Doctoral Dissertation
博士論文

Photoinduced phenomena in organic conductors (有機導体における光誘起現象)

A Dissertation Submitted for
the Degree of Doctor of Philosophy
2023 December
令和５年１２月博士（理学）申請

Department of Physics, Graduate School of Science,
The University of Tokyo
東京大学大学院理学系研究科
物理学専攻

Keisuke Kitayama
北山　圭亮

Abstract

Photoinduced phenomena have become a central focus in recent condensed-matter physics, with numerous studies utilizing light. However, most of these studies has focused on toy models or two-dimensional systems, such as graphene, silicene, and transition metal dichalcogenides. In contrast, bulk materials have been largely overlooked in this area of research. To further advance this promising field, it is crucial to expand the range of target materials. Theoretical studies on real bulk materials with complex crystal and electronic structures are highly desirable.

In this context, we investigate photoinduced phenomena in the organic conductor α-(BEDT-TTF)$_2$I$_3$. Employing two different methods, perturbation theory and Floquet theory, we uncover novel photoinduced phenomena categorized into (i) topological phase transitions and (ii) photovoltaic effects.

In (i), using Floquet theory, we demonstrate three distinct topological phase transitions: a transition to the Chern insulator phase induced by circularly polarized light, the pair annihilation of magnetic charges in momentum space induced by linearly polarized light, and a novel type of photoinduced topological phase transition induced by elliptically polarized light. We explore the reasons behind these photoinduced phase transitions and discuss the feasibility of experimental observation.

In (ii), we examine two nonlinear optical responses: the shift and injection currents. Predicting the dependence of these currents on the frequency of light using perturbation theory, we find that the direction of these currents strongly depends on the frequency. Furthermore, we delve into the nonperturbative effects on these currents using Floquet theory.

These findings highlight that α-(BEDT-TTF)$_2$I$_3$ is a unique material offering a rare opportunity to explore a variety of photoinduced phase-transition phenomena. This work expands the scope of target materials for research on photoinduced phenomena, contributing to the development of optical manipulations of electronic states in condensed matter.

Contents

Chapter 1

Introduction

In Chap. 1, an overview of recent studies on topology in both equilibrium systems and time-periodic systems is provided, setting the context for the research presented in this thesis. The discussion begins with a significant study in the realm of topology in equilibrium systems—the theoretical exploration of the quantum Hall effect. In two-dimensional systems, the quantum Hall conductivity is theoretically shown to be characterized by a topological invariant known as the Chern number. While the quantum Hall effect is originally discussed in the presence of a magnetic field, some theoretical studies have demonstrated the quantized Hall conductivity without the need for a magnetic field. An illustrative example is the quantum Hall effect in time-periodic systems. The Floquet theory allows the mapping of time-periodic systems to static systems, enabling the exploration of topology in time-periodic systems analogous to equilibrium systems. Numerous topological phenomena, including those not realizable in equilibrium systems, have been investigated using this approach. This chapter reviews selected topological phenomena in time-periodic systems, with a focus on topological phase transitions, edge states, nonlinear optical responses, thermalization phenomena, and experimental studies. The chapter concludes by outlining the structure of this thesis.

1.1 Quantum Hall effect and topology

Topological phenomena in quantum materials are a central theme in recent condensed-matter physics. One of the pioneering areas of research that has unveiled the connection between topology and quantum systems is the study of quantum Hall effect. After the experimental observation of the quantum Hall effect, it was revealed to be characterized by the Chern number, a topological invariant defined using the wave function. Since its theoretical explanation, there has been vigorous research in the field of topological materials. In this section, we will review research on the quantum Hall effect and the quantum anomalous Hall effect, the latter of which can be observed even in the absence of a magnetic field.

1.1.1 Quantum Hall effect with a magnetic field

In this section, we introduce the quantum Hall effect, which was the first to reveal the topological properties of quantum materials, along with its theoretical explanation. The quantum Hall effect refers to the phenomenon where the Hall conductivity is quantized in a two-dimensional electron system subjected to a strong magnetic field at low temperatures [1]. Since its experimental observation, attempts to explain this phenomenon were made by Laughlin and others [2]. In 1982, using linear response theory, it was demonstrated that the Hall coefficient is given by the following equation [3]:

$$\sigma_{xy} = \frac{ie^2}{A_0\hbar}\sum_{n\neq m} f_n(\boldsymbol{k})\frac{\langle u_{n\boldsymbol{k}}|\frac{\partial H}{\partial k_x}|u_{m\boldsymbol{k}}\rangle\langle u_{m\boldsymbol{k}}|\frac{\partial H}{\partial k_y}|u_{m\boldsymbol{k}}\rangle - \langle u_{n\boldsymbol{k}}|\frac{\partial H}{\partial k_y}|u_{m\boldsymbol{k}}\rangle\langle u_{m\boldsymbol{k}}|\frac{\partial H}{\partial k_x}|u_{m\boldsymbol{k}}\rangle}{(E_n - E_m)^2}, \tag{1.1}$$

where A_0 denotes the area of the system and H is the Hamiltonian of the system. The quantities E_n and E_m are the eigenvalues of the Hamiltonian, $|u_{n\boldsymbol{k}}\rangle$ is the Bloch function, and $f_n(\boldsymbol{k})$ represents the Fermi-Dirac distribution function. This equation refers to as TKNN formula. In 1985, Kohmoto derive the following equation for the Hall conductivity [4]:

$$\sigma_{xy} = \frac{e^2}{h}\int_{\mathrm{BZ}}\frac{d^2\boldsymbol{k}}{2\pi}\sum_n f_n(\boldsymbol{k})[\nabla_{\boldsymbol{k}}\times\boldsymbol{A}_n(\boldsymbol{k})]_z, \tag{1.2}$$

where the integration is taken over the Brillouin zone. Here, the Berry connection is defined as $\boldsymbol{A}_n(\boldsymbol{k}) = i\langle u_{m\boldsymbol{k}}|\nabla_{\boldsymbol{k}}|u_{m\boldsymbol{k}}\rangle$. The Chern number is defined as follows:

$$\nu_n = \int_{\mathrm{BZ}}\frac{d^2\boldsymbol{k}}{2\pi}[\nabla_{\boldsymbol{k}}\times\boldsymbol{A}_n(\boldsymbol{k})]_z. \tag{1.3}$$

Using the Stokes theorem, it is well-known that this quantity only takes integers when the system is two-dimensional. At absolute zero temperature, the Hall conductivity is determined by summing the Chern numbers (ν) of the bands below the Fermi level, leading to the quantization of the Hall conductivity in two-dimensional systems. This quantized effect is robust against common perturbations, as slight variations in electron density or magnetic field strength do not alter the Chern number ν. Chern numbers are referred to as one of the topological numbers, and the systems where the topological number can be defined from the bulk wave function are called topologically nontrivial systems. The quantum Hall system serves as an example of a topological insulator. An distinctive feature of the quantum Hall system is the presence of chiral edge states. The theoretical work of Y. Hatsugai demonstrated the correspondence between the number of edge states and the Chern number, known as the bulk-edge correspondence [5]. It is crucial to note that breaking time-reversal symmetry is essential for the quantum Hall effect, as a nonzero Chern number cannot be obtained without breaking of time-reversal symmetry.

Subsequently, the quantum spin Hall effect, a topologically nontrivial phenomenon in systems where time-reversal symmetry is not broken, was discovered [6]. The quantum spin Hall effect can be intuitively explained as the superposition of the quantum Hall

effects for spins ↑ and ↓, with the application of a magnetic field in the opposite direction. In the quantum spin Hall effect, there is no magnetic field; instead, spin-orbit interaction plays an essential roles. The edge states exhibit motion in opposite directions for spins ↑ and ↓, and this state is referred to as helical edge states [7]. The three-dimensional versions of this system are observed in certain materials known as a topological insulator, garnering significant attention in recent years [8, 9].

1.1.2 Quantum anomalous Hall effect

As explained in the previous section, the realization of the quantum Hall effect requires the breaking of time-reversal symmetry. However, some theoretical studies have explored the possibility of achieving the quantum Hall effect without the application of a strong magnetic field, leading to what is known as the quantum anomalous Hall effect. One example is the quantum spin Hall effect, which arises due to spin-orbit interaction, as discussed earlier. Another representative model exhibiting this phenomenon is the Haldane model [10]. Haldane considered a tight-binding model of graphene incorporating nearest-neighbor and next-nearest-neighbor hopping terms. He introduced terms breaking spatial inversion symmetry and time-reversal symmetry to demonstrate the occurrence of the quantum Hall effect. Spatial inversion symmetry is broken by adding on-site energies of $+M$ and $-M$ to two sublattices, while time-reversal symmetry is broken by introducing a local magnetic flux in graphene, modifying the next-nearest-neighbor hopping term from t_2 to $t_2 e^{i\phi}$ [Fig. 1.1(a)]. It is noteworthy that the local magnetic flux is zero over the entire unit cell, and Haldane demonstrated the manifestation of the quantum Hall effect even when the energy levels are not discretized as in Landau levels. The phase diagram, depicted using the magnitudes of terms breaking spatial inversion symmetry and time-reversal symmetry [Fig. 1.1(b)], illustrates the phases with a nonzero Chern number, indicating the manifestation of the quantum anomalous Hall effect.

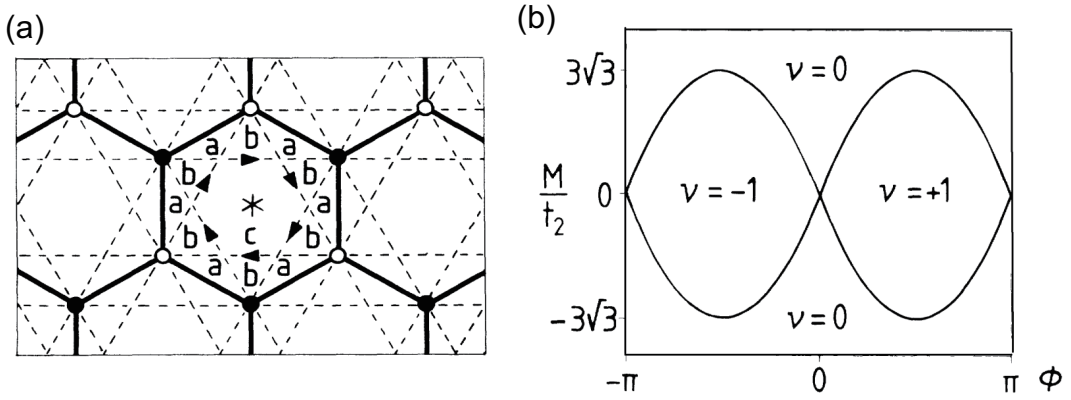

Figure 1.1. (a) Schematic of the Haldane model. There are on-site potentials and a local magnetic flux in the honeycomb lattice model. (b) The phase diagram of the Haldane model depicted in the plane of the phase due to the local magnetic flux and the on-site potential energy. Adapted from Ref. [10].

In 2009, Oka and Aoki theoretically predicted the realization of photoinduced Hall

effect in graphene under irradiation with circularly polarized light [11]. This was demonstrated by combining Floquet theory, a theoretical method to analyze periodically driven systems, with linear response theory which derived the TKNN formula for periodically driven systems. Subsequently, in a later study [12], the effective model for graphene under circularly polarized light was analyzed using Floquet theory, revealing its equivalence to the Haldane model when expanded with respect to $1/\omega$, where ω denotes the frequency of the light. The application of circularly polarized light opens a gap in the Dirac cone of the graphene band structure [Fig. 1.2(a)]. Furthermore, it became evident that edge states emerge in graphene under circularly polarized light based on finite-size system analysis [Fig. 1.2(b)]. Since these studies were presented, research on the topological properties of periodically driven systems has attracted diverse researchers and has been conducted extensively.

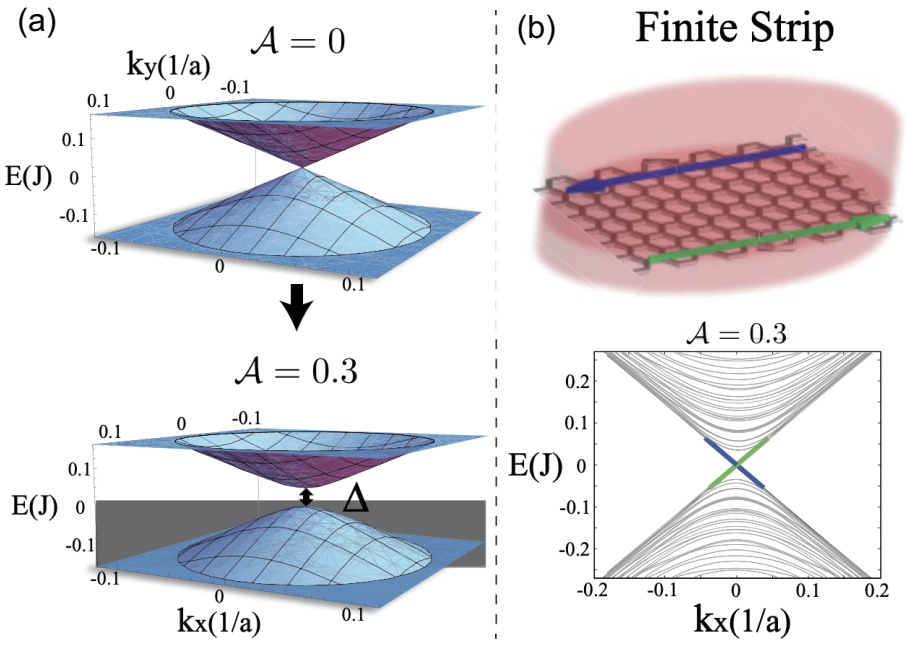

Figure 1.2. (a) The band structure of graphene in the absence of light irradiation (upper figure) and that of graphene irradiated with cirularly polarized light (lower figure). The bandgap opens at the Dirac points due to the irradiation. (b) The graphene nanoribbon with finite sites in one direction (upper figure) and the quasienergy band structure of the graphene nanoribbon irradiated with circularly polarized light (lower figure). Chiral edge states are observed in its band structure. Adapted from Ref. [12].

1.2 Physical phenomena in periodically driven systems

In the previous section, we delved into the exploration of topological properties in equilibrium systems. Now, we shift our focus to the phenomena in periodically driven systems. As mentioned earlier, the pioneering work using the Floquet theorem [11, 12, 13] predicted that a honeycomb lattice irradiated with circularly polarized light achieves a topologically nontrivial band structure similar to the one proposed by Haldane [10]. Since then, there have been numerous attempts to realize phases in non-equilibrium systems by subjecting materials to periodic driving force, which are challenging or impossible to achieve in equilibrium [14]. As an example, theoretical research on fundamental aspects of topology in periodically driven systems, including the classification theory for Floquet systems [15, 16, 17], and applications like controlling quantum spin systems using light [18, 19], have garnered attention. Recent research employing the Floquet theory encompasses theoretical explorations to realize time crystals in periodically driven systems [20], studies examining periodically driven open systems using approaches based on Floquet-Lindblad equations [21, 22], and investigations into the dynamics of periodically driven systems [23, 24, 25, 26]. This showcases a broad spectrum of research in this field. In this section, we review some previous studies of photodriven systems related to this dissertation.

1.2.1 Topological phase transition

Topological phases induced by periodic drive have been explored intensively. For instance, in 2011, Lindner *et al.* demonstrated that subjecting semiconductor quantum well structures to a periodic driving force could induce topologically nontrivial states [27]. While previous studies focused on periodic driving in a gapless system [11, 12], where the frequency is larger than the bandwidth, this research deals with a gapped system under periodic drive, where the frequency is smaller than the bandwidth but larger than the bandgap. Additionally, the mechanism of the phase transition to a topologically nontrivial system is different from that of the photoinduced topological phase transition in graphene. It is impossible to resonantly couple the valence and conduction bands when the frequency is larger than the bandwidth. However, the phase transition proposed by Lindner *et al.* is realized by the resonant coupling between the conduction and valence bands, leading to the opening of the topological bandgap [Figs.1.3(a,b)]. It should be noted that this topological phase transition accompanies the emergence of a chiral edge state, as shown in Fig. 1.3(c).

In addition, the induction of phase transitions by irradiating light has been demonstrated for other materials such as silicene [28], transition metal dichalcogenides [29, 30, 31, 32], and nodal-line semimetals [33, 34, 35]. These theoretical studies utilize a static effective models obtained through Floquet theory. The method to construct the effective model is presented in Sec. 2.2. The design of intriguing properties in periodically driven systems by working backward from effective models is referred to as "Floquet engineering".

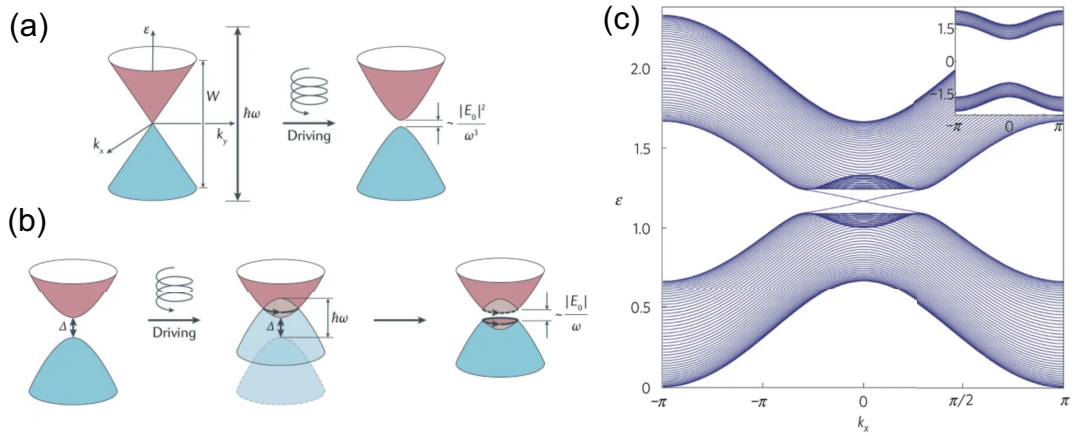

Figure 1.3. (a, b) Schematic illustration of two distinct types of photoinduced topological phase transitions: (a) phase transition in a gapless system induced by a periodic drive with a frequency larger than the bandwidth and (b) phase transition in a gapped system induced by a periodic drive with a frequency smaller than the bandwidth but larger than the bandgap. (c) Quasienergy band structure for the periodically driven semiconductor quantum well with finite extent in one direction, revealing the emergence of chiral edge states connecting the upper and lower bands. The inset shows the band structure of the semiconductor quantum well before the periodic driving. Adapted from Ref. [14, 27].

1.2.2 Edge state in periodically driven system

As mentioned earlier, similar to the Chern insulators in an equilibrium state, chiral edge states appear in graphene irradiated with circularly polarized light [5]. Furthermore, there are other edge states named anomalous edge states that can only be observed in Floquet systems [36]. As mentioned later, time-periodic systems with a period T are characterized by a quasienergy ε that has periodicity: shifting ε by $\varepsilon + 2m\pi/T$ with respect to an integer m results in the same structure. Here m is an integer that corresponds to the photon number. In other words, the quasienergy band structure within the Floquet Brillouin zone $\Lambda = [-\pi/T, \pi/T)$ repeats every $2\pi/T$. In 2013, M. Rudner *et al.* demonstrated that due to the periodicity of quasienergy, edge states between different photon numbers m can emerge, which cannot be observed in equilibrium systems [36] [see the edge state near $\varepsilon = \pi/T$ in Fig. 1.4(a)]. These edge states are referred to as anomalous edge states.

The Chern number of a band is given by $N_{\text{upper}} - N_{\text{lower}}$, where N_{upper} denotes the number of edge states that connect the correponding band and its upper band, and N_{lower} represents the number of edge states that connect the correponding band and its lower band. This fact leads to the bulk-edge correspondence in equilibrium systems. However, in periodically driven systems, anomalous edge states can be realized, leading to the possibility of the emergence of edge states even when all the Chern numbers of the bands in the system are zero [Fig. 1.4(a)]. Figures 1.4(b,c) illustrate a specific example, showing the quasienergy band structure of a two-band model with nonzero Chern numbers with a

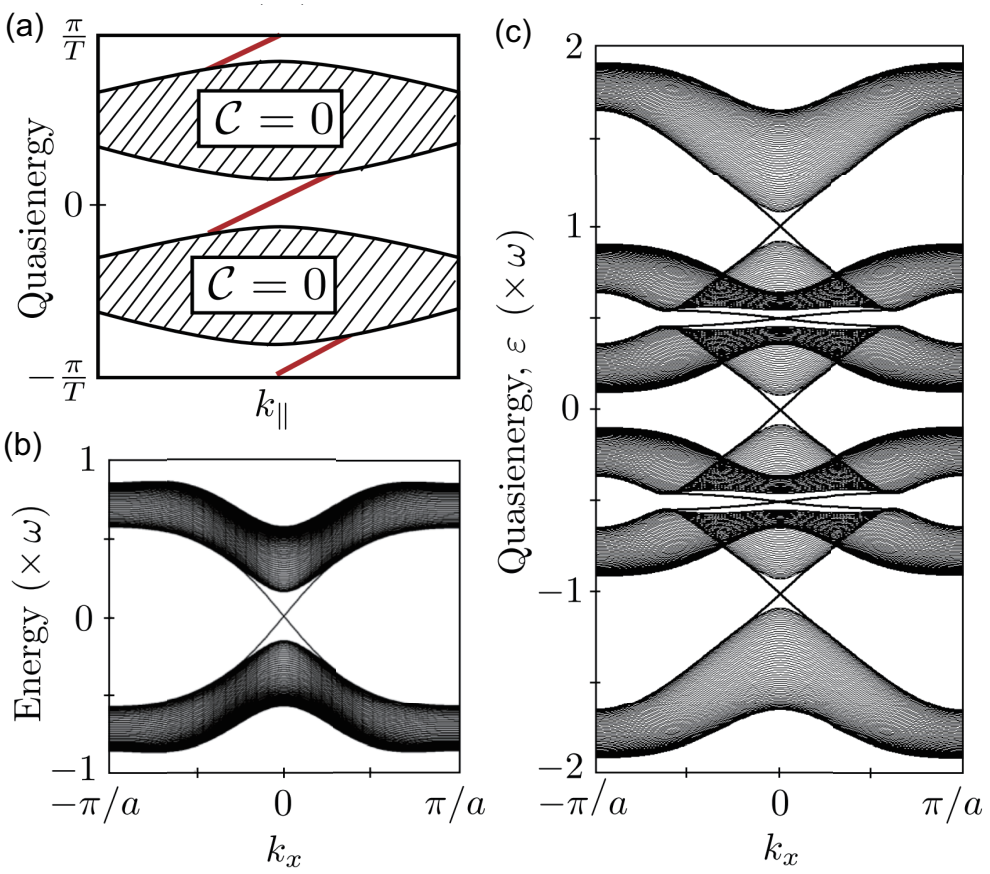

Figure 1.4. (a) Schematic illustration of the band structure where edge states exist despite the Chern numbers of all bands being zero in a periodically driven system. Edge states are present not only around $\varepsilon = 0$ but also around $\varepsilon = \pi/T$, where ε represents the quasienergy. These edge states emerge due to the periodicity of quasienergy ε. (b) Band structure of a two-band model with nonzero Chern numbers for a finite system in the y-direction. (c) Quasienergy band structure for the photodriven system corresponding to the band structure in (b). The analysis was performed by truncating the Floquet Hamiltonian shown in Sec. 2.2 to $-1 \leq m \leq 1$. The Chern numbers of the central two bands corresponding to $m = 0$ are zero, but edge states exist between these bands. Adapted from Ref. [36].

periodic driving force whose frequency ω is half of the bandwidth. It is evident that edge states appear between different photon numbers m. Furthermore, the Chern number of the band with $m = 0$ in Fig. 1.4(c) is zero. It is noted that this band structure was obtained by truncating the Floquet Hamiltonian to $-1 \leq m \leq 1$. These anomalous edge states between different photon numbers also appear in graphene irradiated with circularly polarized light with a frequency smaller than the bandwidth [37, 38].

1.2.3 Nonlinear optical responses

In the previous section, we discussed thermodynamic properties using the quasienergy band structures obtained in the Floquet theory. Now, we delve into transport phenomena. The transport phenomena in periodically driven systems are more intricate because not only the quasienergy band structures but also the nonequilibrium occupation function play a crucial role [39, 40, 41]. Nevertheless, many transport phenomena have been analyzed using Floquet theory [42, 43]. One typical example is nonlinear optical responses, and investigating these responses using Floquet theory enables us to discuss nonperturbative effects in shift currents. In this section, we commence by reviewing previous studies of shift currents before delving into the theoretical study using Floquet theory.

In the linear response theory, the output current $j_\mu(\omega)$ and the input electric field $E_\alpha(\omega)$ have a relation $j_\mu(\omega) = \sigma_{\mu\alpha}E_\alpha(\omega)$. Nevertheless, higher-order terms with respect to the light electric field opens the door to the fascinating realm of nonlinear optical responses [44, 45, 46]. A notable example is second harmonic generation observed in systems with broken spatial-inversion symmetry [47, 48]. Second harmonic generation is one of the second-order nonlinear optical response, resulting in the output current frequency being twice that of the incident light. Another class of nonlinear optical responses that has garnered significant attention is the bulk photovoltaic effect. The bulk photovoltaic effect is also a nonlinear optical response wherein the output current is direct current (dc) even in spite of the alternating current (ac) nature of the input electric field, leading to a rectification effect [44]. Due to this unique mechanism, there has been active exploration of next-generation solar cells utilizing perovskite compounds lacking an inversion center [49, 50]. Understanding this rectification effect has been crucial in the development of novel photovoltaic technologies. This rectification can be comprehended as the outcome of the current frequency being the difference between the input frequencies, contrasting with second harmonic generation, where the input frequencies were combined.

The most widely used method for calculating the nonlinear responses from the bulk photovoltaic effect employs the perturbative approach. Studies based on this approach can be distinguished into two groups: the length gauge [51] and the velocity gauge [45, 46] approaches. These two different gauges incorporate the effect of light in different ways. In the velocity gauge, the effect of light is incorporated by replacing the momentum operator $(\hbar/i)\nabla$ with $(\hbar/i)\nabla + e\boldsymbol{A}(t)$, whereas in the length gauge, the term $e\boldsymbol{r} \cdot \boldsymbol{E}(t)$ is added to the Hamiltonian. It should be noted that these two approaches yield equivalent final results [46, 52]. The formalism for the perturbative approach using the velocity gauge will be discussed in detail in Sec. 2.1.

However, understanding nonperturbative terms higher than second-order through perturbation theory analysis is challenging. Under these circumstances, Morimoto and Na-

gaosa investigated nonlinear optical responses using a different approach: the method based on Floquet theory [53]. They began with a two-band model comprising the valence and conduction bands, with the Fermi level situated between them. Subsequently, they examined the system under irradiation with linearly polarized light and constructed the Floquet Hamiltonian. As discussed in Sec. 2.2, the Floquet Hamiltonian is infinite-dimensional. However, they focused solely on the one-photon absorbed valence band and the original conduction band, leading to a truncated 2×2 matrix Floquet Hamiltonian. They employed Keldysh-Green's function to derive the dc photocurrent. The obtained dc photocurrent is consistent with the photocurrent predicted by perturbation theory when the light amplitude is small. In other words, they theoretically observed that the dc photocurrent J is proportional to the square of the amplitude E^{ω}. However, as the amplitude increases, they observed that J becomes proportional to ΓE^{ω}, where Γ represents the dissipation coefficient.

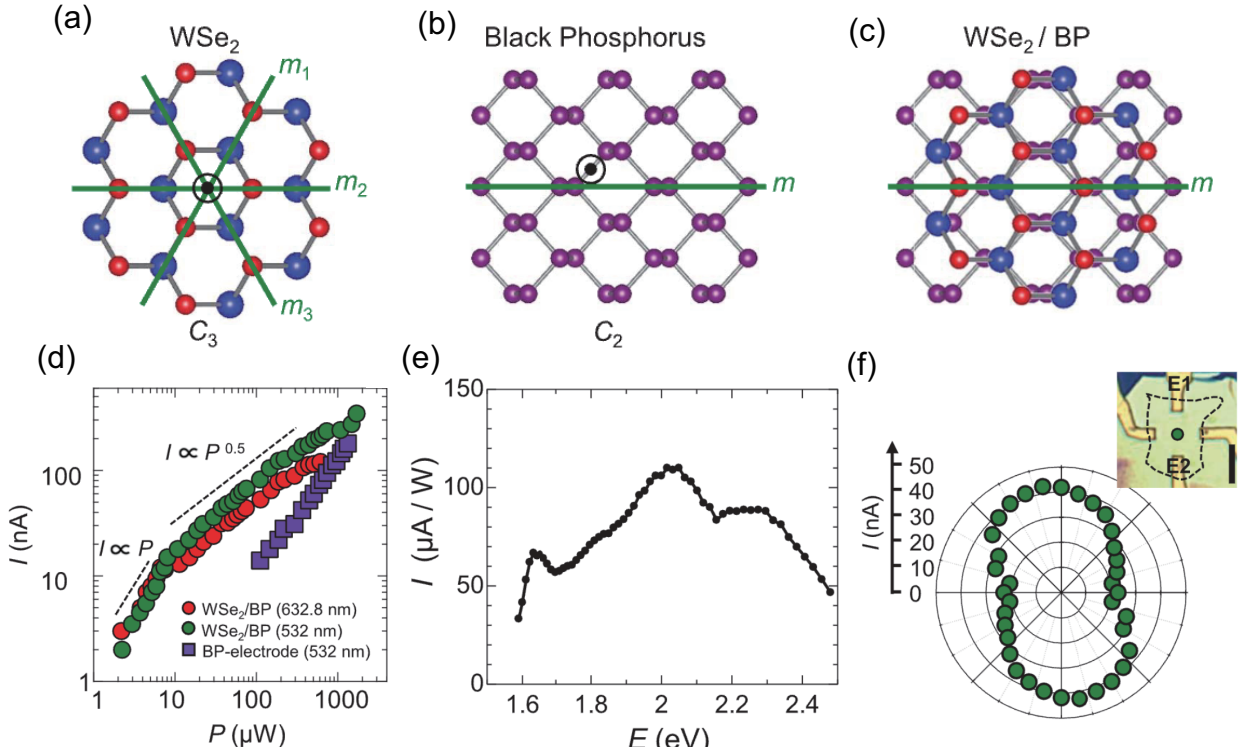

Figure 1.5. (a-c) Schematic image of (a) monolayer WSe_2, (b) black phosphorene, and (c) the heterointerface of WSe_2/BP. (d) Experimental outcomes showing the laser power dependence of the dc photocurrent in WSe_2/BP under irradiation with linearly polarized light. (e) Experimental results displaying the photon energy dependence of the photocurrent. (f) Plots illustrating the observed dc photocurrent as a function of linear polarization angle. Adapted from Ref. [54].

This transition from quadratic to linear dependence of the dc photocurrent with an increase in amplitude has been experimentally observed in a moire system [54]. Akamatsu *et al.* experimentally observed the bulk photovoltaic effect in a van der Waals

heterostructure of WSe_2 and black phosphorene irradiated with linearly polarized light [Fig. 1.5(a-c)]. Fig. 1.5(d) displays the laser power P dependence of the dc photocurrent I. When the power P is small, the dc photocurrent is proportional to the power, but the dependence changes as $I \propto P^{0.5}$ when the power is large. Note that the power is proportional to the square of the intensity of light, so this result is consistent with the theoretical analysis based on Floquet theory. Figure 1.5(e,f) depicts the photon energy dependence of the dc photocurrent and the linear polarization angle dependence of the dc photocurrent, respectively. Both of them are consistent with the theoretical calculation based on the tight-binding model and perturbation theory.

Finally, we delve into the connection between symmetry and nonlinear optical responses. The manifestation of dc photocurrents through nonlinear processes is intricately tied to time-reversal symmetry, spatial-inversion symmetry, and point group symmetry [55, 56, 57]. For instance, the presence of spatial-inversion symmetry renders the bulk photovoltaic effect non-existent. Conversely, in scenarios where inversion symmetry is absent but time-reversal symmetry is preserved, two second-order nonlinear optical responses emerge: the shift current and the circular injection current [45, 46]. As elucidated in Sec. 2.1, the shift current represents the bulk photovoltaic effect induced by linearly polarized light, while the circular injection current arises from circularly polarized light. In cases where both inversion and time-reversal symmetries are broken, yet their product is conserved, the induction of shift current from circularly polarized light and injection current from linearly polarized light occurs. These photocurrents are commonly referred to as magnetic photocurrents [58, 59]. In this thesis, our focus is on the organic conductor with charge order, where time-reversal symmetry is present while inversion symmetry is not conserved.

1.2.4 Floquet prethermalization

As explained earlier, various intriguing phenomena have been theoretically observed in periodically driven systems. However, in 2014, it became evident that there are problems in the theory of periodically driving isolated systems [60]. Specifically, it was shown that the perturbative expansion with respect to $1/\omega$ of the effective Hamiltonian obtained from Floquet theory generally does not converge. This is attributed to the fact that in isolated quantum systems, there is no way for the energy to dissipate, and the system is heated by the periodic drive. More precisely, when rigorously determining the Floquet eigenstates $|u_\alpha\rangle$ of interacting many-body systems and calculating the expectation value of a local physical quantity $\hat{O}$, it was demonstrated that it approaches the thermal equilibrium value as,

$$\langle u_\alpha|\hat{O}|u_\alpha\rangle \to \mathrm{Tr}[\hat{O}\rho_\infty] \quad \text{if } t \to \infty \tag{1.4}$$

in the thermodynamic limit. Here, ρ_∞ represents the infinite-temperature state. This assertion is referred to as the Floquet Eigenstate Thermalization Hypothesis [60, 61].

According to this thermalization hypothesis, Floquet eigenstates under periodic driving generally correspond to infinite-temperature states at $t \to \infty$. After this research was presented, T. Kuwahara *et al.* demonstrated that for systems with short-range interactions subjected to a high-frequency external field, the expectation value of any local

physical quantity $\hat{O}$ satisfies

$$\langle\psi(t)|\hat{O}|\psi(t)\rangle \simeq \langle\psi(0)|e^{(i/\hbar)H_{\rm eff}^n t}\hat{O}e^{-(i/\hbar)H_{\rm eff}^n t}|\psi(0)\rangle \tag{1.5}$$

for sufficiently large n and times $t \ll (\hbar/g)e^{O(\hbar\omega/g)}$, where g denotes the characteristic energy of the system [62, 63, 64, 65]. Here, $|\Psi(t)\rangle$ is the solution of the time-dependent Schrödinger equation for the periodically driven Hamiltonian $H(t)$, and $H_{\rm eff}^n$ is the effective model of $H(t)$ expanded to n-th order in $1/\omega$. It is known that the equation holds for n up to integers of the order of ω/g. Therefore, for $t \ll (\hbar/g)e^{O(\hbar\omega/g)}$, the perturbatively expanded effective Hamiltonian in $1/\omega$ can approximately describing the system's time evolution.

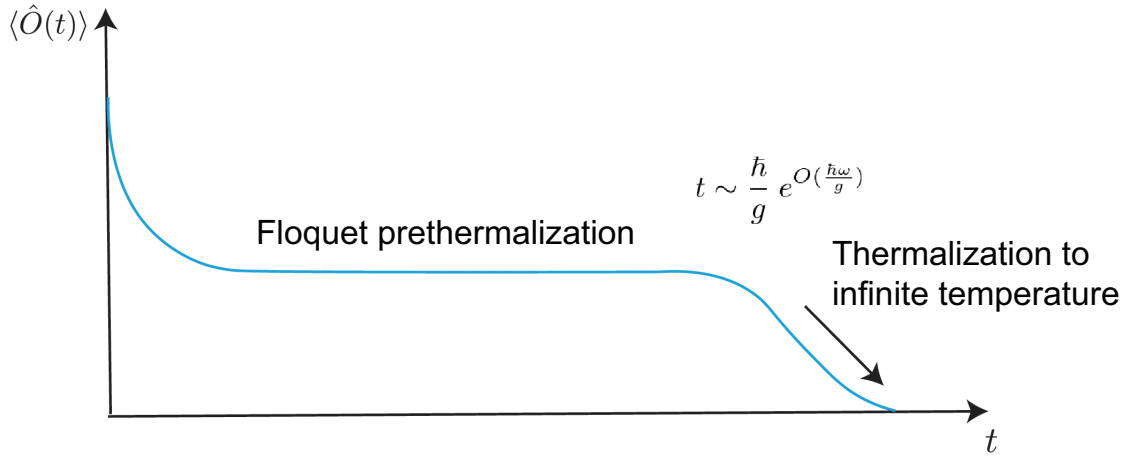

Figure 1.6. Time evolution of the expectation value of a local physical quantity $\hat{O}(t)$ in periodically driven isolated quantum systems. There are two relaxation steps in periodically driven isolated quantum systems, and the relaxation to the first-step quasi-steady state before reaching infinite temperature is referred to as prethermalization in the Floquet prethermalized state.

Let us explain the physical picture of this theorem. For the system to absorb energy from the periodic driving force with frequency ω, a single site must be able to absorb energy up to about g. Consequently, it is necessary to involve approximately $\hbar\omega/g$ sites to absorb energy. Terms of this nature appear in the effective Hamiltonian of Floquet theory at the same order of magnitude as $\hbar\omega/g$. Therefore, considering only low-order terms in the perturbative expansion of the effective Hamiltonian is equivalent to ignoring processes of absorbing or emitting energy from the periodic drive. According to this theorem, the time evolution of a local physical quantity $\hat{O}(t)$ exhibits two-step relaxation, as illustrated in Fig. 1.6. The relaxation to the first-step quasi-steady state before reaching infinite temperature is called prethermalization in the Floquet prethermalized state. We will refer to this quasi-steady state as the nonequilibrium steady state in this thesis.

1.2.5 Experiments of periodically driven systems

In conclusion of this section, we discuss experiments conducted in the periodically driven system. While the field of Floquet systems is predominantly theoretical and has seen relatively few experiments, there have been notable instances where theoretical predictions based on Floquet theory have been confirmed experimentally. Representative experiments include the experimental realization of Floquet topological insulators using photonic crystals, where edge states were observed [66, 67], and the experimental realization of the Haldane model by periodically driving it through oscillations of the optical lattice [68].

Additionally, some experiments confirmed the renormalization of transfer integrals characterized by Bessel function under the application of a periodic drive [69]. For instance, H. Lignier *et al.* conducted the experiments of shaking the optical lattices as shown in Fig. 1.7(a). Figure 1.7(b) displays the dependence of the transfer integral on the periodic drive. The renormalization of transfer integrals is explained using the Floquet effective Hamiltonian. Specifically, as shown in Sec. 2.2, the zeroth-order term obtained by perturbative expansion with respect to $1/\omega$ of the effective Hamiltonian for the periodically driven tight-binding model corresponds to the tight-binding Hamiltonian with the transfer integrals replaced by $t_{i,j} \to t_{i,j} J_0(\mathcal{A}_{i,j})$, where $\mathcal{A}_{i,j}$ is the dimensionless amplitude of the periodic drive. In this thesis, phenomena attributed to this renormalization of transfer integrals are also observed.

Another noteworthy experiment involves the observation of the photoinduced anomalous Hall effect in monolayer graphene [70]. In this experiment, a graphene sample with four electrical contacts was exposed to ultrafast mid-infrared circularly polarized light, as illustrated on the right side of Fig.1.8(a). The frequency of this light is 191 meV, and the intensity is 4.0×10^7 V/m, corresponding to a pump fluence of 0.23 mJ/cm^2. The anomalous Hall currents were detected using a laser-induced photoconductive switch, enabling time-resolved transport measurements with picosecond timescale resolution, as shown on the left side of Fig.1.8(a) [71].

Several notable features of the photoinduced Hall conductivity were observed in this experiment. Firstly, the anomalous Hall current exhibited a perpendicular orientation to the applied current and experienced a reversal of polarity when light helicities were opposite [Fig.1.8(b)]. Secondly, an observable conductance plateau with a width of 60 meV was identified when the Fermi energy was adjusted within the gap [Fig.1.8(c)], indicating a consistent gap opening with the theoretically calculated photoinduced gap of 69 meV [Fig.1.8(d)]. Furthermore, this experimental study revealed that when the Fermi energy lies in the bandgap, the estimated Hall conductance is around $1.8 \pm 0.4\ e^2/\hbar$. However, theoretical studies using a quantum Liouville equation with relaxations emphasized that, even though Floquet states are realized, the observed anomalous Hall effect in photodriven graphene is not solely attributed to the Berry curvature of the Floquet bands but is also influenced by the population imbalance within the photon dressed bands[72, 73, 74].

The experiment observing anomalous Hall conductivity in photodriven graphene represents a significant study of photoinduced topological phase transitions in two-dimensional Dirac systems. Additionally, more recently, the observation of anomalous Hall conductance in three-dimensional Dirac semimetals has been reported by several different

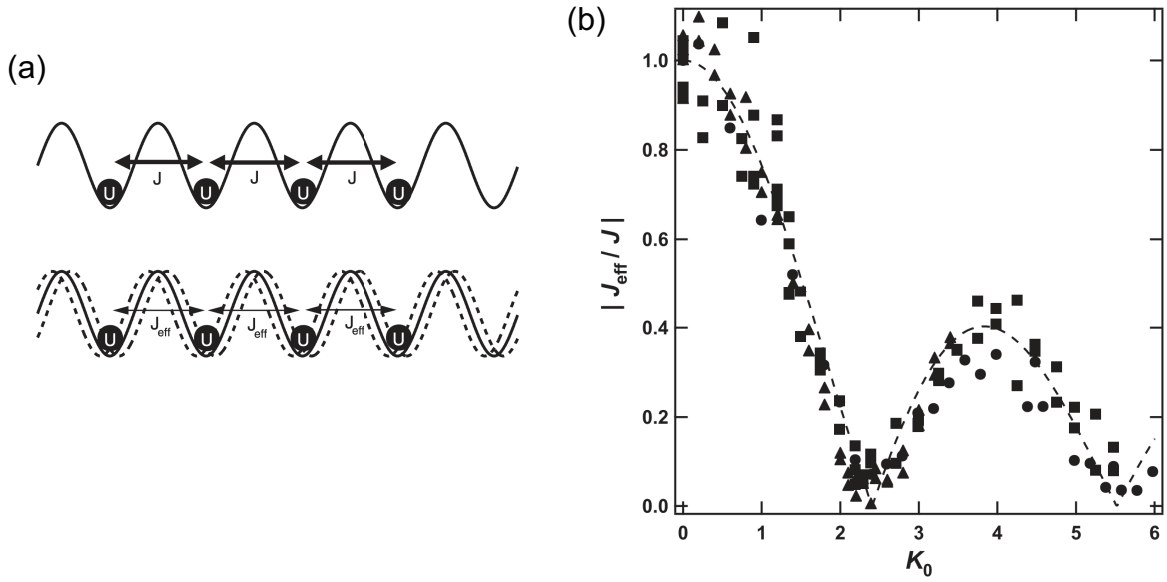

Figure 1.7. (a) Schematic illustration of optical lattice without the periodic drive (upper figure) and the shaken optical lattice (lower figure). (b) The transfer integral J_{eff} of the shaken optical lattice as a function of the amplitude of the periodic drive is shown. The vertical axis represents the transfer integral J_{eff} normalized to the transfer amplitude J before the periodic drive, while the horizontal axis represents the ratio of the amplitude to the frequency of the oscillating external field. The dashed line represents the theoretical prediction derived from Floquet theory. Adapted from Ref. [69].

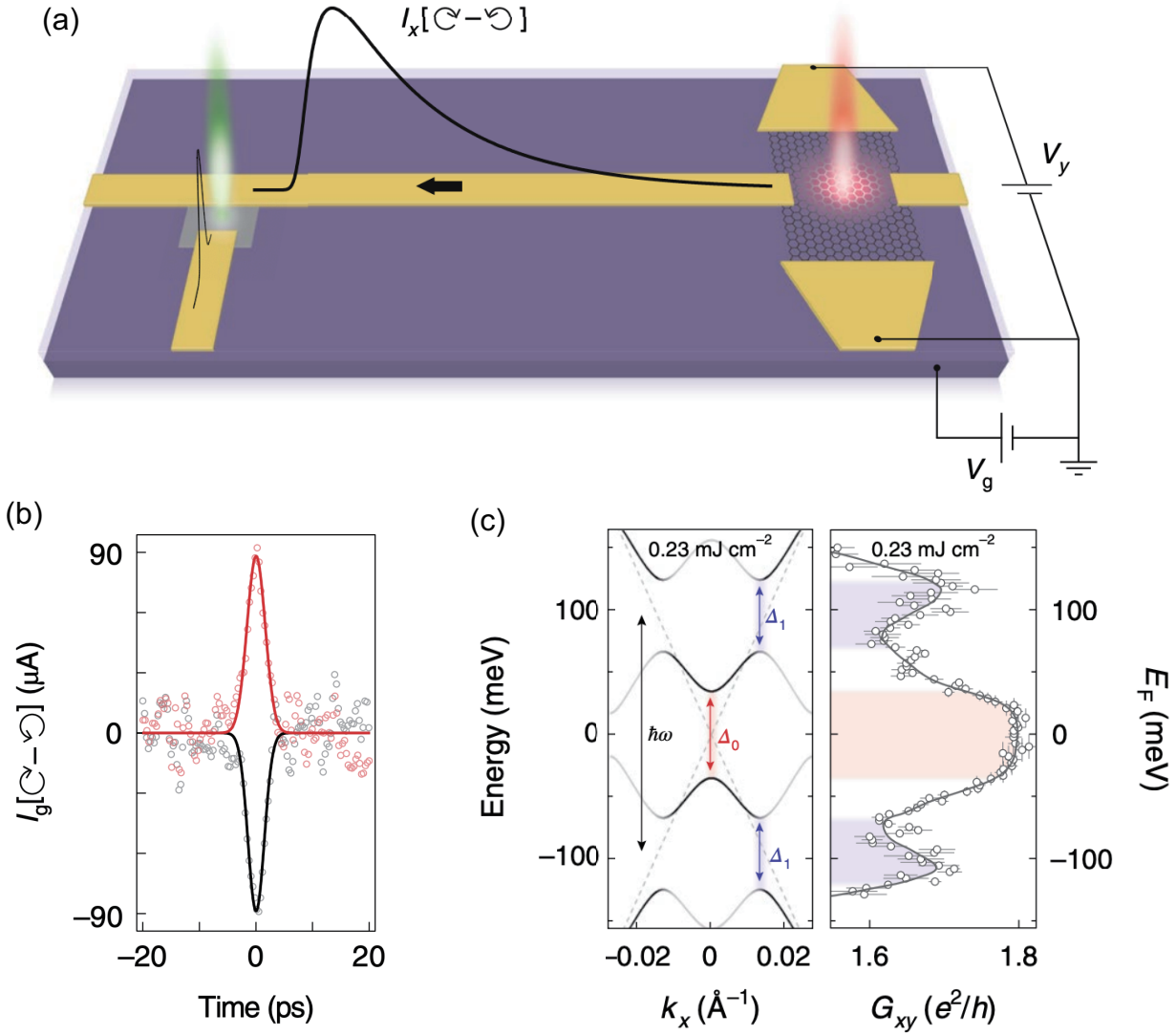

Figure 1.8. (a) Schematic illustration for the observation of light induced Hall conductivity (b) Anomalous Hall current signals I_g with an opposite direction of an applied dc voltage bias. (c) The Fremi-energy dependence of observed Hall conductance G_{xy} and the corresponding Floquet quasienergy band structure obtaianed using theoretical calculation. Adapted from Ref. [70].

groups [75, 76]. These experiments are based on the theoretical prediction of a photoinduced topological phase transition from a three-dimensional phase to Floquet Weyl semimetal phases [77]. While these experimental results demonstrate the realization of Floquet Weyl semimetal phases in photodriven three-dimensional Dirac semimetals, most theoretical predictions using Floquet theory are still awaiting experimental validation.

1.3 Outline of this thesis

In this chapter, we have reviewed significant studies in both equilibrium systems and periodically driven systems. However, most of these investigations primarily focus on toy models or two-dimensional systems such as graphene, silicene, and transition metal dichalcogenides. In light of these circumstances, our thesis delves into the exploration of photoinduced phenomena within the organic conductor α-(BEDT-TTF)$_2$I$_3$ [78]. We focus on this organic conductor because it is a real bulk material with a pair of Dirac-cone bands in its band structure. Additionally, the lattice constant of this material is larger than that of other graphene-like materials, resulting in the enhancement of the applied light effects.

In Chap. 2, we provide a comprehensive review of two distinct methods for analyzing photodriven systems. The first method is grounded in perturbation theory with respect to the light electric field. Here, we derive the dc photocurrent up to the second order with respect to the electric field. The second method employs Floquet theory, and we discuss the process of obtaining a static effective Hamiltonian in photodriven systems.

In Chap. 3, we present recent studies predicting various photoinduced phase transitions in photodriven α-(BEDT-TTF)$_2$I$_3$. Leveraging the Floquet effective Hamiltonian, we anticipate three photoinduced topological phase transitions: a topological phase transition induced by circularly polarized light [79, 80], the pair annihilation of emergent magnetic charges in α-(BEDT-TTF)$_2$I$_3$ under irradiation with linearly polarized light [81], and a novel type of photoinduced topological phase transition accompanied by the collision and collapse of Dirac cones in α-(BEDT-TTF)$_2$I$_3$ induced by elliptically polarized light [82]. We elucidate these phenomena by examining band structures, Chern numbers, and Hall conductivity. Additionally, we discuss the feasibility of experimental observations.

In Chap. 4, our focus shifts to the examination of nonlinear optical responses induced by light irradiation in α-(BEDT-TTF)$_2$I$_3$. We specifically explore two distinct responses: the shift current induced by linearly polarized light [83] and the injection current induced by circularly polarized light [84]. Employing perturbation theory, we demonstrate the frequency dependence of these currents. Furthermore, we delve into the nonperturbative effects using Floquet theory.

In Chap. 5, we consolidate and summarize all the discussions presented in this thesis. Additionally, we conclude the thesis by discussing new and related future problems.

Chapter 2

Analytical method for photodriven systems

In this chapter, we review two different methods for analyzing photodriven systems. One approach involves taking perturbations with respect to the external light electric field, and we employ this method when investigating the dc photocurrent in Chap. 4. In Sec. 2.1, we survey recent studies that explore current responses to the light electric field using the Heisenberg equation [45]. It's worth noting that we consider up to second-order responses with respect to the electric field since the second-order is the smallest order that results in the dc photocurrent. The other method to analyze photodriven systems involves using Floquet theory. One advantage of this method, compared to perturbation theory, is that it allows us to discuss nonperturbative effects of irradiation with light. We apply Floquet theory when studying photoinduced topological phase transitions [Chap. 3] and nonperturbative effects in dc photocurrents [Chap. 4]. In Sec. 2.2, we review the method for constructing the static Floquet effective Hamiltonian and discuss its physical interpretations [85]. We conclude this section by introducing our recent calculation of the Floquet effective Hamiltonian for the photodriven tight-binding model [80].

2.1 Perturbation theory

In this section, we delve into the perturbation theory of current response with respect to the light electric field. Initially, we construct the dipole Hamiltonian, which serves as the foundation for our perturbation analysis. Subsequently, we define the current density operator, as our primary emphasis lies on current response in this thesis. Finally, we apply perturbation to the current density with respect to the electric field and discuss the physical interpretation of the calculation results for second-order responses.

2.1.1 The dipole Hamiltonian

In this section, we construct the dipole Hamiltonian for photodriven systems, which was introduced by Sipe *et al.* in Ref. [45]. We employ the Hamiltonian given by,

$$H(t) = \int \psi^{\dagger}(\boldsymbol{x}, t)\mathcal{H}(t)\psi(\boldsymbol{x}, t)d\boldsymbol{x}. \tag{2.1}$$

where $\psi(\boldsymbol{x}, t)$ denotes the electronic field operator in the Heisenberg picture that satisfies

$$\{\psi(\boldsymbol{x}, t), \psi^{\dagger}(\boldsymbol{x}', t)\} = \delta(\boldsymbol{x} - \boldsymbol{x}'). \tag{2.2}$$

Here $\mathcal{H}(t)$ is defined as,

$$\mathcal{H}(t) = \frac{1}{2m}\left[-i\hbar\nabla + e\boldsymbol{A}(t)\right]^2 + V(\boldsymbol{x}), \tag{2.3}$$

where $\boldsymbol{A}(t)$ refer to a vector potential that produces the light electric field given by $\boldsymbol{E}(t) = -d\boldsymbol{A}(t)/dt$, and $V(\boldsymbol{x})$ is the periodic potential characterized by $V(\boldsymbol{x}) = V(\boldsymbol{x}+\boldsymbol{a})$, where $\boldsymbol{a}$ represents the lattice unit vector. The Heisenberg equation of motion is given by,

$$i\hbar\frac{d\psi(\boldsymbol{x}, t)}{dt} = [\psi(\boldsymbol{x}, t), H(t)]. \tag{2.4}$$

Next, we define the Hamiltonian without the vector potential as,

$$\mathcal{H}_0 = -\frac{\hbar^2\nabla^2}{2m} + V(\boldsymbol{x}), \tag{2.5}$$

and the eigenvectors of this Hamiltonian $\mathcal{H}_0$ as $\psi_n(\boldsymbol{k}, \boldsymbol{x})$. Using the Bloch's theorem, $\psi_n(\boldsymbol{k}, \boldsymbol{x})$ can be divided into the phase factor and the periodic function as $\psi_n(\boldsymbol{k}, \boldsymbol{x}) = u_n(\boldsymbol{k}, \boldsymbol{x})e^{i\boldsymbol{k}\cdot\boldsymbol{x}}$, where $u_n(\boldsymbol{k}, \boldsymbol{x})$ is a function that satisfies $u_n(\boldsymbol{k}, \boldsymbol{x}) = u_n(\boldsymbol{k}, \boldsymbol{x} + \boldsymbol{a})$. Then, we define the function $\bar{\psi}_n(\boldsymbol{k}, \boldsymbol{x}, t)$ as

$$\bar{\psi}_n(\boldsymbol{k}, \boldsymbol{x}, t) = \psi_n(\boldsymbol{k}, \boldsymbol{x}) \exp[-ie\boldsymbol{A}(t) \cdot \boldsymbol{x}/\hbar]. \tag{2.6}$$

By taking the differentiation with respect to time, we obtain

$$i\hbar\frac{\partial\bar{\psi}_n(\boldsymbol{k}, \boldsymbol{x}, t)}{\partial t} = -e\boldsymbol{E}(t) \cdot \boldsymbol{x}\ \psi_n(\boldsymbol{k}, \boldsymbol{x}) \exp[-ie\boldsymbol{A}(t) \cdot \boldsymbol{x}/\hbar]. \tag{2.7}$$

Since it is difficult to deal with a factor of $\boldsymbol{x}$, we eliminate this factor by considering the differentiation with respect to $\boldsymbol{k}$. Then, Eq. (2.7) is rewritten as

$$i\hbar\frac{\partial\bar{\psi}_n(\boldsymbol{k}, \boldsymbol{x}, t)}{\partial t} - ie\boldsymbol{E}(t) \cdot \frac{\partial\bar{\psi}_n(\boldsymbol{k}, \boldsymbol{x}, t)}{\partial \boldsymbol{k}} = -e\boldsymbol{E}(t) \cdot \sum_m \boldsymbol{\xi}_{mn}(\boldsymbol{k})\bar{\psi}_m(\boldsymbol{k}, \boldsymbol{x}, t), \tag{2.8}$$

where the Berry connection $\boldsymbol{\xi}_{mn}(\boldsymbol{k})$ is defined as

$$\boldsymbol{\xi}_{mn}(\boldsymbol{k}) = i\int d\boldsymbol{x}\ u_m^*(\boldsymbol{k}, \boldsymbol{x})\frac{\partial u_n(\boldsymbol{k}, \boldsymbol{x})}{\partial \boldsymbol{k}}. \tag{2.9}$$

It should be noted that $\boldsymbol{\xi}_{mn}(\boldsymbol{k})$ satisfies the following equation:

$$i\frac{\partial u_n(\boldsymbol{k}, \boldsymbol{x})}{\partial \boldsymbol{k}} = \sum_m u_m(\boldsymbol{k}, \boldsymbol{x})\boldsymbol{\xi}_{mn}(\boldsymbol{k}). \tag{2.10}$$

In this thesis, we do not consider the degeneracy of bands expect for the spin degrees of freedom. Therefore, $\partial\bar{\psi}_n(\boldsymbol{k},\boldsymbol{x},t)/\partial\boldsymbol{k}$ is finite and well defined. Considering the definition of $\bar{\psi}_n(\boldsymbol{k},\boldsymbol{x},t)$ in Eq. (2.6), $\bar{\psi}_n(\boldsymbol{k},\boldsymbol{x},t)$ form a complete set. Hence, we expand the field operator $\psi(\boldsymbol{x},t)$ as,

$$\psi(\boldsymbol{x},t) = \sum_n \int d\boldsymbol{k}\; a_n(\boldsymbol{k},t)\bar{\psi}_n(\boldsymbol{k},\boldsymbol{x},t), \tag{2.11}$$

where $a_n(\boldsymbol{k},t)$ denotes the Fermion operator that satisfies the anticommutation relations

$$\{a_n(\boldsymbol{k},t), a_n^\dagger(\boldsymbol{k}',t)\} = \delta_{n,m}\delta(\boldsymbol{k}-\boldsymbol{k}'), \tag{2.12}$$

We substitute Eq. (2.11) into the Heisenberg equation of motion in Eq. (2.4). The differentiation of $\psi(\boldsymbol{x},t)$ with respect to time becomes

$$\begin{aligned}\frac{\partial\psi(\boldsymbol{x},t)}{\partial t} &= \sum_n \int d\boldsymbol{k}\; \left[\frac{\partial a_n(\boldsymbol{k},t)}{\partial t}\bar{\psi}_n(\boldsymbol{k},\boldsymbol{x},t) + a_n(\boldsymbol{k},t)\frac{\partial\bar{\psi}_n(\boldsymbol{k},\boldsymbol{x},t)}{\partial t}\right] \\ &= \sum_n \int d\boldsymbol{k}\; \left[\frac{\partial a_n(\boldsymbol{k},t)}{\partial t} - \frac{e\boldsymbol{E}(t)}{\hbar}\cdot\frac{\partial a_n(\boldsymbol{k},t)}{\partial\boldsymbol{k}} + \frac{ie\boldsymbol{E}(t)}{\hbar}\cdot\sum_m \boldsymbol{\xi}_{nm}(\boldsymbol{k})a_m(\boldsymbol{k},t)\right]\bar{\psi}_n(\boldsymbol{k},\boldsymbol{x},t).\end{aligned} \tag{2.13}$$

On the other hand, the right-hand side of Eq. (2.4) is transformed as

$$[\psi(\boldsymbol{x},t), H(t)] = \sum_n \int d\boldsymbol{k}\; E_n(\boldsymbol{k})a_n(\boldsymbol{k},t)\bar{\psi}_n(\boldsymbol{k},\boldsymbol{x}), \tag{2.14}$$

where $E_n(\boldsymbol{k})$ denotes the eigenvalues of $\mathcal{H}_0$ that correspond to the eigenvectors $\psi_n(\boldsymbol{k},\boldsymbol{x})$. By taking the projection of $\bar{\psi}_n(\boldsymbol{k},\boldsymbol{x})$, we obtain an effective Hamiltonian for $a_n(\boldsymbol{k},t)$, which satisfy

$$i\hbar\frac{\partial a_n(\boldsymbol{k},t)}{\partial t} = [a_n(\boldsymbol{k},t), H_{\text{eff}}], \tag{2.15}$$

in an explicitly Hermitian form as,

$$\begin{aligned}H_{\text{eff}} = &\sum_n \int d\boldsymbol{k}\; E_n(\boldsymbol{k})a_n^\dagger(\boldsymbol{k},t)a_n(\boldsymbol{k},t) + ie\boldsymbol{E}(t)\cdot\sum_n\int d\boldsymbol{k}\;[a_n^\dagger(\boldsymbol{k},t)\partial a_n(\boldsymbol{k},t)] \\ &+e\boldsymbol{E}(t)\sum_{n,m}\int d\boldsymbol{k}\;\boldsymbol{r}_{nm}a_n^\dagger(\boldsymbol{k},t)a_m(\boldsymbol{k},t),\end{aligned} \tag{2.16}$$

where we define the quantity $\boldsymbol{r}_{nm}$ as

$$\boldsymbol{r}_{nm} = \begin{cases}\boldsymbol{\xi}_{nm} & \text{if } n\neq m \\ 0 & \text{otherwise,}\end{cases} \tag{2.17}$$

and the differentation in $[a_n^\dagger(\boldsymbol{k},t)\partial a_n(\boldsymbol{k},t)]$ is defined as

$$[a_n^\dagger(\boldsymbol{k},t)\partial a_n(\boldsymbol{k},t)] = \frac{1}{2}\left[a_n^\dagger(\boldsymbol{k},t)\frac{\partial a_n(\boldsymbol{k},t)}{\partial\boldsymbol{k}} - \frac{\partial a_n^\dagger(\boldsymbol{k},t)}{\partial\boldsymbol{k}}a_n(\boldsymbol{k},t)\right] - i\boldsymbol{\xi}_{nn}(\boldsymbol{k})a_n^\dagger(\boldsymbol{k},t)a_n(\boldsymbol{k},t). \tag{2.18}$$

2.1.2 Current density operator

In this section, we define and discuss the current density operator. The current density operator in Heisenberg picture is defined as,

$$\begin{aligned}\boldsymbol{J}(t) &= -\frac{e}{m}\int \frac{d\boldsymbol{x}}{\Omega}\psi^{\dagger}(\boldsymbol{x},t)[-i\hbar\nabla + e\boldsymbol{A}(t)]\psi(\boldsymbol{x},t) \\ &= -e\sum_{n,m}\int \frac{d\boldsymbol{k}}{\Omega}\boldsymbol{v}_{nm}(\boldsymbol{k})a_n^{\dagger}(\boldsymbol{k},t)a_m(\boldsymbol{k},t),\end{aligned} \tag{2.19}$$

where Ω denotes the volume of the system and the velocity matrix elements $\boldsymbol{v}_{nm}(\boldsymbol{k})$ are given by,

$$\boldsymbol{v}_{nm}(\boldsymbol{k})\delta(\boldsymbol{k}-\boldsymbol{k}') = \frac{1}{m}\int d\boldsymbol{x}\ \psi_n^*(\boldsymbol{k},\boldsymbol{x})(-i\hbar\nabla)\psi_m(\boldsymbol{k}',\boldsymbol{x}). \tag{2.20}$$

Note that the matrix $\boldsymbol{v}_{nm}(\boldsymbol{k})$ can be rewritten as,

$$\boldsymbol{v}_{nm}(\boldsymbol{k}) = \begin{cases} \dfrac{1}{\hbar}\dfrac{\partial E_n(\boldsymbol{k})}{\partial \boldsymbol{k}} & \text{for } n = m \\ \dfrac{\imath}{\hbar}(E_n(\boldsymbol{k}) - E_m(\boldsymbol{k}))\boldsymbol{\xi}_{nm}(\boldsymbol{k}) & \text{for } n \neq m. \end{cases} \tag{2.21}$$

We also define intraband and interband polarization operators $\boldsymbol{P}_{\text{intra}}$ and $\boldsymbol{P}_{\text{inter}}$. The Hamiltonian in Eq. (2.16) leads us to define them as,

$$\boldsymbol{P}_{\text{intra}}(t) = -ie\int \frac{d\boldsymbol{k}}{\Omega}\sum_n [a_n^{\dagger}(\boldsymbol{k},t)\partial a_n(\boldsymbol{k},t)], \tag{2.22}$$

$$\boldsymbol{P}_{\text{inter}}(t) = -e\int \frac{d\boldsymbol{k}}{\Omega}\sum_{nm}\boldsymbol{r}_{nm}(\boldsymbol{k})a_n^{\dagger}(\boldsymbol{k},t)a_m(\boldsymbol{k},t). \tag{2.23}$$

Then, the Hamiltonian in Eq. (2.16) is rewritten as,

$$H_{\text{eff}}(t) = H_O - \Omega[\boldsymbol{P}_{\text{intra}}(t) + \boldsymbol{P}_{\text{inter}}(t)]\cdot\boldsymbol{E}(t), \tag{2.24}$$

where the Hamiltonian H_O is defined as,

$$H_O = \sum_n \int d\boldsymbol{k}E_n(\boldsymbol{k})a_n^{\dagger}(\boldsymbol{k},t)a_n(\boldsymbol{k},t). \tag{2.25}$$

The relation between current density operator $\boldsymbol{J}(t)$ and the polarization operators $\boldsymbol{P}_{\text{inter}}$ and $\boldsymbol{P}_{\text{intra}}$ is given by,

$$\boldsymbol{J}(t) = \boldsymbol{J}_{\text{intra}}(t) + \frac{d\boldsymbol{P}_{\text{inter}}(t)}{dt}, \tag{2.26}$$

where $\boldsymbol{J}_{\text{intra}}(t)$ is defined as,

$$\boldsymbol{J}_{\text{intra}}(t) = -e\int \frac{d\boldsymbol{k}}{\Omega}\sum_{nm}\bar{\boldsymbol{v}}_{nm}(\boldsymbol{k},t)a_n^{\dagger}(\boldsymbol{k})a_m(\boldsymbol{k}). \tag{2.27}$$

In this equation, $\bar{\boldsymbol{v}}_{nm}(\boldsymbol{k},t)$ is given by,

$$\begin{aligned}\bar{v}^a_{nm}(\boldsymbol{k},t) &= v^a_{nn}(\boldsymbol{k})\delta_{nm} + \frac{e\, r^b_{nm;a}(\boldsymbol{k})E^b(t)}{\hbar} \\ &= \frac{\boldsymbol{\varepsilon}_{nm;a}(\boldsymbol{k},t)}{\hbar},\end{aligned} \tag{2.28}$$

where $\boldsymbol{\varepsilon}_{nm}(\boldsymbol{k},t)$ is defined as,

$$\boldsymbol{\varepsilon}_{nm}(\boldsymbol{k},t) = \hbar\omega_n(\boldsymbol{k})\delta_{nm} - e\,\boldsymbol{r}_{nm}(\boldsymbol{k})\cdot\boldsymbol{E}(t). \tag{2.29}$$

Here the generalized derivative $r^a_{nm;b}$ is defined as,

$$r^a_{nm;b} = \frac{\partial r^a_{nm}(\boldsymbol{k})}{\partial k_b} - i\left[\xi^b_{nn}(\boldsymbol{k}) - \xi^b_{mm}(\boldsymbol{k})\right] r^a_{nm}(\boldsymbol{k}). \tag{2.30}$$

Equation (2.26) is proved by using the Heisenberg equation of motion and the sum rules:

$$\frac{\partial\xi^a_{nn}(\boldsymbol{k})}{\partial k^b} - \frac{\partial\xi^b_{nn}(\boldsymbol{k})}{\partial k^a} = -i\sum_p\left[r^a_{np}(\boldsymbol{k})r^b_{pn}(\boldsymbol{k}) - r^b_{np}(\boldsymbol{k})r^a_{pn}(\boldsymbol{k})\right], \tag{2.31}$$

$$r^a_{nm;b} - r^b_{nm;a} = -i\sum_p\left[r^a_{np}(\boldsymbol{k})r^b_{pm}(\boldsymbol{k}) - r^b_{np}(\boldsymbol{k})r^a_{pm}(\boldsymbol{k})\right]. \tag{2.32}$$

For a simple derivation of the sum rules, refer to Ref. [51]. Hereafter, we use Eq. (2.26) to study the optical response in photodriven systems.

2.1.3 Perturbation expansion

In this section, we discuss the perturbation expansion with respect to the light electronic field $\boldsymbol{E}(t)$. We first develop the equation of the motion for the physical quantity $c_{mn}(\boldsymbol{k})$ that is defined as,

$$c_{mn}(\boldsymbol{k}) = \langle a^\dagger_n(\boldsymbol{k})a_m(\boldsymbol{k})\rangle. \tag{2.33}$$

Using the Heisenberg equation of motion and the Hamiltonian in Eq. (2.16), we obtain the equation of motion for $c_{mn}(\boldsymbol{k})$:

$$\frac{\partial c_{mn}}{\partial t} + i(\omega_m - \omega_n)c_{mn} = \frac{eE^b(t)}{\hbar}c_{mn;b} - \frac{ieE^b(t)}{\hbar}\sum_p(r^b_{mp}c_{pn} - c_{mp}r^b_{pn}), \tag{2.34}$$

where $\omega_m = E_m(\boldsymbol{k})/\hbar$. It is noted that the generalized derivative $c_{mn;b}$ is defined in the same way as in Eq. (2.30). In many cases, it is a good approximation to neglect the term corresponding to the intraband motion $eE^b(t)c_{mn;b}/\hbar$. Hence, in the following, we drop the first term in the right hand side of Eq. (2.34).

Next, we solve the equation of motion in Eq. (2.34) based on the perturbation expansion with respect to $\boldsymbol{E}(t)$. The ground-state expression of $c_{mn}(\boldsymbol{k})$, which corresponds to the solution in the absence of $\boldsymbol{E}(t)$, should be given by,

$$c^{(0)}_{mn} = f_n\delta_{mn}. \tag{2.35}$$

Using Eqs. (2.22), and (2.23), the polarization in the ground state is given by,

$$\langle \boldsymbol{P}(t)\rangle^{(0)} = \langle\Psi|\boldsymbol{P}_{\rm intra}(t) + \boldsymbol{P}_{\rm inter}(t)|\Psi\rangle = -e\sum_n \int \frac{d\boldsymbol{k}}{8\pi^3} f_n \boldsymbol{\xi}_{nn}(\boldsymbol{k}). \tag{2.36}$$

In this equation, the $|\Psi\rangle$ is the ground state of the Hamiltonian H_O. Note that the polarization in the above equation is not dependent on time, so the current $\langle \boldsymbol{J}(t)\rangle^{(0)}$ becomes zero.

Now we discuss the first and second-order terms for $c_{mn}(\boldsymbol{k})$ in terms of the perturbation expansion of $\boldsymbol{E}(t)$. We consider the light electronic field given by,

$$E^b(t) = \sum_\beta E^b_\beta e^{-i\omega_\beta t}. \tag{2.37}$$

By performing the integration with respect to time on Eq. (2.34), we obtain the first order term:

$$c^{(1)}_{mn} = \sum_b \sum_\beta \mathcal{B}^b_{mn} E^b_\beta e^{-i\omega_\beta t}, \tag{2.38}$$

where the quantity $\mathcal{B}^b_{mn}$ is given by,

$$\mathcal{B}^b_{mn} = -\frac{e f_{nm} r^b_{mn}}{\hbar(\omega_{mn} - \omega_\beta)}, \tag{2.39}$$

and f_{mn} and ω_{mn} are defined as $f_{mn} = f_m - f_n$ and $\omega_{mn} = \omega_m - \omega_n$, respectively. Performing the similar integral calculation, we obtain the second order term:

$$c^{(2)}_{mn} = \sum_{b,c}\sum_{\beta,\gamma} \frac{-e}{i\hbar(\omega_{mn} - \omega_\Sigma)} \left[-\mathcal{B}^b_{mn;c} + i\sum_p (r^c_{mp}\mathcal{B}^b_{pn} - \mathcal{B}^b_{mp} r^c_{pn}) \right] E^b_\beta E^c_\gamma e^{-i\omega_\Sigma t}, \tag{2.40}$$

where the frequency ω_Σ is defined as $\omega_\Sigma = \omega_\beta + \omega_\gamma$. In this thesis, we discuss perturbation theory to study the dc photocurrent. The first-order term in Eq. (2.38) does not result in the dc photocurrent because ω_β cannot be zero. On the other hand, the second-order term in Eq. (2.40) can lead to the dc photocurrent when the summation of frequencies $\omega_\Sigma = 0$. Hence, we consider the second-order responses with respect to the light electronic field.

Here, we consider the second-order term for the current density. Using the Eq. (2.26), the intraband contribution to the current density is given by,

$$\langle \boldsymbol{J}_{\rm intra}(t)\rangle^{(2)} = \langle \boldsymbol{J}_{\rm intra}(t)\rangle^{(I)} + \langle \boldsymbol{J}_{\rm intra}(t)\rangle^{(II)}, \tag{2.41}$$

$$\langle J^a_{\rm intra}(t)\rangle^{(I)} = -\frac{e^2}{\hbar}\sum_{n,m}\int \frac{d\boldsymbol{k}}{8\pi^3} c^{(1)}_{mn} r^b_{nm;a} E^b(t), \tag{2.42}$$

$$\langle J^a_{\rm intra}(t)\rangle^{(II)} = -e\sum_n \int \frac{d\boldsymbol{k}}{8\pi^3} c^{(2)}_{nn} v^a_{nn}. \tag{2.43}$$

We first discuss the term $\langle J^a_{\rm intra}(t)\rangle^{(II)}$. Using the second-order term for $c_{mn}(\boldsymbol{k})$ in Eq. (2.40), $\langle J^a_{\rm intra}(t)\rangle^{(II)}$ is given by,

$$\begin{aligned}\langle J^a_{\rm intra}(t)\rangle^{(II)} &= \frac{e^2}{\hbar\omega_\Sigma}\left[\sum_{n,m}\sum_{b,c}\sum_{\beta,\gamma}\int\frac{d\boldsymbol{k}}{8\pi^3}v^a_{nn}(\mathcal{B}^b_{nm}r^c_{mn}-r^c_{nm}\mathcal{B}^b_{mn})\right]E^b_\beta E^c_\gamma e^{-i\omega_\Sigma t}\\ &= -\frac{e^3}{\hbar^2\omega_\Sigma}\left[\sum_{n,m}\sum_{b,c}\sum_{\beta,\gamma}\int\frac{d\boldsymbol{k}}{8\pi^3}f_{nm}\Delta^a_{mn}\frac{r^b_{mn}r^c_{nm}}{\omega_{mn}-\omega_\beta-i\eta}\right]E^b_\beta E^c_\gamma e^{-i\omega_\Sigma t},\end{aligned} \tag{2.44}$$

where we define $\boldsymbol{\Delta}_{mn}$ as $\Delta^a_{mn}=v^a_{mm}(\boldsymbol{k})-v^a_{nn}(\boldsymbol{k})$. Here we have added the small quantity $\eta\,(>0)$ to the frequency ω_β. We symmetrize this term in terms of the conversion $\beta b\leftrightarrow\gamma c$, and then obtain

$$\begin{aligned}\langle J^a_{\rm intra}(t)\rangle^{(II)} = -\frac{e^3}{8\hbar^2\omega_\Sigma}\sum_{n,m}\sum_{b,c}\sum_{\beta,\gamma}\int\frac{d\boldsymbol{k}}{8\pi^3}f_{nm}\Delta^a_{mn}[r^c_{nm},r^b_{mn}]\\ \times[F_+(\omega_{mn},\omega_\beta)-F_+(\omega_{mn},\omega_\gamma)],E^b_\beta E^c_\gamma e^{-i\omega_\Sigma t}.\end{aligned} \tag{2.45}$$

where $[r^c_{nm},r^b_{mn}]\equiv r^c_{nm}r^b_{mn}-r^b_{nm}r^c_{mn}$ and the quantity $F_\pm(\omega_{mn},\omega_\beta)$ is defined as,

$$F_\pm(\omega_{mn},\omega_\beta)=\frac{1}{\omega_{mn}-\omega_\beta-i\eta}\pm\frac{1}{\omega_{mn}+\omega_\beta-i\eta}. \tag{2.46}$$

The factor of $1/(\omega_{mn}-\omega-i\eta)$ in the $F_\pm(\omega_{mn},\omega_\gamma)$ is transformed as,

$$\frac{1}{\omega_{mn}-\omega-i\eta}=\mathcal{P}\frac{1}{\omega_{mn}-\omega}+i\pi\delta(\omega_{mn}-\omega), \tag{2.47}$$

where $\mathcal{P}$ denotes the principle part. Using the above equation, the $\langle J^a_{\rm intra}(t)\rangle^{(II)}$ is given by,

$$\langle J^a_{\rm intra}(t)\rangle^{(II)}=\sum_{b,c}\sum_{\beta,\gamma}\left[\frac{\eta^{abc}_2(-\omega_\Sigma;\omega_\beta,\omega_\gamma)}{-i\omega_\Sigma}+i\tilde{\sigma}^{abc}_{2I}(-\omega_\Sigma;\omega_\beta,\omega_\gamma)\right]E^b_\beta E^c_\gamma e^{-i\omega_\Sigma t}, \tag{2.48}$$

where η^{abc}_2 and $\tilde{\sigma}^{abc}_{2I}$ are defined as,

$$\eta^{abc}_2(-\omega_\Sigma;\omega_\beta,\omega_\gamma)=-\frac{e^3\pi}{8\hbar^2}\sum_{n,m}\int\frac{d\mathbf{k}}{8\pi^3}\Delta^a_{mn}f_{nm}\left[r^c_{nm},r^b_{mn}\right]\left[D_-\left(\omega_{mn},\omega_\beta\right)-D_-\left(\omega_{mn},\omega_\gamma\right)\right], \tag{2.49}$$

$$\tilde{\sigma}^{abc}_{2I}(-\omega_\Sigma;\omega_\beta,\omega_\gamma)=\frac{ie^3}{8\hbar^2\omega_\Sigma}\sum_{n,m}\int\frac{d\mathbf{k}}{8\pi^3}\Delta^a_{mn}f_{nm}\left[r^c_{nm},r^b_{mn}\right]\left[H_+\left(\omega_{mn},\omega_\beta\right)-H_+\left(\omega_{mn},\omega_\gamma\right)\right]. \tag{2.50}$$

Note that η^{abc}_2 is purely imaginary, while $\tilde{\sigma}^{abc}_{2I}$ is real. In these equations, $D_\pm(\omega_{mn},\omega_\beta)$ and $H_\pm(\omega_{mn},\omega_\beta)$ are given by,

$$D_\pm(\omega_{mn},\omega_\beta)=\delta\left(\omega_{mn}-\omega_\beta\right)\pm\delta\left(\omega_{mn}+\omega_\beta\right), \tag{2.51}$$

$$H_\pm(\omega_{mn},\omega_\beta)=\frac{\mathcal{P}}{\omega_{mn}-\omega_\beta}\pm\frac{\mathcal{P}}{\omega_{mn}+\omega_\beta}. \tag{2.52}$$

Next we consider $\langle J^a_{\rm intra}(t)\rangle^{(I)}$ term in Eq. (2.41). By substituting Eq. (2.38) into Eq. (2.42), we obtain

$$\langle J^a_{\rm intra}(t)\rangle^{(I)} = -\frac{e^3}{\hbar^2}\sum_{n,m}\sum_{b,c}\sum_{\beta,\gamma}\int\frac{d\boldsymbol{k}}{8\pi^3}f_{nm}\frac{r^b_{mn}r^c_{nm;a}}{\omega_{mn}-\omega_\beta-i\eta}E^b_\beta E^c_\gamma e^{-i\omega_\Sigma t}. \tag{2.53}$$

In the same way as when we derive Eq. (2.45), we symmetrize Eq. (2.53) in terms of $\beta b \leftrightarrow \gamma c$. Then, the above equation is rewritten as,

$$\langle J^a_{\rm intra}(t)\rangle^{(I)} = -\frac{e^3}{4\hbar^2}\sum_{n,m}\sum_{b,c}\sum_{\beta,\gamma}\int\frac{d\boldsymbol{k}}{8\pi^3}f_{nm}\left\{r^b_{mn}r^c_{nm;a}F_-(\omega_{mn},\omega_\beta) + (bc\beta\gamma \leftrightarrow cb\gamma\beta)\right\}, \tag{2.54}$$

where $(bc\beta\gamma \leftrightarrow cb\gamma\beta)$ indicates a term with the interchange of the indices from (b,c,β,γ) to (c,b,γ,β). Using Eq. (2.47), we obtain

$$\langle J^a_{\rm intra}(t)\rangle^{(I)} = \sum_{b,c}\sum_{\beta,\gamma}[\sigma^{abc}_{2R}(-\omega_\Sigma;\omega_\beta,\omega_\gamma) + i\bar{\sigma}^{abc}_{2I}(-\omega_\Sigma;\omega_\beta,\omega_\gamma)]E^b_\beta E^c_\gamma e^{-i\omega_\Sigma t}, \tag{2.55}$$

where σ^{abc}_{2R} and $\bar{\sigma}^{abc}_{2I}$ are defined as,

$$\sigma^{abc}_{2R}(-\omega_\Sigma;\omega_\beta,\omega_\gamma) = \frac{i\pi e^3}{4\hbar^2}\sum_{n,m}\int\frac{d\mathbf{k}}{8\pi^3}f_{nm}\left\{\left[r^b_{mn}r^c_{nm;a}D_+(\omega_{mn},\omega_\beta)\right] + (bc\beta\gamma \leftrightarrow cb\gamma\beta)\right\}, \tag{2.56}$$

$$\bar{\sigma}^{abc}_{2I}(-\omega_\Sigma;\omega_\beta,\omega_\gamma) = -\frac{ie^3}{4\hbar^2}\sum_{n,m}\int\frac{d\mathbf{k}}{8\pi^3}f_{nm}\left\{\left[r^b_{mn}r^c_{nm;a}H_-(\omega_{mn},\omega_\beta)\right] + (bc\beta\gamma \leftrightarrow cb\gamma\beta)\right\}. \tag{2.57}$$

Note that both σ^{abc}_{2R} and $\bar{\sigma}^{abc}_{2I}$ is real.

Now we move on to the interband current $d\boldsymbol{P}_{\rm inter}(t)/dt$ in Eq. (2.26). The interband contribution to the polarization is given by,

$$\langle \boldsymbol{P}_{\rm inter}(t)\rangle^{(2)} = -e\sum_{n,m}\int\frac{d\boldsymbol{k}}{8\pi^3}c^{(2)}_{mn}\boldsymbol{r}_{nm}. \tag{2.58}$$

By performing the same calculations as when deriving $\langle \boldsymbol{J}_{\rm intra}(t)\rangle$ in Eqs. (2.48) and (2.55), the following results are obtained:

$$\langle P^a_{\rm inter}(t)\rangle^{(2)} = \sum_{b,c}\sum_{\beta,\gamma}[\chi^{abc}_{\rm inter}(-\omega_\Sigma;\omega_\beta,\omega_\gamma) + \tilde{\chi}^{abc}_{\rm intra}(-\omega_\Sigma;\omega_\beta,\omega_\gamma)]E^b_\beta E^c_\gamma e^{-i\omega_\Sigma t}, \tag{2.59}$$

where

$$\chi^{abc}_{\rm inter}\left(-\omega_\Sigma;\omega_\beta,\omega_\gamma\right)=-\frac{e^3}{4\hbar^2}\sum_{b,c}\sum_{\beta,\gamma}\sum_{n,m,p}\int\frac{d\mathbf{k}}{8\pi^3}\left\{\left[\frac{r^a_{nm}r^b_{mp}r^c_{pn}}{\omega_{mp}-\rho_\beta\omega_{mn}}L_{nmp}\left(\omega_\beta,\omega_\gamma\right)\right]\right.$$
$$\left.+\left(bc\beta\gamma\leftrightarrow cb\gamma\beta\right)\right\},\tag{2.60}$$

$$\tilde{\chi}^{abc}_{\rm intra}(-\omega_\Sigma;\omega_\beta,\omega_\gamma)$$
$$=-\frac{ie^3}{4\hbar^2}\sum_{b,c}\sum_{\beta,\gamma}\sum_{n,m}\int\frac{d\mathbf{k}}{8\pi^3}f_{nm}r^a_{nm}\left[\left(\frac{r^b_{mn;c}}{\rho_\gamma\omega_{mn}}-\frac{r^b_{mn}\Delta^c_{mn}}{\rho^2_\gamma\omega^2_{mn}}\right)+\left(bc\beta\gamma\leftrightarrow cb\gamma\beta\right)\right]F_+\left(\omega_{mn},\omega_\Sigma\right)$$
$$-\frac{ie^3}{4\hbar^2}\sum_{b,c}\sum_{\beta,\gamma}\sum_{n,m}\int\frac{d\mathbf{k}}{8\pi^3}f_{nm}\left\{\left[r^b_{mn}\left(\frac{\rho_\beta r^a_{nm;c}}{\rho_\gamma\omega_{mn}}+\frac{\rho^2_\beta r^a_{nm}\Delta^c_{mn}}{\rho^2_\gamma\omega^2_{mn}}\right)F_+\left(\omega_{mn},\omega_\beta\right)\right]+\left(bc\beta\gamma\leftrightarrow cb\gamma\beta\right)\right\}.\tag{2.61}$$

Here we define $L_{nmp}(\omega_\beta,\omega_\gamma)$ as,

$$L_{nmp}(\omega_\beta,\omega_\gamma)=\rho_\beta f_{pm}F_+\left(\omega_{mp},\omega_\beta\right)+\rho_\gamma f_{np}F_+\left(\omega_{pn},\omega_\gamma\right)-f_{nm}F_+\left(\omega_{mn},\omega_\Sigma\right),\tag{2.62}$$

with $\rho_\beta=\omega_\beta/\omega_\Sigma$ and $\rho_\gamma=\omega_\gamma/\omega_\Sigma$.

In conclusion, the second-order term of the current density is represented as,

$$\langle\boldsymbol{J}(t)\rangle^{(2)}=\frac{d\langle\boldsymbol{P}(t)\rangle^{(2)}}{dt},\tag{2.63}$$

where the polarization $\langle\boldsymbol{P}(t)\rangle^{(2)}$ is given by,

$$\langle P^a(t)\rangle^{(2)}=\chi^{abc}_2(-\omega_\Sigma;\omega_\beta,\omega_\gamma)E^b_\beta E^c_\gamma e^{-i\omega_\Sigma t}.\tag{2.64}$$

Here χ^{abc}_2 is divided into two terms:

$$\chi^{abc}_2(-\omega_\Sigma;\omega_\beta,\omega_\gamma)=\chi^{abc}_{\rm inter}(-\omega_\Sigma;\omega_\beta,\omega_\gamma)+\chi^{abc}_{\rm intra}(-\omega_\Sigma;\omega_\beta,\omega_\gamma),\tag{2.65}$$

where $\chi^{abc}_{\rm intra}$ is given by,

$$\chi^{abc}_{\rm intra}(-\omega_\Sigma;\omega_\beta,\omega_\gamma)=\frac{\eta^{abc}_2(-\omega_\Sigma;\omega_\beta,\omega_\gamma)}{(-i\omega_\Sigma)^2}+\frac{\sigma^{abc}_2(-\omega_\Sigma;\omega_\beta,\omega_\gamma)}{-i\omega_\Sigma}$$
$$+\tilde{\chi}^{abc}_{\rm intra}(-\omega_\Sigma;\omega_\beta,\omega_\gamma),\tag{2.66}$$

with $\sigma^{abc}_2=\sigma^{abc}_{2R}+i(\bar{\sigma}^{abc}_{2I}+\tilde{\sigma}^{abc}_{2I})$. It should be noted that there are powers of ω_Σ in the denominators in Eq. (2.66), but in many cases, χ_2 does not diverge when $\omega_\Sigma\to 0$.

We now consider the second-order optical responses when the system is irradiated with light $\boldsymbol{E}(t)=\boldsymbol{E}(\omega)e^{-i\omega t}+\boldsymbol{E}(-\omega)e^{i\omega t}$. We first consider the contribution from

$\eta_2^{abc}(0;\omega,-\omega)$ in Eq. (2.66). We write the contribution from η_2^{abc} as $\langle \boldsymbol{J}_{\rm injection}\rangle^{(2)}$. Using Eqs. (2.49) and (2.66), $\langle \boldsymbol{J}_{\rm injection}\rangle^{(2)}$ is given by,

$$\begin{aligned}\frac{d\langle J^a_{\rm injection}\rangle^{(2)}}{dt} =& \sum_{b,c}\left[\eta_2^{abc}(0;\omega,-\omega)E^b(\omega)E^c(-\omega)+\eta_2^{abc}(0;-\omega,\omega)E^b(-\omega)E^c(\omega)\right]\\ =& \sum_{b,c}\left[\eta_2^{abc}(0;\omega,-\omega)E^b(\omega)E^c(-\omega)+\text{c.c.}\right]\\ =& 2\sum_{b,c}\eta_2^{abc}(0;\omega,-\omega)E^b(\omega)E^c(-\omega),\end{aligned} \tag{2.67}$$

where $\eta_2^{abc}(0;\omega,-\omega)$ is given by,

$$\eta_2^{abc}(0;\omega,-\omega) = -\frac{e^3\pi}{2\hbar^2}\sum_{n,m}\int\frac{d\mathbf{k}}{8\pi^3}\Delta^a_{mn}f_{nm}\left[r^c_{mn},r^b_{nm}\right]\delta\left(\omega_{mn}-\omega\right). \tag{2.68}$$

It is evident that this term corresponds to the injection of current induced by the irradiation of the light $\boldsymbol{E}(t)$. Note that this term becomes zero when we consider the smaller frequency compared to the bandgap energy. We also note that the same equation for the injection current can be derived by using the Fermi's Golden Rule. This indicates that the injection current is attributed to the interference via one-photon absorption process [see Appendix A]. As explained earlier, the irradiation with linearly polarized light results in the vanishing the injection current when the system has the time-reversal symmetry.

Next, we consider the contribution from $\sigma_2^{abc}(0;\omega,-\omega)$ to the dc photocurrent. As shown in Eqs. (2.48) and (2.55), there are a real and an imaginary part in $\sigma_2^{abc}(0;\omega,-\omega)$. However, when we consider the case of $\omega_\Sigma = 0$, the imaginary part disappears. Therefore, we only consider the contribution from σ_{2R}^{abc} in Eq. (2.55). We call this contribution as shift current and write as $\langle \boldsymbol{J}_{\rm shift}\rangle^{(2)}$. In the same way as the injection current in Eq. (2.67), the shift current $\langle \boldsymbol{J}_{\rm shift}\rangle^{(2)}$ is given by,

$$\langle J^a_{\rm shift}\rangle^{(2)} = 2\sum_{b,c}\sigma_2^{abc}(0;\omega,-\omega)E^b(\omega)E^c(-\omega), \tag{2.69}$$

where

$$\sigma_2^{abc}(0;\omega,-\omega) = \frac{i\pi e^3}{2\hbar^2}\sum_{n,m}\int\frac{d\boldsymbol{k}}{8\pi^3}f_{nm}(r^b_{mn}r^c_{nm;a}+r^c_{mn}r^b_{nm;a})\delta(\omega_{mn}-\omega). \tag{2.70}$$

This shift current appears because the charge distribution in real space is different between the valence band and the conduction band. Consequently, upon light irradiation, a charge shift occurs when electrons transfer from the valence band to the conduction band. The "shift" of the center of charge results in a net current generation if the crystal's symmetry is low enough. In the following, we consider the component of $\sigma_2^{abb}(0;\omega,-\omega)$. We divide $r^b_{nm}(\boldsymbol{k})$ into the phase factor and the absolute part as,

$$r^b_{nm}(\boldsymbol{k}) = |r^b_{nm}(\boldsymbol{k})|e^{-i\phi_{nm}(\boldsymbol{k})}. \tag{2.71}$$

Then, Eq. (2.70) is transformed as,

$$\sigma_2^{abb}(0;\omega,-\omega) = -\frac{\pi e^3}{\hbar^2}\sum_{n,m}\int \frac{d\boldsymbol{k}}{8\pi^3} f_{nm} S^a_{nm} |r^b_{nm}|^2 \delta(\omega_{mn}-\omega), \tag{2.72}$$

where the shift vector $S^a_{nm}(\boldsymbol{k})$ is defined as,

$$S^a_{nm}(\boldsymbol{k}) = \frac{\partial \phi_{nm}(\boldsymbol{k})}{\partial k^\alpha} + \xi^a_{nn}(\boldsymbol{k}) - \xi^a_{mm}(\boldsymbol{k}). \tag{2.73}$$

Note that this shift vector corresponds to the change of the position of an electron in real-space when the light is irradiated. We also note that Eq. (2.73) is gauge-invariant although the Berry connection $\xi^a_{nn}(\boldsymbol{k})$ is not gauge-invariant.

Lastly, we mention the contribution from $\chi_{\rm inter}(0;\omega,-\omega)$ and $\chi_{\rm intra}(0;\omega,-\omega)$, which arises from the interband polarization. They corresponds to the dc polarization resulting from the mixing of the vector potentials with frequencies ω and $-\omega$. However, they do not contribute to the dc photocurrent when $\omega_\Sigma \to 0$ [see Eq. (2.66)]. Therefore, in Chap. 4, we focus solely on the shift current and injection current.

2.2 Floquet theory

In this section, we discuss Floquet theory as a method to study the nonperturbative effect induced by irradiation with light. We begin with the Floquet theorem, which is a temporal version of the Bloch theorem, and then explore the approach to derive a static effective Hamiltonian [85]. Furthermore, we obtain the Floquet effective Hamiltonian for a photodriven tight-binding model in Sec. 2.2.3. The content in Sec. 2.2.3 is based on our previous study in Ref. [80].

2.2.1 Floquet theorem

In this section, we introduce a general formalism of the Floquet theory for photo-irradiated systems. The photodriven systems are described by the time dependent Schrödinger equation given by,

$$i\hbar\frac{\partial}{\partial\tau}\left|\Psi(\tau)\right\rangle = H(\tau)\left|\Psi(\tau)\right\rangle. \tag{2.74}$$

Here the Hamiltonian $H(\tau)$ is time-periodic as $H(\tau)=H(\tau+T)$ with a temporal period $T(=2\pi/\omega)$ of the light. In such systems, the wave function $|\Psi(\tau)\rangle$ can be written in the form,

$$\left|\Psi(\tau)\right\rangle = e^{-i\varepsilon\tau/\hbar}\left|\Phi(\tau)\right\rangle, \tag{2.75}$$

where ε and $|\Phi(\tau)\rangle$ are referred to as the quasienergy and the Floquet state, respectively. The Floquet state satisfies $|\Phi(\tau)\rangle = |\Phi(\tau+T)\rangle$. This theorem is called Floquet theorem and can be regarded as a temporal version of the Bloch theorem for spatially periodic systems. We substitute Eq. (2.75) into Eq. (2.74) and perform the Fourier transformations

with respect to time. Eventually, the time dependent Schrödinger equation is transformed in the form,

$$\sum_{m=-\infty}^{\infty} \mathcal{H}_{nm} \left|\Phi_\nu^m\right\rangle = \varepsilon_\nu^n \left|\Phi_\nu^n\right\rangle, \tag{2.76}$$

where

$$\mathcal{H}_{nm} = H_{n-m} - m\omega\delta_{n,m}. \tag{2.77}$$

Here the Fourier coefficients H_n and $|\Phi_\nu^n\rangle$ are defined as

$$H_n = \frac{1}{T}\int_0^T H(\tau)e^{in\omega\tau}d\tau, \tag{2.78}$$

$$\left|\Phi_\nu^n\right\rangle = \frac{1}{T}\int_0^T \left|\Phi_\nu(\tau)\right\rangle e^{in\omega\tau}d\tau. \tag{2.79}$$

The eigenvalue equation in Eq. (2.76) can be rewritten in the matrix form given by,

$$\begin{pmatrix} \ddots & & & & \\ & H_0-\omega & H_1 & H_2 & \\ & H_{-1} & H_0 & H_1 & \\ & H_{-2} & H_{-1} & H_0+\omega & \\ & & & & \ddots \end{pmatrix} \begin{pmatrix} \vdots \\ |\Phi_\alpha^1\rangle \\ |\Phi_\alpha^0\rangle \\ |\Phi_\alpha^{-1}\rangle \\ \vdots \end{pmatrix} = \varepsilon_\alpha \begin{pmatrix} \vdots \\ |\Phi_\alpha^1\rangle \\ |\Phi_\alpha^0\rangle \\ |\Phi_\alpha^{-1}\rangle \\ \vdots \end{pmatrix}. \tag{2.80}$$

In this thesis, we refer to the matrix in Eq. (2.80) as Floquet Hamiltonian. It is noted that there is no time dependence in the eigenvalue equation in Eq. (2.80), but this eigenvalue equation is infinite-dimensional. More precisely, using the Floquet theorem, solving the time-dependent Schrödinger equation [Eq. (2.74)] in a Hilbert space $\mathbb{H}$ is transformed into the static eigenvalue equation in an expanded Hilbert space $\mathbb{H}\otimes\mathbb{T}$, where $\mathbb{T}$ is the Hilbert space for the periodic drive. The integer n in $\mathbb{T}$ corresponds to the number of photons, and $|\Phi_\nu^{-n}\rangle$ is interpreted as a state dressed with n photons [85].

It is obvious that the number of eigenvalues in Eq. (2.80) is $\dim \mathbb{H}\otimes\mathbb{T}$. However, there is redundancy in a set of eigenvalues and eigenvectors. When ε_α and $\{|\Phi_\alpha^m\rangle\}$ are an eigenvalue and an eigenvector of the eigenvalue equation in Eq. (2.80), then $\varepsilon_\alpha + n\omega$ and $\{|\Phi_\alpha^{m+n}\rangle\}$ also become the eigenvalue and the eigenvector that corresponds to the same physical state as ε_α and $\{|\Phi_\alpha^m\rangle\}$. In addition, solutions with eigenvalues that differ only $n\omega$ correspond to the same physical state, as shown in Eq. (2.75). Therefore, it is sufficient to obtain the eigenvalues that belongs to the set $\Lambda = [-\omega/2, \omega/2)$. Here, the set Λ is referred to as the Floquet Brillouin zone.

2.2.2 Floquet effective Hamiltonian

In this section, we construct the static Floquet effective Hamiltonian corresponding to the quasienergy within the Floquet Brillouin zone $\Lambda = [-\omega/2, \omega/2)$. There are several

ways to construct a Floquet effective Hamiltonian. In the following, we introduce the Floquet effective Hamiltonian derived by Brillouin-Wigner theory [85].

We first define the projection operator and wave operator. The projection operator is given by $[\mathcal{P}]_{m,n} = \delta_{m,n}\delta_{m,0}$, and the wave operator $\Omega(\varepsilon)$ is defined as follows:

$$|\boldsymbol{\Phi_\alpha}\rangle = \Omega(\varepsilon)\mathcal{P}\,|\boldsymbol{\Phi_\alpha}\rangle\,. \tag{2.81}$$

It should be noted that this equation does not hold for all α, but it works for at most $\dim \mathcal{P}$ eigenvectors. In the following, we consider the projection of the Floquet Hamiltonian to the zero-photon substate. Using the projection operator and wave operator, the Floquet effective Hamiltonian is given by,

$$H_{\text{eff}} = \mathcal{P}\mathcal{H}\Omega(\varepsilon)\mathcal{P}, \tag{2.82}$$

where $\mathcal{H}$ and $\mathcal{M}$ are defined as $[\mathcal{H}]_{n,m} = H_{n-m} - m\omega\delta_{n,m}$ and $[\mathcal{M}]_{n,m} = m\delta_{n,m}$, respectively. The reason why the effective Hamiltonian can be expressed in Eq. (2.82) is that the eigenvalue and eigenvector of H_{eff} can be derived using the following calculation:

$$\begin{aligned} H_{\text{eff}}\mathcal{P}\,|\Phi_\alpha\rangle &= \mathcal{P}\mathcal{H}\Omega(\varepsilon)\mathcal{P}\,|\Phi_\alpha\rangle \\ &= \mathcal{P}\mathcal{H}\,|\Phi_\alpha\rangle \\ &= \varepsilon_\alpha\mathcal{P}\,|\Phi_\alpha\rangle\,. \end{aligned} \tag{2.83}$$

Note that $\mathcal{P}^2 = \mathcal{P}$ holds by definition. This calculation shows that the eigenvalue and eigenvector of H_{eff} are ε_α and $|\Phi_\alpha\rangle$, respectively.

In the following, we consider the method for calculating the wave operator $\Omega(\varepsilon)$. Note that once we obtain the wave operator, the effective Hamiltonian can be derived using Eq. (2.82). To obtain the wave operator $\Omega(\varepsilon)$, we consider the projection of $(1-\mathcal{P})$ onto the Floquet state $|\Phi_\alpha\rangle$ and we find $|\Phi_\alpha\rangle$ can be expressed as,

$$\begin{aligned} |\boldsymbol{\Phi_\alpha}\rangle &= \mathcal{P}\,|\boldsymbol{\Phi_\alpha}\rangle + \frac{1-\mathcal{P}}{\mathcal{M}\omega}(\mathcal{H}+\mathcal{M}\omega-\varepsilon_\alpha)\,|\boldsymbol{\Phi_\alpha}\rangle \\ &= \left(1 - \frac{1-\mathcal{P}}{\mathcal{M}\omega}(\mathcal{H}+\mathcal{M}\omega-\varepsilon_\alpha)\right)^{-1}\mathcal{P}\,|\boldsymbol{\Phi_\alpha}\rangle\,. \end{aligned} \tag{2.84}$$

Therefore, we obtain the wave operator $\Omega(\varepsilon)$ and the Floquet effective Hamiltonian $H_{\text{eff}}(\varepsilon)$ as,

$$\Omega(\varepsilon) = \left(1 - \frac{1-\mathcal{P}}{\mathcal{M}\omega}(\mathcal{H}+\mathcal{M}\omega-\varepsilon)\right)^{-1}\mathcal{P}, \tag{2.85}$$

$$H_{\text{eff}}(\varepsilon) = \mathcal{P}\mathcal{H}\left(1 - \frac{1-\mathcal{P}}{\mathcal{M}\omega}(\mathcal{H}+\mathcal{M}\omega-\varepsilon)\right)^{-1}\mathcal{P}. \tag{2.86}$$

It should be noted that the effective Hamiltonian is dependent on ε. The number of eigenvalues of $H_{\text{eff}}(\varepsilon)$ in Eq. (2.86) is $\dim \mathbb{H}$, but each eigenvalue contains the information of $\dim \mathbb{T}$ eigenvalues by considering the solution of the equation $\varepsilon = E_i(\varepsilon)$. Therefore, we can consider $\dim \mathbb{H}\otimes\mathbb{T}$ eigenvalues by using the effective Hamiltonian in Eq. (2.86).

However, when we exclude the dependence of ε in the effective Hamiltonian by taking a perturbation, we can only consider the $\dim \mathbb{H}$ eigenvalues. In other words, the eigenvalues of the effective Hamiltonian without the dependence of ε are not unique, and they are determined by the way of eliminating the dependence of ε.

In the following, we consider a method of eliminating the dependence of ε to derive the effective Hamiltonian from which all quasienergies belonging to the FBZ are able to be obtained. Equation (2.85) is transformed as,

$$\Omega(\varepsilon) = \mathcal{P} + \frac{1-\mathcal{P}}{\mathcal{M}\omega}(\mathcal{H} + \mathcal{M}\omega)\Omega(\varepsilon) - \frac{1-\mathcal{P}}{\mathcal{M}\omega}\Omega(\varepsilon)\varepsilon. \tag{2.87}$$

In addition, we can conduct the calculation as,

$$\begin{aligned} \varepsilon_\alpha \mathcal{P}\left|\Phi_\alpha\right\rangle &= H_{\text{eff}}\mathcal{P}\left|\Phi_\alpha\right\rangle \\ &= \mathcal{P}\mathcal{H}\Omega(\varepsilon)\mathcal{P}\left|\Phi_\alpha\right\rangle. \end{aligned} \tag{2.88}$$

This indicates that we can replace ε with $\mathcal{P}\mathcal{H}\Omega(\varepsilon)$. Therefore, the wave operator without the dependence of ε is obtained as,

$$\Omega = \mathcal{P} + \frac{1-\mathcal{P}}{\mathcal{M}\omega}(\mathcal{H} + \mathcal{M}\omega)\Omega - \frac{1-\mathcal{P}}{\mathcal{M}\omega}\Omega\mathcal{P}\mathcal{H}\Omega. \tag{2.89}$$

We can solve this equation and obtain the wave operator Ω self-consistently. The perturbative expansion of the wave operator Ω with respect to $1/\omega$ is derived as,

$$\Omega_{\text{BW}} = \sum_{N=0}^{\infty} \Omega_{BW}^{(N)}, \tag{2.90}$$

$$\Omega_{\text{BW}}^{(0)} = \mathcal{P}, \tag{2.91}$$

$$\Omega_{\text{BW}}^{(1)} = \frac{1-\mathcal{P}}{\mathcal{M}\omega}\mathcal{H}\mathcal{P}, \tag{2.92}$$

$$\Omega_{\text{BW}}^{(N+1)} = \frac{1-\mathcal{P}}{\mathcal{M}\omega}(\mathcal{H} + \mathcal{M}\omega)\Omega_{\text{BW}}^{(N)} - \sum_{M=1}^{N} \frac{1-\mathcal{P}}{\mathcal{M}\omega}\Omega_{\text{BW}}^{(M)}\mathcal{P}\mathcal{H}\Omega_{\text{BW}}^{(N-M)}. \tag{2.93}$$

Here we use the equations $(1-\mathcal{P})\mathcal{P} = 0$ and $\mathcal{P}\mathcal{M} = 0$. Using the above equation, we obtain the Floquet effective Hamiltonian H_{BW} as,

$$H_{\text{BW}} = \sum_{N=0}^{\infty} H_{\text{BW}}^{(N)}, \tag{2.94}$$

$$H_{\text{BW}}^{(0)} = H_0, \tag{2.95}$$

$$H_{\text{BW}}^{(1)} = \sum_{n\neq 0} \frac{H_{-n}H_n}{n\omega}, \tag{2.96}$$

$$H_{\text{BW}}^{(2)} = \sum_{n_1\neq 0}\sum_{n_2\neq 0}\left(\frac{H_{-n_1}H_{n_1-n_2}H_{n_2}}{n_1 n_2\omega^2} - \frac{H_{-n_1}H_{n_1}H_0}{n_1^2\omega^2}\right). \tag{2.97}$$

It should be noted that the effective Hamiltonian $H_{\rm BW}$ produces all the quasienergies in the FBZ and eigenvectors projected to the zero-photon subspace $|\Phi^0_\alpha\rangle = \mathcal{P}\,|\mathbf{\Phi}_\alpha\rangle$.

If we only consider the first order of $1/\omega$, we obtain the effective Hamiltonian $H_{\rm BW}$,

$$H_{\rm eff} = H_0 + \sum_{n=1}^{\infty} \frac{[H_{-n}, H_n]}{n\omega} + O\left(\frac{W^3}{\omega^2}\right). \tag{2.98}$$

Here W refers to the bandwidth of the system. This effective Hamiltonian is valid when the light frequency ω is high enough compared to the bandwidth W. It should be noted that the following approximated form, in which only the first term of the series expansion is taken, is often used in the high-frequency limit,

$$H_{\rm eff} \sim H_0 + \frac{[H_{-1}, H_1]}{\hbar\omega}. \tag{2.99}$$

2.2.3 Floquet theory of photodriven tight-binding model

In this section, we consider the following tight-binding model that describes a lattice electron system,

$$H = \sum_{i,j} t_{ij} c_i^\dagger c_j, \tag{2.100}$$

where i and j refer to the lattice sites. The symbol $c_i^\dagger$ (c_i) represents the creation (annihilation) operator of an electron at ith site, while t_{ij} denotes the transfer integral between ith and jth sites. When the system is irradiated with light, the transfer integrals attain Peierls phases due to the time-dependent vector potential of light electromagnetic field. A general equation for the vector potential caused by the elliptically polarized light is given by,

$$\boldsymbol{A}(\tau) = (A_x \sin(\omega\tau + \phi), A_y \sin(\omega\tau)), \tag{2.101}$$

where ϕ denotes the phase difference between the x-component and y-component. This vector potential gives a time-dependent electric field

$$\begin{aligned} \boldsymbol{E}(\tau) &= -\frac{d\boldsymbol{A}(\tau)}{d\tau} \\ &= -(A_x\omega\cos(\omega\tau + \phi), A_y\omega\cos(\omega\tau)). \end{aligned} \tag{2.102}$$

The transfer integrals with a time-dependent Peierls phase are given by

$$\begin{aligned} t_{ij}(\tau) &= t_{ij} \exp\left[-i\frac{e}{\hbar}\boldsymbol{A}(\tau)\cdot(\boldsymbol{r}_i - \boldsymbol{r}_j)\right] \\ &= t_{ij} \exp\left[-i\frac{e}{\hbar}A_x(x_i - x_j)\sin(\omega\tau + \phi) - i\frac{e}{\hbar}A_y(y_i - y_j)\sin(\omega\tau)\right]. \end{aligned} \tag{2.103}$$

Here we introduce the coordinates $\boldsymbol{r}_i = (x_i, y_i)$ for ith site.

The Fourier coefficients H_n are calculated using Eq. (2.78) as

$$H_n = \sum_{i,j} t_{ij} J_n(\mathcal{A}_{ij}) e^{-in\theta_{ij}} c_i^\dagger c_j. \tag{2.104}$$

Here J_n is the nth Bessel function, and $\mathcal{A}_{ij}$ and θ_{ij} are respectively defined as

$$\mathcal{A}_{ij} = \frac{e}{\hbar}[A_x^2(x_i - x_j)^2 + A_y^2(y_i - y_j)^2 + 2A_xA_y(x_i - x_j)(y_i - y_j)\cos\phi]^{1/2} \tag{2.105}$$

$$\theta_{ij} = \tan^{-1}\left[\frac{A_x(x_i - x_j)\sin\phi}{A_x(x_i - x_j)\cos\phi + A_y(y_i - y_j)}\right]. \tag{2.106}$$

The second term of H_{eff} in Eq. (2.98) is given by,

$$\sum_{n=1}^{\infty}\frac{[H_{-n}, H_n]}{n\hbar\omega} = \sum_{\langle\langle i,k\rangle\rangle}\sum_{n=1}^{\infty}\frac{2i}{n\hbar\omega}\sum_j \mathrm{Im}(\chi_{ij}^{-n}\chi_{jk}^{n})(c_i^\dagger c_k - c_k^\dagger c_i), \tag{2.107}$$

where we define

$$\chi_{ij}^{n} \equiv t_{ij}J_n\left(\mathcal{A}_{ij}\right)e^{-in\theta_{ij}}. \tag{2.108}$$

This term describes next-nearest-neighbor electron hoppings between ith and kth sites via the in-between jth site connected by two transfer integrals t_{ij} and t_{jk}. On the other hand, the first term H_0 of H_{eff} in Eq. (2.98) is given by,

$$H_0 = \sum_{i,j} t_{ij}J_0(\mathcal{A}_{ij})c_i^\dagger c_j. \tag{2.109}$$

This term describes the nearest-neighbor electron hoppings between ith and jth sites connected by a single transfer integral t_{ij}, which are renormalized by the Bessel function $J_0(\mathcal{A}_{ij})$. It should be noted that the effective Hamiltonian obtained by substituting Eqs. (2.107) and (2.109) into the Eq. (2.98) represents a general equation applicable to photodriven systems and is not specific to the organic salt α-(BEDT-TTF)$_2$I$_3$.

Chapter 3

Photoinduced topological phase transition in α-(BEDT-TTF)$_2$I$_3$

As introduced in Chap. 1, most of the previous research on photoinduced tological phase transitions using Floquet theory has dealt with tight-binding models on simple lattices, and there have been few studies based on realistic models for specific materials. On the other hand, to further develop this promising research field, widening the range of target materials is indispensable, and towards this objective, theoretical studies on actual materials with complex electronic and crystalline structures are highly desired. Moreover, we can expect richer material-specific photoinduced topological phenomena in studies on actual materials. One promising material is an organic salt α-(BEDT-TTF)$_2$I$_3$, where BEDT-TTF denotes bis(ethylenedithio)-tetrathiafulvalene [86]. This compound has tilted Dirac cones in its band structure [78, 87, 88], and many interesting topological properties and phenomena rising from these Dirac-cone bands have been investigated so far.

In this chapter, we discuss our recent theoretical studies that predicted novel phenomena and rich phases in photodriven organic salt α-(BEDT-TTF)$_2$I$_3$. By analyzing a photodriven tight-binding model describing conduction electrons in the BEDT-TTF layer using the Floquet theorem, we demonstrate three topological phase transitions in photodriven α-(BEDT-TTF)$_2$I$_3$, (1) topological phase transition to the Chern insulator induced by circularly polarized light [Section 3.2], (2) pair annihilation of emergent magnetic charges induced by linearly polarized light [Section 3.3], and (3) novel type of photoinduced topological phase transition accompanied by collision and collapse of two Dirac cones [Section 3.4]. The content of this chapter is published in Ref. [79, 80, 81, 82].

3.1 Model for photodriven α-(BEDT-TTF)$_2$I$_3$

3.1.1 Tight-binding model

In this section, we develop a tight-binding model for the organic conductor α-(BEDT-TTF)$_2$I$_3$ in the absence of the light irradiation. Figure 3.1 illustrates the crystal structure of α-(BEDT-TTF)$_2$I$_3$, where layers of BEDT-TTF$^{+1/2}$ molecules are stacked alternately with layers of I_3^{-1} molecules. Typically, crystals made up of molecules are insulators.

However, in the case of this material, a unique electron transfer process occurs. The I_3 molecule receives an electron from the BEDT-TTF molecule, leading to the formation of closed-shell electron structures I_3^{-1} that contribute to the stabilization of the crystal. As a consequence of this electron transfer, one-quarter of the electrons per spin in the BEDT-TTF HOMO band shift to the I_3 band, while the remaining three-quarters of the electrons per spin remain in the BEDT-TTF HOMO band. Since the wave functions overlap with adjacent molecules, electrons in the BEDT-TTF layers are able to move within the layer. In contrast, the I_3^{-1} layer's band is located well below the Fermi energy due to the closed-shell structure. As the BEDT-TTF layers are separated by the I_3^{-1} layer, the probability of electrons to transfer along the c-axis is minimal. Thus, this system is often referred to as a quasi-two-dimensional system. In this thesis, we treat this material as an ideal two-dimensional system.

This material exhibits a horizontal-stripe charge order stabilized by the long-range Coulomb interactions under ambient pressure [89, 90, 91, 92]. However, this charge order disappears when a uniaxial pressure, $P_a(> 4$ kbar), is applied or when the temperature exceeds 135 K. At that point, the system transforms into a Dirac semimetal with a pair of gapless Dirac-cone bands whose Dirac points are situated at the Fermi level [86, 87]. In this thesis, we focus on scenarios where uniaxial pressure is applied, resulting in either a gapless Dirac semimetal or a Dirac semimetal with a small gap in this material. It's important to note that the gap of the Dirac cones in its band structure can be adjusted by applying the appropriate uniaxial pressure to this material.

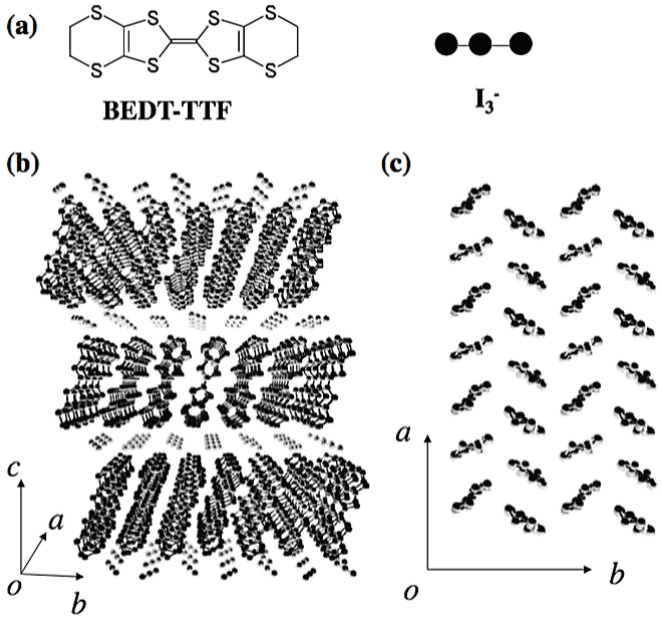

Figure 3.1. (a) BEDT-TTF molecule and I_3^- anions. (b) Crystal structure of α-(BEDT-TTF)$_2$I$_3$ viewed from the a axis. BEDT-TTF layers and I_3 layers are stacked alternately. (c) The crystal structure viewed from the c axis. Adapted from Ref. [86].

Figure 3.2(a) shows the crystal structure of quasi-two-dimensional BEDT-TTF lay-

ers in α-(BEDT-TTF)$_2$I$_3$. We employ a tight binding model to describe the electronic structure in the BEDT-TTF layer, which is given by,

$$H = \sum_{i,j} \sum_{\alpha,\beta} t_{i\alpha,j\beta} c^{\dagger}_{i,\alpha} c_{j,\beta} + \Delta \sum_{i} (c^{\dagger}_{i,\mathrm{A}} c_{i,\mathrm{A}} - c^{\dagger}_{i,\mathrm{A}'} c_{i,\mathrm{A}'}). \tag{3.1}$$

In this equation, i, j refer to the unit cells, while α and β label the molecular sites (A, A$'$, B, and C). The symbol $c^{\dagger}_{i,\alpha}(c_{i,\alpha})$ represents the electron creation (annihilation) operator, and $t_{i\alpha,j\beta}$ denotes transfer integrals between neighboring sites. In Eq. (3.1), we introduce a staggered site potential ($\Delta > 0$) as an order parameter for the charge order in a mean-field theory [90]. When the charge order completely melts ($\Delta = 0$), two tilted Dirac cones emerge between the third and fourth bands. Meanwhile, when the compound is in the charge order phase ($\Delta > 0$), the tilted Dirac cones become gapped at the Dirac points, as confirmed by various experiments [93, 94]. The P_a dependencies of the eight transfer integrals in Fig. 3.2 are deduced theoretically by interpolation: $t_{a1} = -0.028(1.00{+}0.089P_a)$ eV, $t_{a2} = 0.048(1.0{+}0.167P_a)$ eV, $t_{a3} = -0.020(1.0{-}0.025P_a)$ eV, $t_{b1} = 0.123$ eV, $t_{b2} = 0.140(1.0 + 0.011P_a)$ eV, $t_{b3} = -0.062(1.0 + 0.032P_a)$ eV, and $t_{b4} = -0.025$ eV [95]. In this thesis, we assume that $P_a = 4$ kbar.

After performing the Fourier transformations with respect to the spatial coordinates, the tight-binding Hamiltonian is converted into the momentum space as

$$H = \sum_{\boldsymbol{k}} (c^{\dagger}_{\boldsymbol{k}A}\, c^{\dagger}_{\boldsymbol{k}A'}\, c^{\dagger}_{\boldsymbol{k}B}\, c^{\dagger}_{\boldsymbol{k}C}) H(\boldsymbol{k}) \begin{pmatrix} c_{\boldsymbol{k}A} \\ c_{\boldsymbol{k}A'} \\ c_{\boldsymbol{k}B} \\ c_{\boldsymbol{k}C} \end{pmatrix}, \tag{3.2}$$

where

$$H(\boldsymbol{k}) = \begin{pmatrix} \Delta & A_2 & B_2 & B_1 \\ A_2^* & -\Delta & B_2^* & B_1^* \\ B_2^* & B_2 & 0 & A_1 \\ B_1^* & B_1 & A_1 & 0 \end{pmatrix}, \tag{3.3}$$

with

$$A_1 = 2t_{a1} \cos(k_y a/2), \tag{3.4}$$
$$A_2 = t_{a2} e^{ik_y a/2} + t_{a3} e^{-ik_y a/2}, \tag{3.5}$$
$$B_1 = t_{b1} e^{i(k_x b/2 + k_y a/4)} + t_{b4} e^{-i(k_x b/2 - k_y a/4)}, \tag{3.6}$$
$$B_2 = t_{b2} e^{i(k_x b/2 - k_y a/4)} + t_{b3} e^{-i(k_x b/2 + k_y a/4)}. \tag{3.7}$$

Here b and a are the lattice constants along the x and y axes, respectively [Fig. 3.2(a)]. Figure 3.2(c) displays the band structure obtained by diagonalizing the matrix of the tight-binding Hamiltonian in Eq. (3.3) when $\Delta = 0$. As mentioned earlier, two Dirac-cone bands emerge in its band structure, leading to the discovery of various intriguing phenomena, such as the flux-induced Chern insulator phases [96], prediction of nonlinear anomalous thermoelectric effect [97], and observation of freezing of charge motion [98]. It's worth noting that these Dirac cones differ from those in graphene in that they are tilted and lack rotational symmetry.

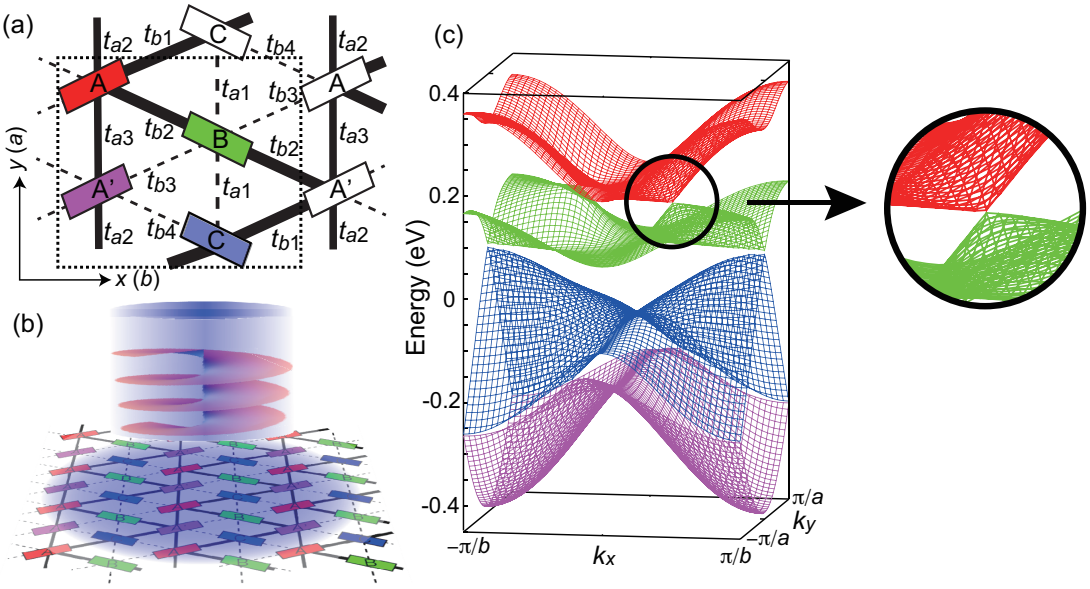

Figure 3.2. (a) Quasi-two-dimensional conduction layer of α-(BEDT-TTF)$_2$I$_3$. The dashed rectangle represents a unit cell composed of four molecules (A, A′, B, and C) and eight kinds of transfer integrals. (b) Schematic of α-(BEDT-TTF)$_2$I$_3$ under the irradiation with circularly polarized light. (c) Band structure of α-(BEDT-TTF)$_2$I$_3$ obtained from a tight-binding model for two-dimensional BEDT-TTF layer. There exists a pair of tilted Dirac cones between the valence band (third band) and the condcution band (the fourth band). Adapted from our previous study in Ref. [79, 81].

3.1.2 Floquet Hamiltonian for photodriven α-(BEDT-TTF)$_2$I$_3$

In this section, we construct the Floquet Hamiltonian for α-(BEDT-TTF)$_2$I$_3$ under the irradiation with light. We consider the model where the light is irradiated perpendicularly to the BEDT-TTF layer in α-(BEDT-TTF)$_2$I$_3$ [Fig. 3.2(b)]. As explained in the previous chapter, a general form of the vector potential caused by the elliptically polarized light is given by Eq. (2.101). Here we introduce dimensionless amplitude $\mathcal{A}_b$ and $\mathcal{A}_a$ as,

$$\mathcal{A}_a = \frac{eaA_y}{\hbar}, \qquad \mathcal{A}_b = \frac{ebA_x}{\hbar}. \tag{3.8}$$

Note that amplitudes of the two electric-field components E_a^ω and E_b^ω for the elliptically polarized light are given by,

$$E_a^\omega = A_y\omega = \frac{\mathcal{A}_a\hbar\omega}{ea}, \qquad E_b^\omega = A_x\omega = \frac{\mathcal{A}_b\hbar\omega}{eb}. \tag{3.9}$$

For the Hamiltonian in the momentum representation, the effects of irradiation with elliptically polarized light can be treated simply by replacing the momenta k_x and k_y as

$$k_x \quad \to \quad k_x + \mathcal{A}_b \sin(\omega\tau + \phi), \tag{3.10}$$
$$k_y \quad \to \quad k_y + \mathcal{A}_a \sin(\omega\tau). \tag{3.11}$$

It is straightforward to obtain the Fourier coefficients of the Hamiltonian H_n for α-(BEDT-TTF)$_2$I$_3$ as in Eq. (2.104). The transfer integrals $t_{i\alpha,j\beta}$ are renormalized as

$$t_{a1} \quad \to \quad t_{a1}J_n(\mathcal{A}_a/2), \tag{3.12}$$
$$\tilde{t}_{a1} \quad \to \quad \tilde{t}_{a1}J_{-n}(\mathcal{A}_a/2), \tag{3.13}$$
$$t_{a2} \quad \to \quad t_{a2}J_{-n}(\mathcal{A}_a/2), \tag{3.14}$$
$$t_{a3} \quad \to \quad t_{a3}J_n(\mathcal{A}_a/2), \tag{3.15}$$
$$t_{b1} \quad \to \quad t_{b1}J_{-n}(\mathcal{A}_+)e^{-in\theta_+}, \tag{3.16}$$
$$t_{b2} \quad \to \quad t_{b2}J_n(\mathcal{A}_-)e^{+in\theta_-}, \tag{3.17}$$
$$t_{b3} \quad \to \quad t_{b3}J_n(\mathcal{A}_+)e^{-in\theta_+}, \tag{3.18}$$
$$t_{b4} \quad \to \quad t_{b4}J_{-n}(\mathcal{A}_-)e^{+in\theta_-}. \tag{3.19}$$

Here we define $\mathcal{A}_\pm$ and $\theta_\pm$ as

$$\mathcal{A}_\pm = \frac{1}{4}\sqrt{4\mathcal{A}_b^2 + \mathcal{A}_a^2 \pm 4\mathcal{A}_a\mathcal{A}_b\cos\phi}, \tag{3.20}$$
$$\theta_\pm = \tan^{-1}\left(\frac{2\mathcal{A}_b\sin\phi}{\pm 2\mathcal{A}_b\cos\phi + \mathcal{A}_a}\right). \tag{3.21}$$

By using the renormalizations, the Fourier coefficients of the Hamiltonian H_n is explicitly given in the matrix form,

$$\hat{H}_n(\boldsymbol{k}) = \begin{pmatrix} \Delta\delta_{n,0} & A_{2,n}(\boldsymbol{k}) & B_{2,n}(\boldsymbol{k}) & B_{1,n}(\boldsymbol{k}) \\ A^*_{2,-n}(\boldsymbol{k}) & -\Delta\delta_{n,0} & B^*_{2,-n}(\boldsymbol{k}) & B^*_{1,-n}(\boldsymbol{k}) \\ B^*_{2,-n}(\boldsymbol{k}) & B_{2,n}(\boldsymbol{k}) & 0 & A_{1,n}(\boldsymbol{k}) \\ B^*_{1,-n}(\boldsymbol{k}) & B_{1,n}(\boldsymbol{k}) & A^*_{1,-n}(\boldsymbol{k}) & 0 \end{pmatrix} \tag{3.22}$$

with

$$A_{1,n}(\boldsymbol{k}) = \tilde{t}_{a1}\, e^{ik_y a/2} J_{-n}(\mathcal{A}_a/2) + t_{a1}\, e^{-ik_y a/2} J_n(\mathcal{A}_a/2), \tag{3.23}$$

$$A_{2,n}(\boldsymbol{k}) = t_{a2}\, e^{ik_y a/2} J_{-n}(\mathcal{A}_a/2) + t_{a3}\, e^{-ik_y a/2} J_n(\mathcal{A}_a/2), \tag{3.24}$$

$$B_{1,n}(\boldsymbol{k}) = t_{b1}\, e^{i(k_x b/2 + k_y a/4)} J_{-n}(\mathcal{A}_+) e^{-in\theta_+} + t_{b4}\, e^{-i(k_x b/2 - k_y a/4)} J_{-n}(\mathcal{A}_-) e^{+in\theta_-}, \tag{3.25}$$

$$B_{2,n}(\boldsymbol{k}) = t_{b2}\, e^{i(k_x b/2 - k_y a/4)} J_n(\mathcal{A}_-) e^{+in\theta_-} + t_{b3}\, e^{-i(k_x b/2 + k_y a/4)} J_n(\mathcal{A}_+) e^{-in\theta_+}. \tag{3.26}$$

In the case of $\phi = \pi/2$, we have

$$\mathcal{A}_+ = \mathcal{A}_- = \frac{1}{4}\sqrt{4\mathcal{A}_b^2 + \mathcal{A}_a^2} \equiv \mathcal{A}, \tag{3.27}$$

$$\theta_+ = \theta_- = \tan^{-1}\left(\frac{2\mathcal{A}_b}{\mathcal{A}_a}\right) \equiv \theta. \tag{3.28}$$

In this thesis, we adopt two different approaches to analyze the Floquet Hamiltonian. One approach is to directly solve the eigenequation in Eq. (2.76) by restricting the number of photon as $|m| \leq 8$ where the size of the Floquet Hamiltonian matrix $\mathcal{H}_{nm} (\equiv H_{n-m} - m\omega\delta_{n,m})$ in Eq. (2.77) is 68×68 because $\hat{H}_n$ is a 4×4 matrix. The other approach is to solve the eigenequation for H_{eff} in Eq. (2.98) by restricting the summation over n within $n \leq 8$. The former method provides finer and more precise calculation results in the low-frequency region of $\hbar\omega/t < 1$, while the latter method provides reasonable results when $\hbar\omega/t \gg 1$ because this method is based on the effective Hamiltonian obtained from the perturbation with respect to $t/\hbar\omega$. We also note that for smaller frequencies ω, a larger size $|m|$ of the Floquet matrix is required, typically of the order of $W/\hbar\omega$, where W is the bandwidth [85]. Since we adopt $|m| \leq 8$ for α-(BEDT-TTF)$_2$I$_3$ with $W \sim 0.8$ eV, the obtained results are reliable for $\hbar\omega \geq 0.1$ eV. Therefore we mainly discuss the results obtained by the former method unless otherwise noted.

3.2 Topological phase transition induced by circularly polarized light

In Sec. 3.1, we reviewed some features of α-(BEDT-TTF)$_2$I$_3$ and constructed the Floquet Hamiltonian for the material under irradiation with light. Now, we shift our focus to the photoinduced topological phase transition in α-(BEDT-TTF)$_2$I$_3$. We begin by discussing the photoinduced topological phase transition induced by circularly polarized light. We demonstrate that irradiation with circularly polarized light opens a gap at the Dirac points, ultimately leading to the system becoming a Chern insulator characterized by a quantized topological invariant. The content of this section has been published in Ref. [79, 81], and is also part of my master's thesis.

3.2.1 Band structure and Berry curvature

We discuss the photoinduced variation of band structures and their topological properties by analyzing the Floquet Hamiltonian obtained in the previous section. Here, we focus on the case where the charge order dissolves upon applying sufficient uniaxial pressure, and thus, we set $\Delta = 0$ in the following. Figure 3.3(a) displays the band dispersions for the third and fourth bands, $E_3(\boldsymbol{k})$ and $E_4(\boldsymbol{k})$, in the absence of photoirradiation. As mentioned earlier, these two bands make contact at two individual points in momentum space to form a pair of inclined Dirac cones, with the Dirac points situated at the Fermi level. Figure 3.3(b-d) depict plots of $E_3(\boldsymbol{k})$ and $E_4(\boldsymbol{k})$ for photoirradiated systems with various E^{ω} and ω of light. Once the system is irradiated with circularly polarized light, a gap opens at the Dirac points.

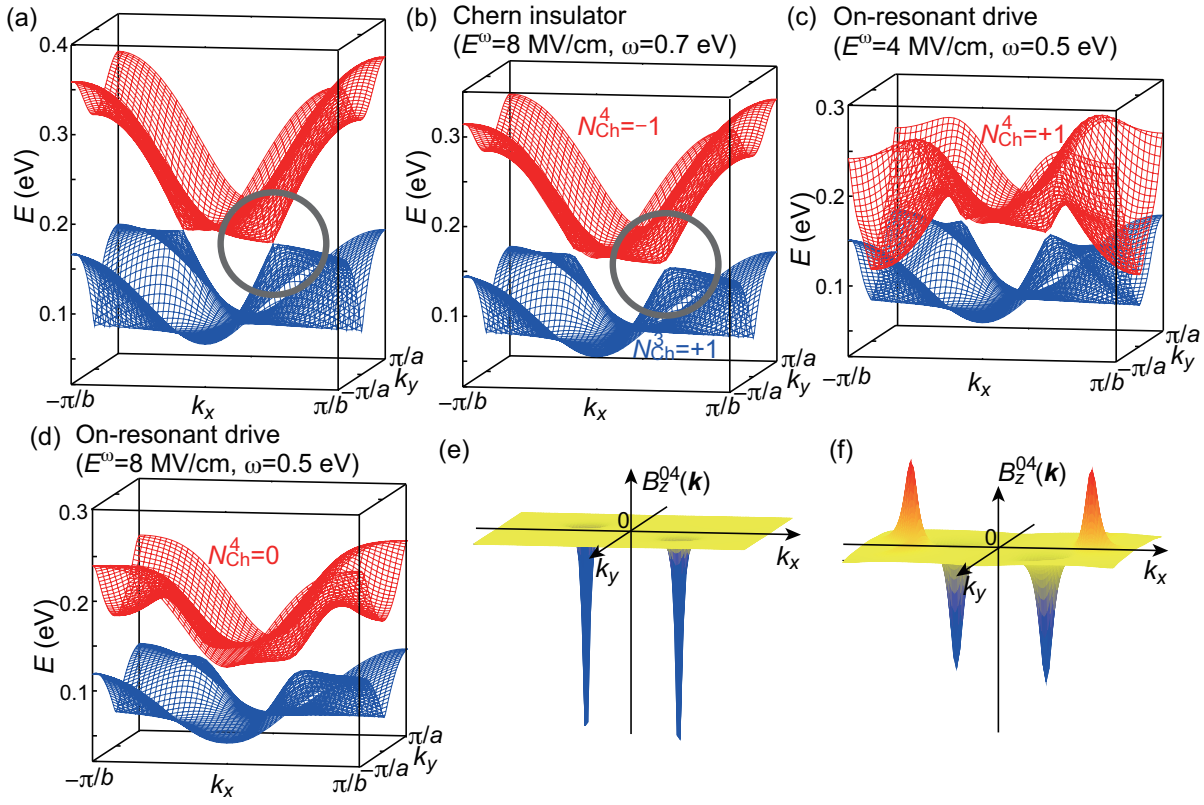

Figure 3.3. (a) Band dispersions of the third and fourth bands, $E_3(\boldsymbol{k})$ and $E_4(\boldsymbol{k})$, before light irradiation. (b-d) Those for the photoinduced phases under irradiation with circularly polarized light, i.e., (b) $N^4_{\mathrm{Ch}} \neq 0$ under off-resonant drive (Chern insulator phase), (c) $N^4_{\mathrm{Ch}} \neq 0$ under on-resonant drive, and (d) $N^4_{\mathrm{Ch}} = 0$ under on-resonant drive. (e, f) Berry curvatures of the fourth band $B^4_z(\boldsymbol{k})$ in momentum space for (e) the photoinduced Chern insulator phase with $N^4_{\mathrm{Ch}} = -1$ and (f) the photoinduced phase with $N^4_{\mathrm{Ch}} = 0$. Adapted from our previous study in Ref. [79].

To explore the topological character of α-(BEDT-TTF)$_2$I$_3$ irradiated with circularly polarized light, we calculate the Berry curvature and Chern number. The Chern number

of the νth band $N_{\rm Ch}^{\nu}$ (ν=1,2,3,4) is related to the Berry curvature $B_z^{\nu}(\boldsymbol{k})$,

$$N_{\rm Ch}^{\nu} = \frac{1}{2\pi}\int\int_{\rm BZ} B_z^{\nu}(\boldsymbol{k})dk_x dk_y, \tag{3.29}$$

where the Berry curvature $B_z^{\nu}(\boldsymbol{k})$ at each $\boldsymbol{k}$ point is given by

$$B_z^{\nu}(\boldsymbol{k}) = i\sum_{(m,\mu)} \frac{\langle\Phi_{\nu}^{n}(\boldsymbol{k})|\,\frac{\partial\hat{\mathcal{H}}}{\partial k_x}\,|\Phi_{\mu}^{m}(\boldsymbol{k})\rangle\,\langle\Phi_{\mu}^{m}(\boldsymbol{k})|\,\frac{\partial\hat{\mathcal{H}}}{\partial k_y}\,|\Phi_{\nu}^{n}(\boldsymbol{k})\rangle - c.c.}{[\varepsilon_{\mu}^{m}(\boldsymbol{k}) - \varepsilon_{\nu}^{n}(\boldsymbol{k})]^2}. \tag{3.30}$$

Here $\hat{\mathcal{H}}$ refers to the Floquet Hamiltonian matrix, whereas $\varepsilon_{\nu}^{n}(\boldsymbol{k})$ and $|\Phi_{\nu}^{n}(\boldsymbol{k})\rangle$ are, respectively, the eigenenergies and the corresponding eigenvectors of Eq. (2.76) with $\nu = 1, 2, 3, 4$ and $|m| \leq 8$. The summation is taken over m and μ where $(m, \mu) \neq (n, \nu)$; "*c.c.*" denotes the complex conjugate of the first term of the numerator. Note that B_z^{ν} is independent of the photon number n. In this thesis, the Chern numbers and Berry curvatures are calculated using a numerical technique proposed by Fukui *et al*. in Ref. [99].

The calculated Chern numbers of the bands in photodriven α-(BEDT-TTF)$_2$I$_3$ are presented in Figs. 3.3(b-d). The band structure in Fig. 3.3(b) depicts irradiation with light of a frequency larger than the bandwidth of α-(BEDT-TTF)$_2$I$_3$ (this situation is referred to as the off-resonant situation). Note that the bandwidth of α-(BEDT-TTF)$_2$I$_3$ shrinks due to renormalization characterized by the Bessel function $J_0(\mathcal{A})$ resulting from light irradiation. We observe a nonzero Chern number in the fourth band $N_{\rm Ch}^4$. When the electron filling is 3/4 with three fully occupied lower bands, the sum of the Chern numbers over the three bands below the Fermi level, $N_{\rm Ch} = \sum_{\nu=1}^{3} N_{\rm Ch}^{\nu}$, coincides with $-N_{\rm Ch}^4$, because conservation of invariance requires the sum of the Chern numbers over all four bands to be zero. Therefore, the band structure in Fig. 3.3(b), characterized by $N_{\rm Ch} = +1$, is assigned to the Chern insulator phase. It should be noted that the nonequilibrium distribution function can be approximated to the Fermi-Dirac distribution when the frequency of light is larger than the bandwidth of the system.

On the other hand, we find both zero and nonzero Chern numbers for the fourth band $N_{\rm Ch}^4$ when the frequency of light is smaller than the bandwidth of α-(BEDT-TTF)$_2$I$_3$ (this situation is referred to as the on-resonant situation). Figures 3.3(e) and (f) display the Berry curvature of the photoindced phases, corresponding to the band structures shown in Figs. 3.3(b) and (d), respectively. The Berry curvature in the Chern insulator phase has two negative peaks at the gapped Dirac points, corresponding to the nonzero quantized Chern number $-N_{\rm Ch}^4$ of -1. Meanwhile, the Berry curvature in Fig. 3.3(f) has additional positive peaks as well as two negative peaks around the gapped Dirac points that cancel the opposite contributions, resulting in $N_{\rm Ch}^4 = 0$. These additional peaks come from the band crossing between the one-photon dressed band and the original band, and thus this kind of phase only appears in on-resonant case. Note that the conductivity and transport properties in on-resonant systems should be calculated using the Floquet–Keldysh method [41, 100], which is formulated by combining the Keldysh Green's function technique [101, 102] and the Floquet theory. The photoinduced Hall conductivity in α-(BEDT-TTF)$_2$I$_3$ is extensively discussed in our previous papers [79, 80] and my master's thesis.

3.2.2 Chiral edge current

The Chern insulator is characterized by existence of chiral edge states as well as the Chern number N_{Ch}. Therefore, we next investigate the edge states for systems having edges to validate the predicted photoinduced topological phase transition. The band structures including those associated with the edge states are calculated for systems having edges by imposing the open boundary conditions in the x direction and the periodic boundary conditions in the y direction and vice versa. Here we display how to perform the calculations by taking a system having AA′ and BC edges, both of which are parallel to the y axis [Fig. 3.4]. The positions of unit cells are numbered in ascending order from the left most (i=1) to the right most ($i = N_x$) along the x axis, whereas from the bottom (j=1) to the top ($j = N_y$) along the y axis.

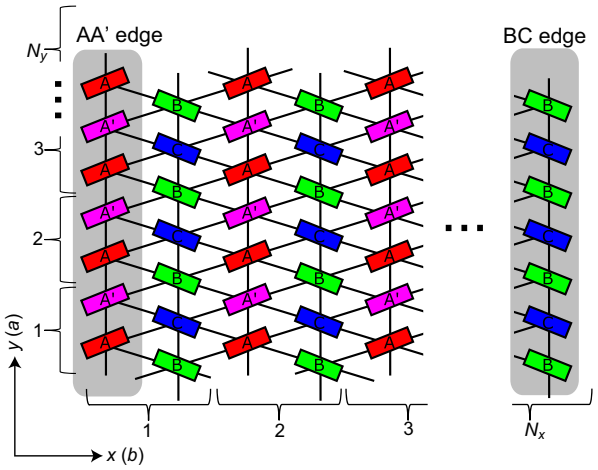

Figure 3.4. Monolayer nanoribbon-shaped system of α-(BEDT-TTF)$_2$I$_3$ having AA′ and BC edges parallel to the y (a) axis used for calculation of the band structures including those of the edge states. The open boundary conditions are imposed in the x direction while the periodic boundary conditions in the y direction. The numberings of the unit cells along the x and y axes are also presented. Adapted from our previous study in Ref. [80].

Since we impose the periodic boundary conditions in the y direction, we perform the Fourier transformation for the creation and annihilation operators with respect to the y coordinate,

$$c^{\dagger}_{ij\alpha} = \frac{1}{\sqrt{N_y}} \sum_{k_y} c^{\dagger}_{k_y i\alpha} e^{ik_y y_{j,\alpha}}, \tag{3.31}$$

where i and j are the integer coordinates of unit cells along the x and y axes (i.e., $1 \leq i \leq N_x$ and $1 \leq j \leq N_y$), respectively. The index α labels a molecule site among four in the unit cell. The coordinate $y_{i,\alpha}$ is the y coordinate of the αth molecule site in the (1,j)th unit cell. Then we can solve the eigenvalue problem for the nanoribbon-shaped

system shown in Fig. 3.4 using the basis $\left(c^\dagger_{k_y,A,1}, c^\dagger_{k_y,A',1}, \cdots, c^\dagger_{k_y,B,N_x}, c^\dagger_{k_y,C,N_x}\right)$ with

$$k_y = \frac{2\pi}{N_y a} n_y, \left(n_y = -\frac{N_y}{2} + 1, \cdots, \frac{N_y}{2}\right). \tag{3.32}$$

A tight-binding model for this system is given by,

$$H = \psi^\dagger_{k_y} H(k_y) \psi_{k_y}, \tag{3.33}$$

where

$$\psi^\dagger_{k_y} = \left(c^\dagger_{k_y,A,1}, c^\dagger_{k_y,A',1}, c^\dagger_{k_y,B,1}, c^\dagger_{k_y,C,1}, \cdots, c^\dagger_{k_y,A,N_x}, c^\dagger_{k_y,A',N_x}, c^\dagger_{k_y,B,N_x}, c^\dagger_{k_y,C,N_x}\right), \tag{3.34}$$

$$H(k_y) = \begin{pmatrix}
0 & H_{\mathrm{AA'}} & H_{\mathrm{AB}} & H_{\mathrm{AC}} & 0 & 0 & 0 & 0 & \cdots & 0 & 0 \\
H^*_{\mathrm{AA'}} & 0 & H_{\mathrm{A'B}} & H_{\mathrm{A'C}} & 0 & 0 & 0 & 0 & \cdots & 0 & 0 \\
H^*_{\mathrm{AB}} & H^*_{\mathrm{A'B}} & 0 & H_{\mathrm{BC}} & H_{\mathrm{BA}} & H_{\mathrm{BA'}} & 0 & 0 & \cdots & 0 & 0 \\
H^*_{\mathrm{AC}} & H^*_{\mathrm{A'C}} & H_{\mathrm{BC}} & 0 & H_{\mathrm{CA}} & H_{\mathrm{CA'}} & 0 & 0 & \cdots & 0 & 0 \\
0 & 0 & H^*_{\mathrm{BA}} & H^*_{\mathrm{CA}} & 0 & H_{\mathrm{AA'}} & H_{\mathrm{AB}} & H_{\mathrm{AC}} & \cdots & 0 & 0 \\
0 & 0 & H^*_{\mathrm{BA'}} & H^*_{\mathrm{CA'}} & H^*_{\mathrm{AA'}} & 0 & H_{\mathrm{A'B}} & H_{\mathrm{A'C}} & \cdots & 0 & 0 \\
0 & 0 & 0 & 0 & H^*_{\mathrm{AB}} & H^*_{\mathrm{A'B}} & 0 & H_{\mathrm{BC}} & \cdots & 0 & 0 \\
0 & 0 & 0 & 0 & H^*_{\mathrm{AC}} & H^*_{\mathrm{A'C}} & H_{\mathrm{BC}} & 0 & \cdots & 0 & 0 \\
\vdots & \vdots & \vdots & \vdots & \vdots & \vdots & \vdots & \vdots & \ddots & \vdots & \vdots \\
0 & 0 & 0 & 0 & 0 & 0 & 0 & 0 & \cdots & 0 & H_{\mathrm{BC}} \\
0 & 0 & 0 & 0 & 0 & 0 & 0 & 0 & \cdots & H_{\mathrm{BC}} & 0
\end{pmatrix}, \tag{3.35}$$

with

$$H_{\mathrm{BC}} = 2t_{a1} \cos\left(\frac{k_y}{2}\right) \equiv p_1 \tag{3.36}$$

$$H_{\mathrm{AA'}} = t_{a2} e^{ik_y/2} + t_{a3} e^{-ik_y/2} \equiv p_2 \tag{3.37}$$

$$H_{\mathrm{AC}} = H_{\mathrm{CA'}} = t_{b1} e^{ik_y/4} \equiv q_1 \tag{3.38}$$

$$H_{\mathrm{AB}} = H_{\mathrm{BA'}} = t_{b2} e^{-ik_y/4} \equiv q_2 \tag{3.39}$$

$$H_{\mathrm{A'B}} = H_{\mathrm{BA}} = t_{b3} e^{ik_y/4} \equiv q_3 \tag{3.40}$$

$$H_{\mathrm{A'C}} = H_{\mathrm{CA}} = t_{b4} e^{-ik_y/4} \equiv q_4 \tag{3.41}$$

The transfer integrals in this tight-binding model attain Peierls phase when the system is irradiated with circularly polarized light. Using the dimensionless vector potential amplitudes $\mathcal{A}_a$ and $\mathcal{A}_b$ in Eq. (3.8), the components of the time-dependent tight-binding

Hamiltonian are given by,

$$H_{\mathrm{BC}}(\tau) = 2t_{a1}\cos\left(\frac{k_y}{2} + \frac{\mathcal{A}_a}{2}\sin(\omega\tau)\right) \equiv p_1(\tau) \tag{3.42}$$

$$H_{\mathrm{AA'}}(\tau) = t_{a2}e^{ik_y/2}\exp\left(i\frac{\mathcal{A}_a}{2}\sin(\omega\tau)\right) + t_{a3}e^{-ik_y/2}\exp\left(-i\frac{\mathcal{A}_a}{2}\sin(\omega\tau)\right) \equiv p_2(\tau) \tag{3.43}$$

$$H_{\mathrm{AC}}(\tau) = H_{\mathrm{CA'}}(\tau) = t_{b1}e^{ik_y/4}\exp\left[i\left(\frac{\mathcal{A}_a}{4}\sin(\omega\tau) + \frac{\mathcal{A}_b}{2}\cos(\omega\tau)\right)\right] \equiv q_1(\tau) \tag{3.44}$$

$$H_{\mathrm{AB}}(\tau) = H_{\mathrm{BA'}}(\tau) = t_{b2}e^{-ik_y/4}\exp\left[-i\left(\frac{\mathcal{A}_a}{4}\sin(\omega\tau) - \frac{\mathcal{A}_b}{2}\cos(\omega\tau)\right)\right] \equiv q_2(\tau) \tag{3.45}$$

$$H_{\mathrm{A'B}}(\tau) = H_{\mathrm{BA}}(\tau) = t_{b3}e^{ik_y/4}\exp\left[i\left(\frac{\mathcal{A}_a}{4}\sin(\omega\tau) + \frac{\mathcal{A}_b}{2}\cos(\omega\tau)\right)\right] \equiv q_3(\tau) \tag{3.46}$$

$$H_{\mathrm{A'C}}(\tau) = H_{\mathrm{CA}}(\tau) = t_{b4}e^{-ik_y/4}\exp\left[-i\left(\frac{\mathcal{A}_a}{4}\sin(\omega\tau) - \frac{\mathcal{A}_b}{2}\cos(\omega\tau)\right)\right] \equiv q_4(\tau) \tag{3.47}$$

After the Fourier transformation with respect to time τ, we obtain the following Fourier components

$$p_{1,n} = t_{a1}\left[e^{ik_y/2}J_{-n}\left(\frac{\mathcal{A}_a}{2}\right) + e^{-ik_y/2}J_n\left(\frac{\mathcal{A}_a}{2}\right)\right] \tag{3.48}$$

$$p_{2,n} = t_{a2}e^{ik_y/2}J_{-n}\left(\frac{\mathcal{A}_a}{2}\right) + t_{a3}e^{-ik_y/2}J_n\left(\frac{\mathcal{A}_a}{2}\right) \tag{3.49}$$

$$q_{1,n} = t_{b1}e^{ik_y/4}J_{-n}(\mathcal{A})e^{-in\theta} \tag{3.50}$$

$$q_{2,n} = t_{b2}e^{-ik_y/4}J_n(\mathcal{A})e^{+in\theta} \tag{3.51}$$

$$q_{3,n} = t_{b3}e^{ik_y/4}J_{-n}(\mathcal{A})e^{-in\theta} \tag{3.52}$$

$$q_{4,n} = t_{b4}e^{-ik_y/4}J_n(\mathcal{A})e^{+in\theta}, \tag{3.53}$$

where the following relations hold,

$$(p_2^*)_{,n} = (p_{2,-n})^*, \tag{3.54}$$

$$(q_1^*)_{,n} = (q_{1,-n})^*, \tag{3.55}$$

$$(q_2^*)_{,n} = (q_{2,-n})^*, \tag{3.56}$$

$$(q_3^*)_{,n} = (q_{3,-n})^*, \tag{3.57}$$

$$(q_4^*)_{,n} = (q_{4,-n})^*. \tag{3.58}$$

By diagonalizing thus derived Floquet effective Hamiltonian, we obtain the band dispersion relations, which contain those of chiral edge states.

We examine several monolayer systems of α-(BEDT-TTF)$_2$I$_3$ with different edges. Figures 3.5(a) and (b) depict band structures before and during the light irradiation, respectively, for a system with vertical edges along the y axis, that is, the AA$'$ and BC edges at left and right ends of the sample [Fig. 3.4 and Fig. 3.5(e)]. As explained earlier, the open boundary conditions are imposed in the x direction, while the periodic boundary conditions are imposed in the y direction. It should be noted that we obtain the band

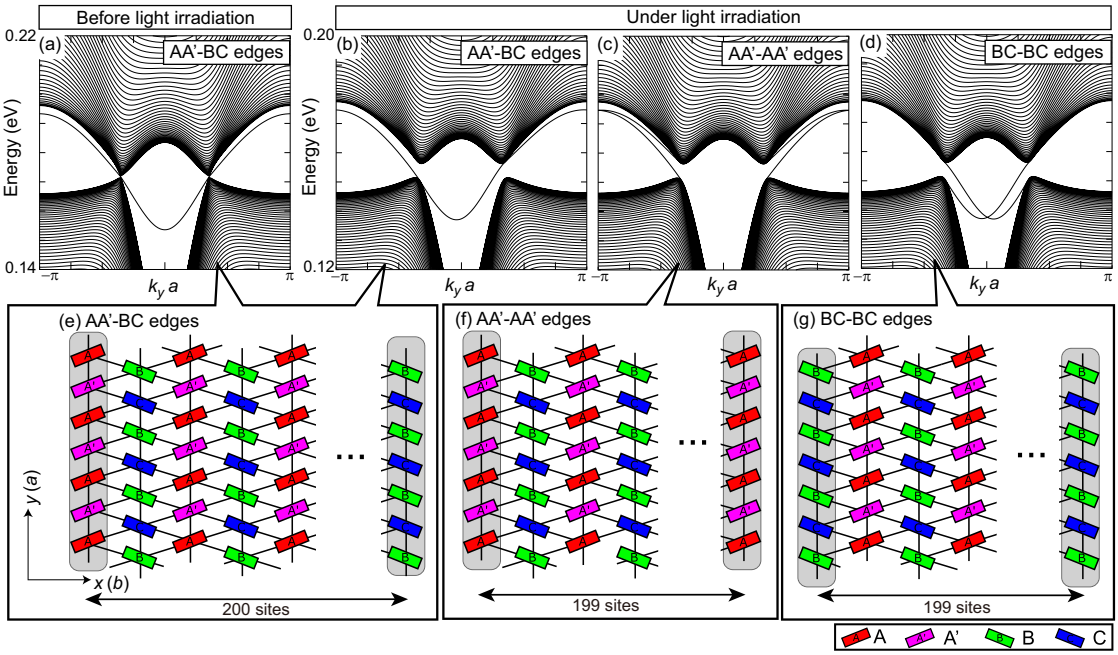

Figure 3.5. Band structures with chiral edge-state bands for systems with vertical edges on which the open boundary conditions are imposed in the x (b) direction. (a) Those for a steady system with AA$'$-BC edges in the absence of light irradiation. (b-d) Those for photodriven systems with (b) AA$'$-BC edges (c) AA$'$-BC edges, and (d) BC-BC edges where the periodic boundary conditions are imposed in the y (a) direction. (e-f) Systems with (e) AA$'$-BC edges, (f) AA$'$-AA$'$ edges, and (g) BC-BC edges used for the calculations. The amplitudes and frequency of light are set to be $E_a^\omega = 8$ MV/cm, $E_b^\omega = 8$ MV/cm, and $\hbar\omega = 0.7$ eV. Adapted from our previous study in Ref. [80].

dispersion relations including those associated with the edge states by diagonalizing the Floquet effective Hamiltonian. Here the amplitudes and frequency of the elliptically polarized light are chosen to be $E_a^\omega = 8$ MV/cm, $E_b^\omega = 8$ MV/cm, and $\hbar\omega = 0.7$ eV, respectively, where the Chern insulator is realized. The band structures in Figs. 3.5(a) and (b) show appearance of the bands associated with the edge states. The Dirac points are degenerate before light irradiation in Fig. 3.5(a), whereas they become gapped under light irradiation in Fig. 3.5(b). Importantly, the edge-state bands connect the lower valence band and the upper conduction band, which clearly evidences that the predicted photoinduced phase assigned to the Chern insulator phase is indeed topologically nontrivial. We also examine other systems with different vertical edges. Figure 3.5(c) displays the band dispersion relations for a system having two AA′ edges [Fig. 3.5(f)], whereas Fig. 3.5(d) depicts those for a system having two BC edges [Fig. 3.5(g)]. We again obtain the band structures associated with the chiral edge states connecting the upper and lower bands of the gapped Dirac cones.

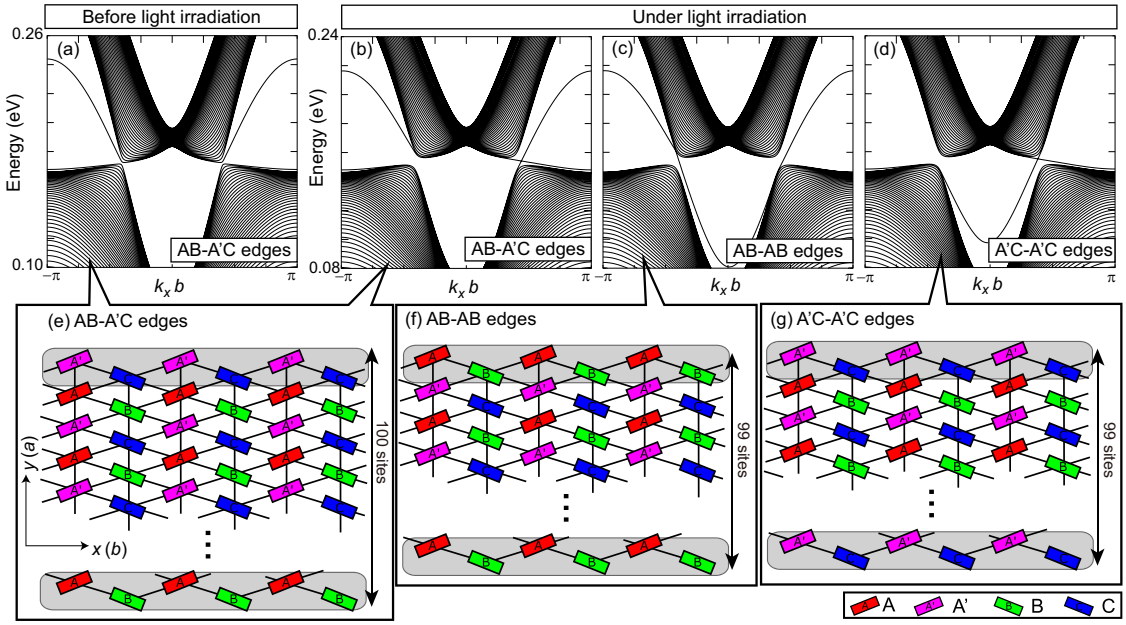

Figure 3.6. Band structures with chiral edge-state bands for systems with horizontal edges on which the open boundary conditions are imposed in the y (a) direction. (a) Those for a steady system with AB-A′C edges in the absence of light irradiation. (b-d) Those for photodriven systems with (b) AB-A′C edges (c) AB-AB edges, and (d) A′C-A′C edges where the periodic boundary conditions are imposed in the x (b) direction. (e-f) Systems with (e) AB-A′C edges, (f) AB-AB edges, and (g) A′C-A′C edges used for the calculations. The amplitudes and frequency of light are set to be $E_a^\omega = 8$ MV/cm, $E_b^\omega = 8$ MV/cm, and $\hbar\omega = 0.7$ eV. Adapted from our previous study in Ref. [80].

We also calculate the band dispersion relations for systems with horizontal edges [Figs. 3.6(a)-(d)]. Systems used for the calculations are depicted in Figs. 3.6(e)-(g). Specifically, we examine the systems with (e) AB-A′C edges, (f) AB-AB edges, and (g)

A′C-A′C edges at upper and bottom ends of the system. The open boundary conditions are imposed in the y direction, whereas the periodic boundary conditions are imposed in the x direction. The amplitudes and frequency of light are again chosen to be $E_a^\omega = 8$ MV/cm, $E_b^\omega = 8$ MV/cm, and $\hbar\omega = 0.7$ eV, respectively. The Dirac points are degenerate before the light irradiation [Fig. 3.6(a)], but the degeneracy is lifted by the photoinduced gap during the light irradiation [Figs. 3.6(b)-(d)]. Although the bands associated with the edge states depend on the edge species, they always connect the lower valence band and the upper conduction band separated by the photoinduced band gap at the Dirac points, again indicating that the corresponding photoinduced Chern insulator phase is indeed topologically nontrivial.

3.3 Pair annihilation of emergent magnetic charges induced by linearly polarized light

In the previous section, we demonstrated the photoinduced topological phase transition to the Chern insulator phase by focusing on the Chern numbers and the chiral edge states. Against the topological phase transition due to the breaking the time revearsal symmetry, we discuss the photoinduced band deformation induced by linearly polarized light in this section. Using the Floquet theory, we theoretically predict that a pair of slightly gapped Dirac-cone bands in a weakly charge-ordered α-(BEDT-TTF)$_2$I$_3$, which behave as magnetic charges with opposite signs in the momentum space, exhibit pair annihilation under irradiation with linearly polarized light. This photoinduced pair annihilation is accompanied by a nontopological phase transition to the Floquet normal insulator phase in contrast to the circularly polarized-light-induced topological phase transition to the Chern insulator phase. We stress that a charge-ordered state in α-(BEDT-TTF)$_2$I$_3$ providing a required staggered site potential and thereby provides a rare example of materials that can be used to observe the predicted pair annihilation phenomenon. The content of this section has been published in Ref. [81], and is also part of my master's thesis.

3.3.1 Band structure and Berry curvature

We first discuss quasienergy band structures of α-(BEDT-TTF)$_2$I$_3$ irradiated with linearly polarized light. The irradiated linearly polarized light generates a vector potential,

$$\boldsymbol{A}(\tau) = A\sin(\omega\tau)(\cos\theta, \sin\theta). \tag{3.59}$$

This vector potential corresponds to a linearly polarized light electric field whose polarized angle is θ,

$$\boldsymbol{E}(\tau) = -\frac{d\boldsymbol{A}(\tau)}{d\tau} = -A\omega\cos(\omega\tau)(\cos\theta, \sin\theta). \tag{3.60}$$

Therefore, we set $A_x = A\cos\theta$, $A_y = A\sin\theta$, and $\phi = 0$ to obtain the Floquet Hamiltonian matrix. Figures 3.7(a-d) show the band structures for various light amplitudes

obtained by the Floquet Hamiltonian. Here, the frequency and polarization angle of the linearly polarized light are chosen to be $\hbar\omega = 0.6$ eV and $\theta = 45°$, respectively. Additionally, as explained later, the site potential is fixed at $\Delta = 1 \times 10^{-5}$ eV for some reasons. Figure 3.7(a) displays the band structure before the light irradiation. On the other hand, Figs. 3.7(b-d) depict that the band structures during light irradiation have a photoinduced pair annihilation of the Dirac points. The distance between the two Dirac points shortens as the light amplitude E^{ω} increases, and these two Dirac points eventually merge and disappear at $E^{\omega} \sim 15$ MV/cm.

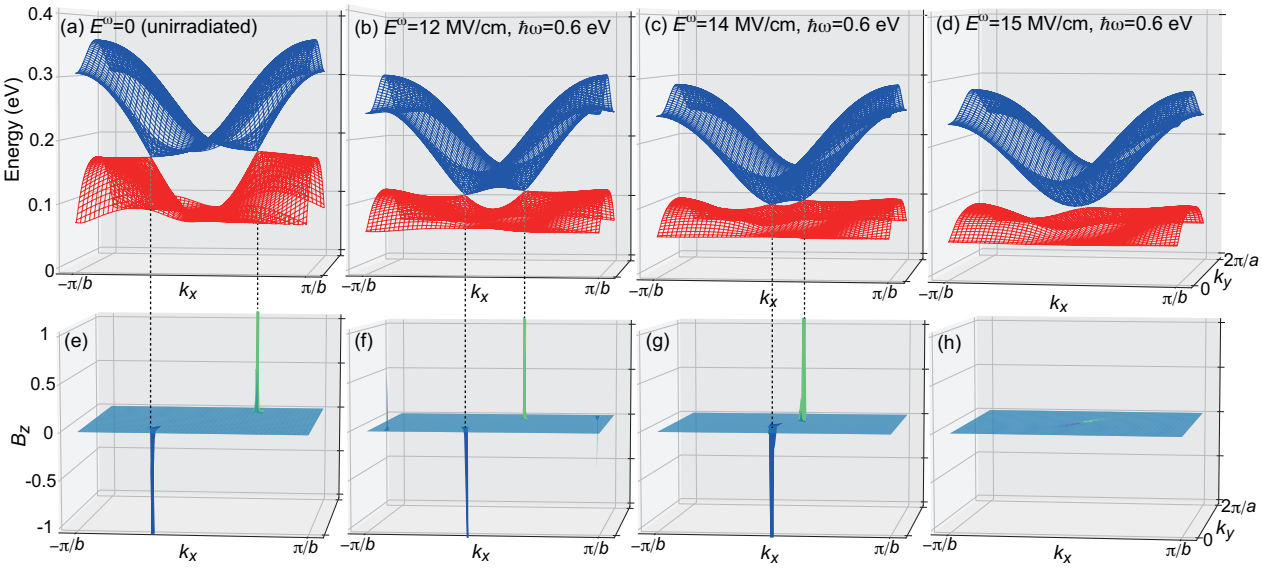

Figure 3.7. (a–d) Band structures of the photodriven α-(BEDT-TTF)$_2$I$_3$ under irradiation with linearly polarized light for various light amplitudes E^{ω}: (a) E^{ω}=0 (unirradiated case), (b) E^{ω}=12 MV/cm, (c) E^{ω}=14 MV/cm and (d) E^{ω}=15 MV/cm. (e–f) Berry curvature of the fourth band in the photodriven α-(BEDT-TTF)$_2$I$_3$. The sharp peaks with opposite signs indicate the existence of positive and negative magnetic charges at the momentum points corresponding to the gapped Dirac points. The frequency and the polarization angle of light are set to be $\hbar\omega = 0.6$ eV and $\theta = 45°$, respectively. Additionally, the site potential is fixed at $\Delta = 1 \times 10^{-5}$ eV. The pair annihilation of magnetic charges is realized with increasing E^{ω}. Adapted from our previous study in Ref. [81].

This phenomenon can be regarded as a pair annihilation of emergent magnetic charges with opposite signs. This pair annihilation in the momentum space is clearly visualized by the Berry curvature in the momentum space, which acts as an effective magnetic field by exerting an additional quantum phase (Berry phase) on itinerant electrons. For the massless Dirac-cone bands without a gap opening, the Berry curvature cannot be defined at the Dirac points. Here, the tiny gap at the Dirac points due to the staggered site potential of $\Delta = 1 \times 10^{-5}$ eV is assumed to avoid this problem. Figures 3.7(e-f) displays the calculated Berry curvatures $B_z^4(\boldsymbol{k})$ of the fourth band ($\nu = 4$) for various light amplitudes E^{ω}, which correspond to the band structures in Figs. 3.7(a-d), respectively.

Notice that the peaks of $B_z^\nu(\boldsymbol{k})$ at the two gapped Dirac points have opposite signs [79, 103, 96]. The positive peak corresponds to a positive magnetic charge (i.e., a source of the emergent magnetic field), whereas the negative peak corresponds to a negative magnetic charge (i.e., a sink of the emergent magnetic field). It should be noted that these magnetic charges can be regarded as magnetic fluxes rather than magnetic monopoles because they emerge in the two-dimensional momentum space. Therefore, the pair annihilation in this organic system can be interpreted as the pair annihilation of magnetic fluxes.

3.3.2 Phase diagram

This pair annihilation of emergent magnetic charges in the momentum space is accompanied by a nonequilibrium phase transition. To study the photoinduced phases in the present material, we define two types of energy gap defined as,

$$E_{\rm gap} = \min\left[\varepsilon_4^0(\boldsymbol{k})\right] - \max\left[\varepsilon_3^0(\boldsymbol{k})\right], \tag{3.61}$$

$$\tilde{E}_{\rm gap} = \min\left[\varepsilon_4^0(\boldsymbol{k}) - \varepsilon_3^0(\boldsymbol{k})\right]. \tag{3.62}$$

The gap $E_{\rm gap}$ is an indicator used to judge whether the system is insulating. That is to say, when $E_{\rm gap} > 0$, a gap opens at the Fermi level over the whole area of the Brillouin zone, and the system is thus insulator. In contrast, the system is semimetal when $E_{\rm gap} < 0$. Meanwhile, $\tilde{E}_{\rm gap}$ is an indicator used to judge whether the Dirac cones are gapped. In other words, the Dirac cones are gapped at the Dirac points when $E_{\rm gap} > 0$, whereas they are not gapped when $E_{\rm gap} > 0$. Note that $E_{\rm gap}$ cannot be negative by definition.

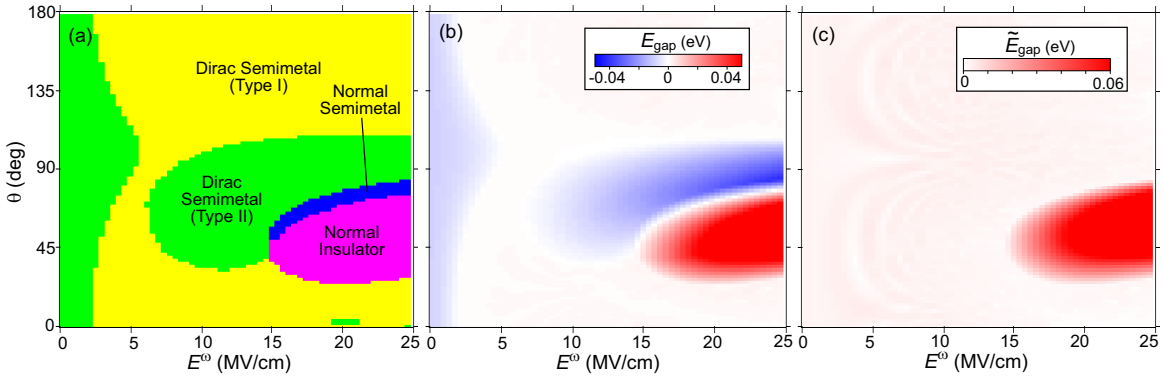

Figure 3.8. (a) Phase diagram for nonequilibrium steady states in the photo-driven α-(BEDT-TTF)$_2$I$_3$ irradiated with linearly polarized light, in the plane of the amplitude E^ω and the polarization angle θ of the light. (b,c) Color maps of the calculated two types of energy gap, (b) $E_{\rm gap}$ and (c) $\tilde{E}_{\rm gap}$, defined in Eqs. (3.61) and (3.62), respectively. The light frequency ω is set to be $\hbar\omega = 0.6$ eV. Adapted from our previous study in Ref. [81].

Figure 3.8(a) displays the phase diagram for nonequilibrium steady states in α-(BEDT-TTF)$_2$I$_3$ irradiated with linearly polarized light in the plane of the amplitude E^ω and the polarization angle θ of light. Here, the light frequency ω is chosen to be $\hbar\omega = 0.6$ eV. This phase diagram contains a variety of nonequilibrium steady phases

such as the type-I Dirac semimetal, type-II Dirac semimetal, normal semimetal, and normal insulator phases. Here, we distinguish between two types of Dirac semimetal phases: one is the Dirac semimetal with a point-like Fermi surface (type-I semimetal), and the other is a Dirac semimetal whose Fermi surface contains electron and hole pockets (type-II semimetal). These phases are classified according to the signs of the calculated energy gaps $E_{\rm gap}$ [Fig 3.8(b)] and $\tilde{E}_{\rm gap}$ [Fig. 3.8(c)] (see Table. 3.1). Notice that we did not consider the staggered site potential in obtaining the phase diagram.

	$\tilde{E}_{\rm gap}=0$	$\tilde{E}_{\rm gap}>0$
$E_{\rm gap}>0$	Type I Dirac semimetal	Normal insulator
$E_{\rm gap}\leq 0$	Type II Dirac semimetal	Normal semimetal

Table 3.1: Classification of the photoinduced phases in α-(BEDT-TTF)$_2$I$_3$ under irradiation with linearly polarized light according to the band gaps $E_{\rm gap}$ and $\tilde{E}_{\rm gap}$ defined by Eqs. (3.61) and (3.62).

It should be noted that there are two possible types of band structure for $E_{\rm gap}<0$ and $\tilde{E}_{\rm gap}=0$. Figure 3.9(a) depicts the band structure in which the upper band crosses the Fermi level at momenta far from the Dirac cones. On the other hand, Fig. 3.9(b) displays the band structure with overtilted Dirac cones where the upper (lower) cone band is located below (above) the Fermi level. In this thesis, we do not distinguish these phases in the phase diagram. In addition, note that the system is in the on-resonant situation when the amplitude of light is approximately less than 5 MV/cm in Fig. 3.8(a). Therefore, as explained earlier, the transport phenomena in low amplitude region should be considered using Floquet-Keldysh formalism. On the other hand, when the amplitude of light is larger and the bands in photodriven α-(BEDT-TTF)$_2$I$_3$ is enough shrinked due to the renormalization of the transfer integrals, the system becomes in the off-resonant situation. Therefore, the photoinduced pair annihilation of emergent magnetic charges occurs in the off-resonant situation.

As shown in Fig. 3.8, the phase transition from the Dirac semimetal phase to the normal insulator phase occurs at $E^{\omega}\sim 15$ MV/cm, which indicates that the observed pair annihilation of magnetic charges is accompanied by this photoinduced phase transition. Importantly, this phase transition is not topological but topologically trivial. In the case of the irradiation with circularly polarized light, the light breaks the time-reversal symmetry, and the second term of the Floquet effective Hamiltonian in Eq. (2.98) thus becomes finite ($\sum_{n=1}^{\infty}[H_{-n},H_n]/n\hbar\omega\neq 0$). Indeed, this term opens a gap at the Dirac points, and the Floquet Chern insulator phase eventually appears as bands separated by the gap attain nonzero Chern numbers. On the other hand, the Chern insulator phase never appears in the present case because the linearly polarized light does not break the time reversal symmetry. When the system is time-reversal invariant, the second term of the Floquet effective Hamiltonian vanishes ($\sum_{n=1}^{\infty}[H_{-n},H_n]/n\hbar\omega=0$) because the Hamiltonian is required to be invariant upon the replacement of ω with $-\omega$. As a result, the Hamiltonian reduces to $H_{\rm eff}=H_0+\mathcal{O}(1/\omega^2)$. However, the photoinduced gap opening occurs in this case due to the photoinduced renormalization of the transfer integrals.

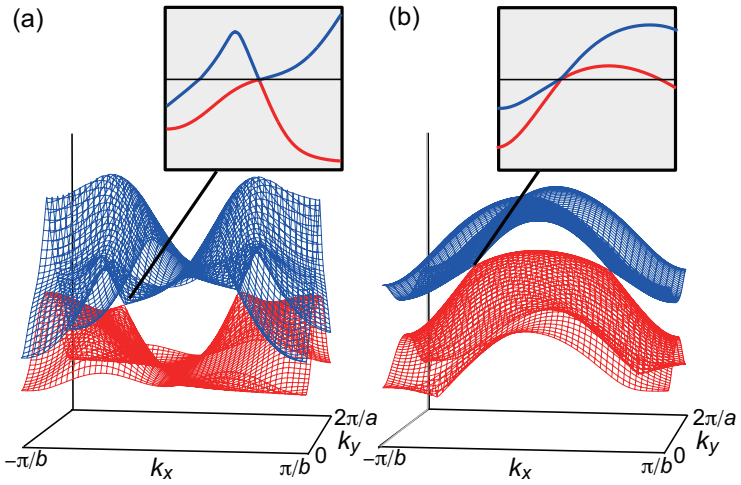

Figure 3.9. Two possible types of band structure for $E_{\rm gap} < 0$ and $\tilde{E}_{\rm gap} = 0$. (a) Band structure in which the upper band crosses the Fermi level at momenta far from the Dirac cones. (b) Band structure with overtilted Dirac cones where the upper (lower) cone band is located below (above) the Fermi level. Both cases are assigned to the type-II Dirac semimetal phase in the phase diagram in Fig. 3.8(a). Adapted from our previous study in Ref. [81].

More specifically, according to Eq. (2.98), the transfer integrals in the expression for H_0 are renormalized as

$$t_{i\alpha,j\beta} \;\rightarrow\; t_{i\alpha,j\beta} J_0(A_{i\alpha,j\beta}). \tag{3.63}$$

The normal insulator phase appears when the gap is opened by the resulting photoinduced band deformation.

Bond direction	Photoinduced renormalization of transfer integral	Renormalization factor
[010]	$t_{a1} \rightarrow t_{a1} J_0(\mathcal{A}_a/2)$ $t_{a2} \rightarrow t_{a2} J_0(\mathcal{A}_a/2)$ $t_{a3} \rightarrow t_{a3} J_0(\mathcal{A}_a/2)$	$J_0(\mathcal{A}_a/2)$
[110]	$t_{b1} \rightarrow t_{b1} J_0(\mathcal{A}_+)$ $t_{b3} \rightarrow t_{b3} J_0(\mathcal{A}_+)$	$J_0(\mathcal{A}_+)$
[1$\bar{1}$0]	$t_{b2} \rightarrow t_{b2} J_0(\mathcal{A}_-)$ $t_{b4} \rightarrow t_{b4} J_0(\mathcal{A}_-)$	$J_0(\mathcal{A}_-)$

Table 3.2: Photoinduced renormalizations of the transfer integrals in α-(BEDT-TTF)$_2$I$_3$ under irradiation with linearly polarized light.

In the phase diagram of Fig. 3.8(a), the normal insulator phase is observed only when the polarization angle θ is approximately 45°. This indicates that only linearly polarized light with a polarization angle of $\theta \sim 45°$ gives rise to the pair annihilation of emergent

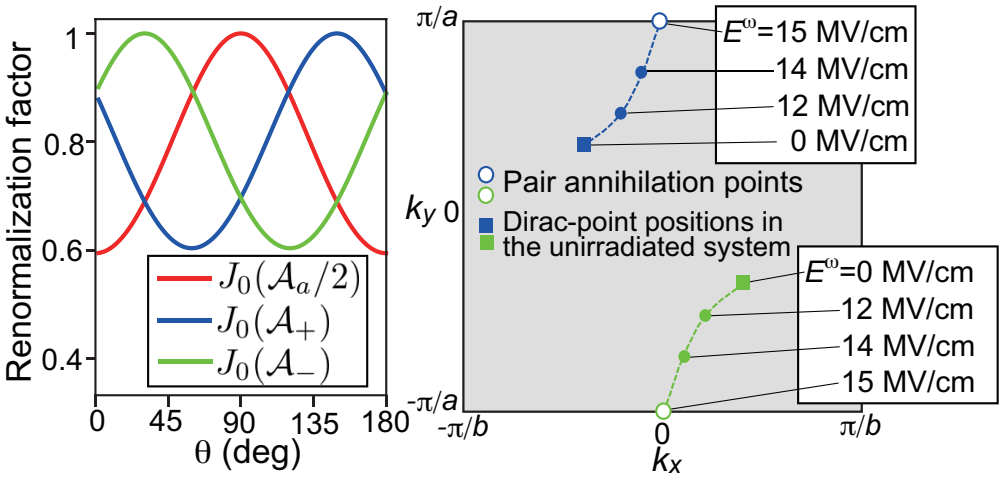

Figure 3.10. (a) Photoinduced renormalization factors $J_0(\mathcal{A}_a/2)$, $J_0(\mathcal{A}_+)$ and $J_0(\mathcal{A}_-)$ for the transfer integrals in α-(BEDT-TTF)$_2$I$_3$ under irradiation with linearly polarized light as functions of the light polarization angle θ. The light amplitude and frequency are set to be E^ω=15 MV/cm and $\hbar\omega$=0.6 eV, respectively. (b) Trajectories of the positive and negative emergent magnetic charges at the Dirac points with increasing light amplitude E^ω in the momentum space. Adapted from our previous study in Ref. [81].

magnetic charges. This sensitivity to the polarization angle θ might be attributed to the anisotropic renormalizations of the transfer integrals. Under the irradiation of light, the transfer integrals are renormalized by factors represented by the Bessel functions as shown in Eq. (3.63). More specifically, the transfer integrals for bonds along [010], [110] and [1$\bar{1}$0] directions are renormalized by factors $J_0(\mathcal{A}_a/2)$, $J_0(\mathcal{A}_+)$ and $J_0(\mathcal{A}_-)$, respectively (see Table. 3.2). Since $\mathcal{A}_a$, $\mathcal{A}_+$ and $\mathcal{A}_-$ are functions of θ as shown in Eqs. (3.72) and (3.77), the extent of the renormalization significantly depends on the angle θ. In Fig. 3.10(a), we plot the three renormalization factors $J_0(\mathcal{A}_a/2)$, $J_0(\mathcal{A}_+)$ and $J_0(\mathcal{A}_-)$ as functions of θ. We find that $J_0(\mathcal{A}_+)$ takes a minimum at $\theta \sim 45°$, which means that the transfer integrals for bonds along the [110] direction are strongly suppressed at $\theta \sim 45°$. This anisotropic renormalization of the transfer integrals is expected to modulate the band dispersions along the [110] direction in the momentum space, which displaces the Dirac points along this direction and the resulting collision and pair annihilation of the emergent magnetic charges with opposite signs. To confirm this, we display the positions of the two emergent magnetic charges in Fig. 3.10(b). As the light amplitude E^ω increases from 0 to 15 MV/cm, the positions of the positive and negative magnetic charges move toward (k_x, k_y)=$(0, \pi)$ and $(0, -\pi)$, respectively. Notably, they move approximately along the [110] direction in the momentum space, which supports the idea that the pair annihilation results from the anisotropic renormalizations of transfer integrals.

It should be noted that the pair annihilation of Dirac points cannot be observed in a honeycomb lattice irradiated with light. This is because the renormalizations of the transfer integrals do not depends on the bond direction in this case. Recently, the movement and merging of the Dirac points have been observed both theoretically [104]

and experimentally [105], but these studies manipulate the transfer integrals one by one. Therefore, the photoinduced pair annihilation of magnetic charges is a novel phenomenon that can occur only in low symmetry materials.

3.4 Novel type of photoinduced topological phase transition induced by elliptically polarized light

In the previous section, we illustrated that the pair annihilation of the emergent magnetic charges with opposite signs can be realized in α-(BEDT-TTF)$_2$I$_3$ irradiated with linearly polarized light. We stressed that this phenomenon occurs due to the anisotropic renormalization of the transfer integrals. In this section, we theoretically predict that irradiation with elliptically polarized light with a specific elliptical-axis angle [Fig. 3.11] causes collision of the Dirac points and resulting their collapse through dynamical band deformation, which result in the topological phase transition from a semimetal with gapped Dirac cones (topological) to a normal insulator (nontopological). This novel type of topological phase transition is distinct from the photoinduced topological phase transition induced by ciruclarly polarized light shown in Sec. 3.2. We also elucidate a rich nonequilibrium phase diagram in plane of the amplitude and elliptical-axis angle of light that contains four phases: topological semimetal phase, Chern insulator phase, normal semimetal phase, and normal insulator phase [Fig. 3.12]. In addition, we propose that the Hall conductivity can be a promising probe of the predicted unique photoinduced phase transition. The content of this chapter has been published in Ref. [82]. Note that the calculation results of band structure and Berry curvature (Sec. 3.4.2) is part of my master's thesis.

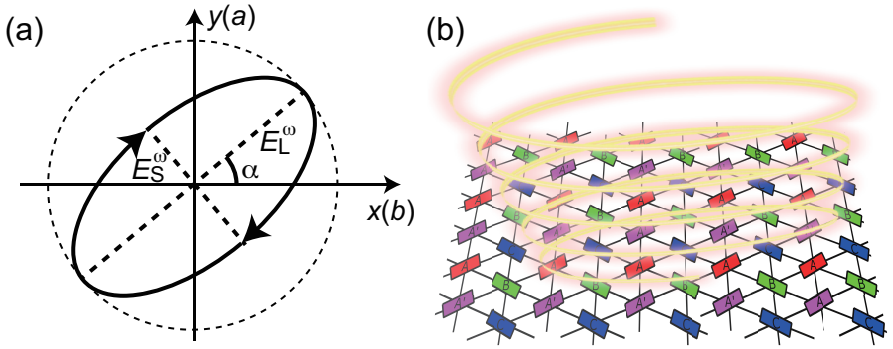

Figure 3.11. (a) Elliptically polarized light applied to the BEDT-TTF layer, which is characterized by the short-axis and long-axis amplitudes (E_S^ω, E_L^ω), the polarization angle α, and the frequency $\hbar\omega$. (b) Schematic of photodriven α-(BEDT-TTF)$_2$I$_3$ irradiated with elliptically polarized light. [80, 82]

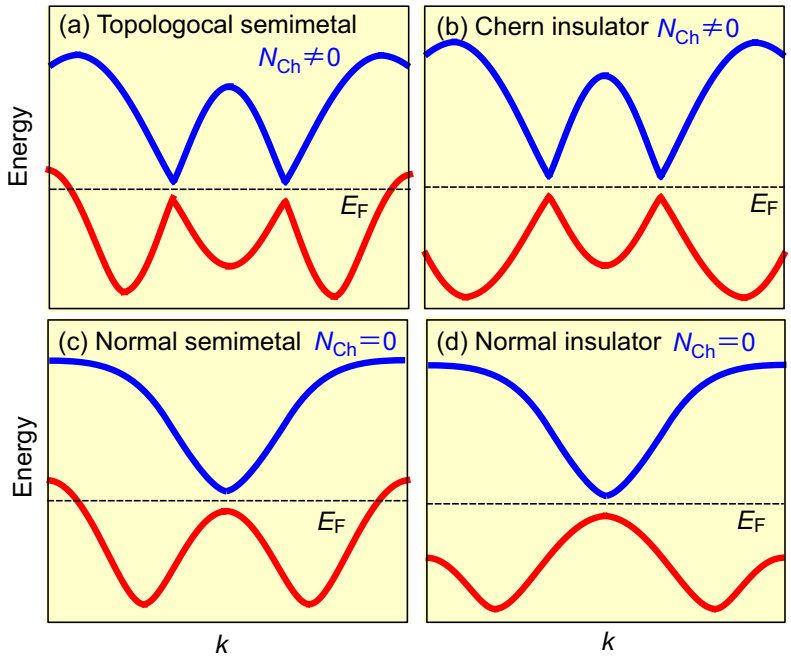

Figure 3.12. Schematic band structures of various photoinduced phases discussed in this section, i.e., (a) topological semimetal with gapped Dirac cones, (b) Chern insulator, (c) normal semimetal, and (d) normal insulator. The former two are topological phases which is characterized by nonzero Chern numbers, while the latter two are nontopological phases. Adapted from our previous study in Ref. [82].

3.4.1 Model

In this section, we consider the situation that α-(BEDT-TTF)$_2$I$_3$ is irradiated with elliptically polarized light, whose vector potential is given by,

$$\boldsymbol{A}(\tau) = \begin{pmatrix} \cos\alpha & -\sin\alpha \\ \sin\alpha & \cos\alpha \end{pmatrix} \begin{pmatrix} A_{\rm L}\cos(\omega\tau) \\ A_{\rm S}\sin(\omega\tau) \end{pmatrix}. \tag{3.64}$$

Here ω is the frequency of light. This vector potential produces a time-dependent electric field,

$$\begin{aligned} \boldsymbol{E}(\tau) &= -\frac{d\boldsymbol{A}(\tau)}{d\tau} \\ &= \begin{pmatrix} \cos\alpha & -\sin\alpha \\ \sin\alpha & \cos\alpha \end{pmatrix} \begin{pmatrix} -E^{\omega}_{\rm L}\sin(\omega\tau) \\ E^{\omega}_{\rm S}\cos(\omega\tau) \end{pmatrix}, \end{aligned} \tag{3.65}$$

where the amplitude of light is defined as $E^{\omega}_{\gamma} = A_{\gamma}\omega$ ($\gamma = {\rm S}, {\rm L}$). Equation (3.65) describes elliptically polarized light in Fig. 3.11(a), which is characterized by the long-axis amplitude $E^{\omega}_{\rm L}$, the short-axis amplitude $E^{\omega}_{\rm S}$, the elliptical-axis angle α, and the frequency $\hbar\omega$. It should be noted that we introduce the elliptical-axis angle to investigate the collapse and collision of Dirac points in this section, which is distinct from the elliptically polarized light considered in Sec. 3.1.2. The formalism in Sec. 3.1.2 corresponds to the case of $\alpha = 0$.

The Fourier coefficients of the tight-binding model with the Peierls phases that corresponds to the vector potential in Eq. (3.65) are calculated as,

$$H_n = \sum_{\langle i,j\rangle}\sum_{\alpha,\beta} t_{i\alpha,j\beta} J_n(A_{i\alpha,j\beta}) e^{-in\theta_{i\alpha,j\beta}} c^{\dagger}_{i,\alpha} c_{j,\beta} \tag{3.66}$$

where J_n is the nth Bessel function. Here, $A_{i\alpha,j\beta}$ and $\theta_{i\alpha,j\beta}$ are respectively defined as

$$\begin{aligned} A_{i\alpha,j\beta} &= \frac{e}{\hbar}\Big[\{bA_{\rm L}(\tilde{x}_{i\alpha} - \tilde{x}_{j\beta})\cos\alpha + aA_{\rm L}(\tilde{y}_{i\alpha} - \tilde{y}_{j\beta})\sin\alpha\}^2 \\ &\quad + \{-bA_{\rm S}(\tilde{x}_{i\alpha} - \tilde{x}_{j\beta})\sin\alpha + aA_{\rm S}(\tilde{y}_{i\alpha} - \tilde{y}_{j\beta})\cos\alpha\}^2\Big]^{1/2} \\ &= \big[\{\mathcal{A}_b(\tilde{x}_{i\alpha} - \tilde{x}_{j\beta}) + \mathcal{A}_a(\tilde{y}_{i\alpha} - \tilde{y}_{j\beta})\}^2 \\ &\quad + \{-\mathcal{A}_d(\tilde{x}_{i\alpha} - \tilde{x}_{j\beta}) + \mathcal{A}_c(\tilde{y}_{i\alpha} - \tilde{y}_{j\beta})\}^2\big]^{1/2}, \end{aligned} \tag{3.67}$$

$$\begin{aligned} \theta_{i\alpha,j\beta} &= \tan^{-1}\left[\frac{bA_{\rm L}(\tilde{x}_{i\alpha} - \tilde{x}_{j\beta})\cos\alpha + aA_{\rm L}(\tilde{y}_{i\alpha} - \tilde{y}_{j\beta})\sin\alpha}{-bA_{\rm S}(\tilde{x}_{i\alpha} - \tilde{x}_{j\beta})\sin\alpha + aA_{\rm S}(\tilde{y}_{i\alpha} - \tilde{y}_{j\beta})\cos\alpha}\right] \\ &= \tan^{-1}\left[\frac{\mathcal{A}_b(\tilde{x}_{i\alpha} - \tilde{x}_{j\beta}) + \mathcal{A}_a(\tilde{y}_{i\alpha} - \tilde{y}_{j\beta})}{-\mathcal{A}_d(\tilde{x}_{i\alpha} - \tilde{x}_{j\beta}) + \mathcal{A}_c(\tilde{y}_{i\alpha} - \tilde{y}_{j\beta})}\right], \end{aligned} \tag{3.68}$$

with

$$\mathcal{A}_a = \frac{eaA_{\rm L}\sin\alpha}{\hbar} \tag{3.69}$$

$$\mathcal{A}_b = \frac{ebA_{\rm L}\cos\alpha}{\hbar} \tag{3.70}$$

$$\mathcal{A}_c = \frac{eaA_{\rm S}\cos\alpha}{\hbar} \tag{3.71}$$

$$\mathcal{A}_d = \frac{ebA_{\rm S}\sin\alpha}{\hbar}. \tag{3.72}$$

After performing the Fourier transformations with respect to the spatial coordinates, we obtain,

$$\hat{H}_n(\boldsymbol{k}) = \begin{pmatrix} 0 & A_{2,n}(\boldsymbol{k}) & B_{2,n}(\boldsymbol{k}) & B_{1,n}(\boldsymbol{k}) \\ A^*_{2,-n}(\boldsymbol{k}) & 0 & B^*_{2,-n}(\boldsymbol{k}) & B^*_{1,-n}(\boldsymbol{k}) \\ B^*_{2,-n}(\boldsymbol{k}) & B_{2,n}(\boldsymbol{k}) & 0 & A_{1,n}(\boldsymbol{k}) \\ B^*_{1,-n}(\boldsymbol{k}) & B_{1,n}(\boldsymbol{k}) & A_{1,n}(\boldsymbol{k}) & 0 \end{pmatrix}, \tag{3.73}$$

where

$$\begin{aligned}
A_{1,n}(\boldsymbol{k}) &= t_{a1}\ \exp\left[i\frac{k_y}{2}\right] J_{-n}(\sqrt{\mathcal{A}_a^2+\mathcal{A}_c^2}/2)e^{-in\theta} \\
&\quad + t_{a1}\ \exp\left[-i\frac{k_y}{2}\right] J_n(\sqrt{\mathcal{A}_a^2+\mathcal{A}_c^2}/2)e^{-in\theta}, \\
A_{2,n}(\boldsymbol{k}) &= t_{a2}\ \exp\left[i\frac{k_y}{2}\right] J_{-n}(\sqrt{\mathcal{A}_a^2+\mathcal{A}_c^2}/2)e^{-in\theta} \\
&\quad + t_{a3}\ \exp\left[-i\frac{k_y}{2}\right] J_n(\sqrt{\mathcal{A}_a^2+\mathcal{A}_c^2}/2)e^{-in\theta}, \\
B_{1,n}(\boldsymbol{k}) &= t_{b1}\ \exp\left[i\Big(\frac{k_x}{2}+\frac{k_y}{4}\Big)\right] J_{-n}\left(\sqrt{\mathcal{A}_{\mathrm{L}+}^2+\mathcal{A}_{\mathrm{S}-}^2}\right) e^{-in\theta_2} \\
&\quad + t_{b4}\ \exp\left[-i\Big(\frac{k_x}{2}-\frac{k_y}{4}\Big)\right] J_{-n}\left(\sqrt{\mathcal{A}_{\mathrm{L}+}^2+\mathcal{A}_{\mathrm{S}-}^2}\right) e^{-in\theta_2}, \\
B_{2,n}(\boldsymbol{k}) &= t_{b2}\ \exp\left[i\Big(\frac{k_x}{2}-\frac{k_y}{4}\Big)\right] J_{n}\left(\sqrt{\mathcal{A}_{\mathrm{L}-}^2+\mathcal{A}_{\mathrm{S}+}^2}\right) e^{-in\theta_3} \\
&\quad + t_{b3}\ \exp\left[-i\Big(\frac{k_x}{2}+\frac{k_y}{4}\Big)\right] J_{n}\left(\sqrt{\mathcal{A}_{\mathrm{L}-}^2+\mathcal{A}_{\mathrm{S}+}^2}\right) e^{-in\theta_3},
\end{aligned}$$

with

$$\mathcal{A}_{\mathrm{L}\pm} = \frac{eA_\ell}{4\hbar}(\pm 2b\cos\alpha + a\sin\alpha), \tag{3.74}$$

$$\mathcal{A}_{\mathrm{S}\pm} = \frac{eA_{\mathrm{S}}}{4\hbar}(\pm 2b\cos\alpha + a\sin\alpha), \tag{3.75}$$

$$\theta = \tan^{-1}\left(\frac{A_{\mathrm{L}}\sin\alpha}{A_{\mathrm{S}}\cos\alpha}\right), \tag{3.76}$$

$$\theta_\pm = \tan^{-1}\left[\frac{A_{\mathrm{L}}(\pm 2b\cos\alpha + a\sin\alpha)}{A_{\mathrm{S}}(\mp 2b\cos\alpha + a\sin\alpha)}\right]. \tag{3.77}$$

We utilize Eq. (3.73) for H_n, H_{-n} and H_{n-m} in Eqs. (2.77) and (2.98).

3.4.2 Band structure and Berry curvature

We first discuss the photoinduced collision and collapse of two gapped Dirac points and resulting novel topological phase transition in α-(BEDT-TTF)$_2$I$_3$. Figures 3.13(a-d) depict quasienergy band structures under irradiation with elliptically polarized light for

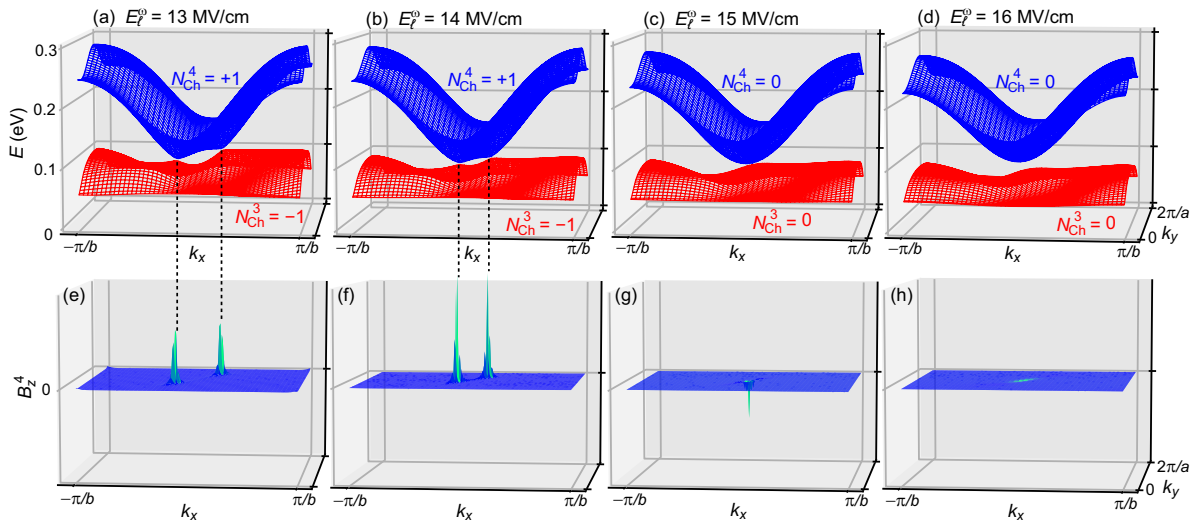

Figure 3.13. (a-d) Band structures in α-(BEDT-TTF)$_2$I$_3$ under irradiation with elliptically polarized light for different long-axis amplitudes E_{L}^{ω} of light, i.e., (a) $E_{\mathrm{L}}^{\omega} = 13$ MV/cm, (b) $E_{\mathrm{L}}^{\omega} = 14$ MV/cm, (c) $E_{\mathrm{L}}^{\omega} = 15$ MV/cm, and (d) $E_{\mathrm{L}}^{\omega} = 16$ MV/cm. (e-h) Berry curvatures for the fourth band in respective band structures. When a weak light field is applied, a pair of gapped Dirac points with positive Berry-curvature peaks appear, indicating the emergence of photoinduced topological phase. The distance between the two Dirac points becomes closer as E_{L}^{ω} increases, and they eventually collide to annihilate when $E_{\mathrm{L}}^{\omega} \sim 15$ MV/cm. At $E_{\mathrm{L}}^{\omega} = 16$ MV/cm, a gapped band structure with zero Berry curvature appears, indicating the occurence of photinduced phase tranition to a nontopological insulator phase. The frequency, polarization angle, and short-axis amplitude of elliptically polarized light are set to be $\hbar\omega = 0.6$ eV, $\alpha = 45°$, and $E_{\mathrm{S}}^{\omega} = 2$ MV/cm, respectively. Adapted from our previous study in Ref. [82].

different long-axis amplitudes $E_{\rm L}^{\omega}$ of light, namely, (a) $E_{\rm L}^{\omega} = 13$ MV/cm, (b) $E_{\rm L}^{\omega} = 14$ MV/cm, (c) $E_{\rm L}^{\omega} = 15$ MV/cm, and (d) $E_{\rm L}^{\omega} = 16$ MV/cm, where the other parameters of the light are chosen as $\hbar\omega = 0.6$ eV, $\alpha = 45°$, and $E_{\rm S}^{\omega} = 2$ MV/cm. These results are obtained by diagonalizing the Floquet Hamiltonian in Eq. (2.77). In Figs. 3.13(e-h), the Berry curvatures of the fourth band for corresponding quasienergy band structures are displayed.

Since elliptically polarized light breaks the time-reversal symmetry, it opens a topological gap at the two Dirac points that are initially gapless, and brings about a phase transition to a topologically nontrivial phase. As presented in Figs. 3.13(a) and (b), the quasienergy bands of this topological phase cross the Fermi level at certain momentum points distinct from those of the gapped Dirac points, indicating that the system attains a metallic conductivity. Hence, we call this phase as the topological semimetal with a pair of gapped Dirac cones. Note that the Chern numbers of the third and fourth bands are $N_{\rm Ch}^{3} = -1$ and $N_{\rm Ch}^{4} = +1$, respectively. As shown in Figs. 3.13(e) and (f), the Berry curvature of the fourth band has positive peaks that correspond to two gapped Dirac points. These positive Berry curvatures give rise to nonzero Hall conductivity, which will be discussed in Sec. 3.4.3. This photoinduced topological phase transition is nothing but the one that has been intensively studied since its prediction for a photodriven Dirac-electron system in graphene [11, 12, 13, 85].

As we increase the long-axis amplitude $E_{\rm L}^{\omega}$ of light, these two Dirac points get closer in the momentum space [Figs. 3.13(a) and (b), and Figs. 3.13(e) and (f)]. This approaching behavior of the Dirac points is caused by the band deformation due to the photoinduced anisotropic renormalization of the transfer integrals as discussed in Sec. 3.3. When $E_{\rm L}^{\omega}$ reaches around 15 MV/cm, these Dirac points collide [Figs. 3.13(c) and (g)], and eventually disappear [Figs. 3.13(d) and (h)]. After the disappearance of Dirac points, the quasienergy band structure still has a gap that separates the third and fourth bands as shown in Fig. 3.13(d). However, the system is no longer topological, that is, the Chern numbers of the third and fourth bands are both zero, indicating the emergence of nontopological phase under irradiation with relatively intense elliptically polarized light of $E_{\rm L}^{\omega} \gtrsim 15$ MV/cm. This phenomenon was studied before for the linearly polarized light in Sec. 3.3. The present result is an extension to the case of elliptically polarized light with $E_{\rm L}^{\omega} \gg E_{\rm S}^{\omega}$. Notice that this photoinduced phase transition is a transition from topological to nontopological phases and originates from a novel physical mechanism distinct from the usually argued mechanism based on the time-reversal symmetry breaking.

3.4.3 Photoinduced Hall conductivity

To see unusual aspects of this novel photoinduced topological phase transition, we calculate dependencies of several physical quantities on the long-axis amplitude $E_{\rm L}^{\omega}$ of light [Fig. 3.14]. The profile of the Chern number $N_{\rm Ch}^{4}$ in Fig. 3.14(a) depicts an abrupt change from +1 to 0 at $E_{\rm L}^{\omega} = 14.75$ MV/cm, indicating the occurence of photoinduced phase transition from topological to nontopological phases. Upon this change in the band topologies, the gap between the third and fourth bands is required to close. This can be seen in the profile of band gap $\tilde{E}_{\rm gap}$, which is defined in Eq. (3.62). Figure 3.14(a) displays the profile of $\tilde{E}_{\rm gap}$, which clearly indicates the closing of band gap at the point where the

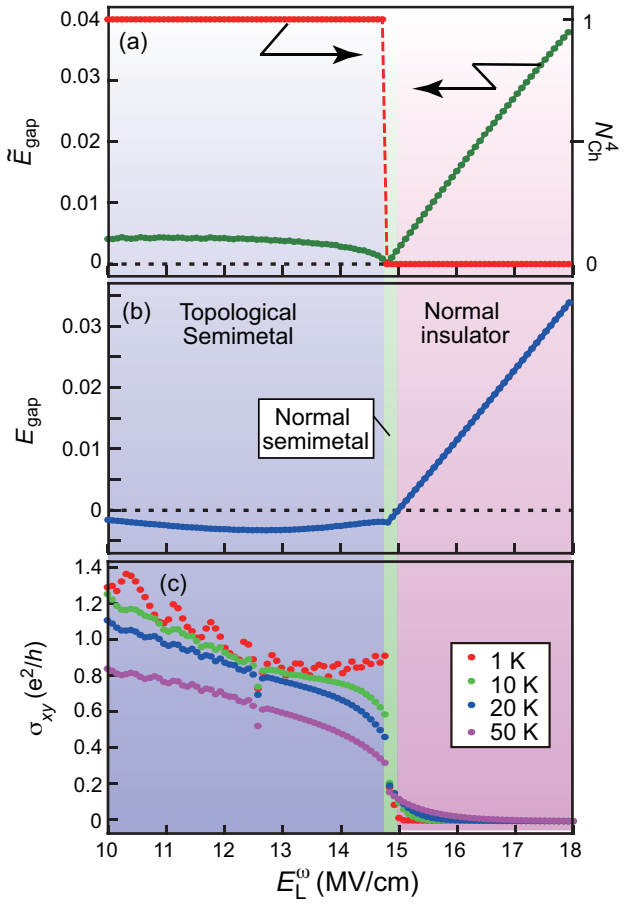

Figure 3.14. Calculated dependencies of several physical quantities, namely, (a) the band gap $\tilde{E}_{\rm gap}$, the Chern number of the fourth band $N^4_{\rm ch}$, (b) the energy gap $E_{\rm gap}$, and (c) the Hall conductivities σ_{xy} at various temperatures, on the long-axis amplitude $E^{\omega}_{\rm L}$ of light, which characterize the predicted novel photoinduced topological-to-nontopological phase transition accompanied with collision and collapse of the two Dirac points in α-(BEDT-TTF)$_2$I$_3$ irradiated with elliptically polarized light. The light parameters are set as $\hbar\omega = 0.6$ eV, $\alpha = 45°$, and $E^{\omega}_{\rm S} = 2$ MV/cm, respectively. Adapted from our previous study in Ref. [82].

Chern number changes from $N_{\rm Ch}^4 = +1$ to $N_{\rm Ch}^4 = 0$. Therefore, unlike the pair annihilation that occurs during the irradiation with linearly polarized light demonstrated in Sec. 3.3, this phenomenon is difficult to interpret in terms of the annihilation of the magnetic charges because the Chern numbers of the bands change during the disappearance of the Dirac points.

We also calculate another quantity called energy gap $E_{\rm gap}$ defined in Eq. (3.61). Figure 3.14(b) depicts the calculated $E_{\rm gap}$ as a function of the long-axis amplitude $E_{\rm L}^{\omega}$. According to this figure as well as Fig. 3.14(a), we find that a normal semimetal phase ($\tilde{E}_{\rm gap} > 0$ and $E_{\rm gap} < 0$) emerges in a small region of 14.75 MV/cm $< E_{\rm L}^{\omega} <$ 15 MV/cm next to the topological semimetal phase with nonzero Chern number. This phase is nontopological with a vanishing Chern number $N_{\rm Ch}^4 = 0$ and has a metallic conductivity with $E_{\rm gap} < 0$. In the subsequent region of $E_{\rm L}^{\omega} > 15$ MV/cm, the normal insulator phase appears with $N_{\rm Ch}^4 = 0$ and $E_{\rm gap} > 0$.

The present photoinduced topological phase transition can be seen in the profiles of photoinduced Hall conductivity σ_{xy} as well. The Hall conductivity σ_{xy} is a physical quantity that is sensitive to the topological properties of electronic states and thus can be exploited to identify topological phases characterized by nonzero Chern numbers. This quantity is associated with the Berry curvatures of bands $B_z^{\nu}(\boldsymbol{k})$ as

$$\sigma_{xy} = \frac{2e^2}{h} \int\int_{\rm BZ} \frac{dk_x dk_y}{2\pi} \sum_{\nu} n_{\nu}(\boldsymbol{k}) B_z^{\nu}(\boldsymbol{k}). \tag{3.78}$$

The factor 2 comes from the spin degeneracy [see Appendix B]. Here $n_{\nu}(\boldsymbol{k})$ is the nonequilibrium distribution function for the ν-th Floquet band in the photodriven steady states [41, 100, 106],

$$n_{\nu}(\boldsymbol{k}) = \frac{\langle \Phi_{\nu}^0(\boldsymbol{k}) | \hat{N}_{\boldsymbol{k}}(\varepsilon_{\nu}^0(\boldsymbol{k})) | \Phi_{\nu}^0(\boldsymbol{k}) \rangle}{\langle \Phi_{\nu}^0(\boldsymbol{k}) | \hat{A}_{\boldsymbol{k}}(\varepsilon_{\nu}^0(\boldsymbol{k})) | \Phi_{\nu}^0(\boldsymbol{k}) \rangle}. \tag{3.79}$$

This quantity is calculated using the Floquet–Keldysh formalism [41, 100, 106], which combines the Keldysh Green's function technique [101, 102] with the Floquet theory. The quantities $\hat{A}_{\boldsymbol{k}}$ and $\hat{N}_{\boldsymbol{k}}$ are given by,

$$\hat{A}_{\boldsymbol{k}}(\varepsilon) = \frac{i}{2\pi} \left(\hat{G}^{\rm R}(\boldsymbol{k}, \varepsilon) - \hat{G}^{\rm A}(\boldsymbol{k}, \varepsilon) \right), \tag{3.80}$$

$$\hat{N}_{\boldsymbol{k}}(\varepsilon) = -\frac{i}{2\pi} \hat{G}^{<}(\boldsymbol{k}, \varepsilon). \tag{3.81}$$

The lesser Green's function $\hat{G}^{<}$ and the lesser self-energy $\hat{\Sigma}^{<}$ are given, respectively, by,

$$\hat{G}^{<}(\boldsymbol{k}, \varepsilon) = \hat{G}^{\rm R}(\boldsymbol{k}, \varepsilon)\, \hat{\Sigma}^{<}(\varepsilon)\, \hat{G}^{\rm A}(\boldsymbol{k}, \varepsilon), \tag{3.82}$$

$$\hat{\Sigma}^{<}(\varepsilon) = \frac{\hat{\Sigma}^{\rm A} + \hat{\Sigma}^{\rm K}(\varepsilon) - \hat{\Sigma}^{\rm R}}{2}. \tag{3.83}$$

The retarded, advanced and Keldysh Green's functions $\hat{G}^{\rm R}$, $\hat{G}^{\rm A}$, and $\hat{G}^{\rm K}$ are obtained by

solving the following Dyson equation,

$$\begin{aligned}&\begin{pmatrix}\hat{G}^{\mathrm{R}}(\boldsymbol{k},\varepsilon) & \hat{G}^{\mathrm{K}}(\boldsymbol{k},\varepsilon)\\ 0 & \hat{G}^{\mathrm{A}}(\boldsymbol{k},\varepsilon)\end{pmatrix}^{-1}\\ &=\begin{pmatrix}[\hat{G}^{\mathrm{R0}}(\boldsymbol{k},\varepsilon)]^{-1} & 0\\ 0 & [\hat{G}^{\mathrm{A0}}(\boldsymbol{k},\varepsilon)]^{-1}\end{pmatrix}-\begin{pmatrix}\hat{\Sigma}^{\mathrm{R}} & \hat{\Sigma}^{\mathrm{K}}(\varepsilon)\\ 0 & \hat{\Sigma}^{\mathrm{A}}\end{pmatrix},\end{aligned} \tag{3.84}$$

where $\hat{\Sigma}^{\mathrm{R}}$, $\hat{\Sigma}^{\mathrm{A}}$ and $\hat{\Sigma}^{\mathrm{K}}$ are matrices of the retarded, advanced, and Keldysh self-energies, respectively. Each of the matrices is made up of $(2m_{\max}+1)\times(2m_{\max}+1)$ block matrices where we set $m_{\max}=8$ in the present study, while the size of each block matrix is 4×4. The matrix components of $\hat{G}^{\mathrm{R0}}$, $\hat{G}^{\mathrm{A0}}$, $\hat{\Sigma}^{\mathrm{R}}$, $\hat{\Sigma}^{\mathrm{A}}$ and $\hat{\Sigma}^{\mathrm{K}}$ are given respectively by

$$[\hat{G}^{\mathrm{R0}}(\boldsymbol{k},\varepsilon)]^{-1}_{n\nu,m\mu}=\varepsilon\delta_{n,m}\delta_{\nu,\mu}-\mathcal{H}_{n\nu,m\mu}(\boldsymbol{k}), \tag{3.85}$$

$$[\hat{G}^{\mathrm{A0}}(\boldsymbol{k},\varepsilon)]^{-1}_{n\nu,m\mu}=\varepsilon\delta_{n,m}\delta_{\nu,\mu}-\mathcal{H}_{n\nu,m\mu}(\boldsymbol{k}), \tag{3.86}$$

$$[\hat{\Sigma}^{\mathrm{R}}]_{n\nu,m\mu}=-i\Gamma\delta_{n,m}\delta_{\nu,\mu}, \tag{3.87}$$

$$[\hat{\Sigma}^{\mathrm{A}}]_{n\nu,m\mu}=i\Gamma\delta_{n,m}\delta_{\nu,\mu}, \tag{3.88}$$

$$[\hat{\Sigma}^{\mathrm{K}}(\varepsilon)]_{n\nu,m\mu}=-2i\Gamma\tanh\left[\frac{\varepsilon-\mu+m\omega}{2k_{\mathrm{B}}T_{\mathrm{hr}}}\right]\delta_{n,m}\delta_{\nu,\mu}. \tag{3.89}$$

Here the symbol $\hat{M}_{n\nu,m\mu}$ denotes the (ν,μ)th component of the (m,n)th block matrix $\hat{M}_{nm}$ (4×4), and the block matrix $\hat{\mathcal{H}}_{n,m}$ constituting the Floquet Hamiltonian is given by Eq. (2.77). We assume that the system is coupled to a heat reservoir at temperature T_{hr} with a dissipation coefficient Γ where we set $\Gamma=0.001$ eV for the calculations. For simplicity, we neglect the frequency-dependence and the momentum-dependence of the dissipation coefficient Γ, for which the dissipations appear only in the diagonal components of the self-energy matrices. In the calculations of $n_\nu(\boldsymbol{k})$, we phenomenologically introduced the damping rate Γ $(=0.001$ eV) to incorporate the effects of coupling to thermally fluctuating environment. Figure 3.14(c) shows the calculated E_{L}^{ω} dependencies of the photoinduced Hall conductivities σ_{xy} at various temperatures. This quantity takes large values in the topological semimetal phase with $N_{\mathrm{Ch}}^4=1$, but it decreases abruptly with a jump at the transition point to the normal semimetal phase with $N_{\mathrm{Ch}}^4=0$. In the normal insulator phase with $N_{\mathrm{Ch}}^4=0$, this quantity is almost suppressed to be zero. On the other hand, the Berry curvature does not become zero in the whole Brillouin zone by increasing the amplitude of light within the range of experimental realization before the disappearance of two Dirac points [79, 81]. These results indicate that the predicted successive photoinduced phase transitions might be experimentally detected by measurement of the Hall conductivity under the irradiation with the light. Additionally, it is observed that there are oscillations in the calculation results of the photoinduced Hall conductivities at all temperatures. These oscillations may arise due to finite-size effects, but the reasons for these oscillations are still unclear.

The emergence of normal semimetal phase in a small region between the topological semimetal phase and the normal insulator phase, namely, 14.75 MV/cm $<E_{\mathrm{L}}^{\omega}<$15

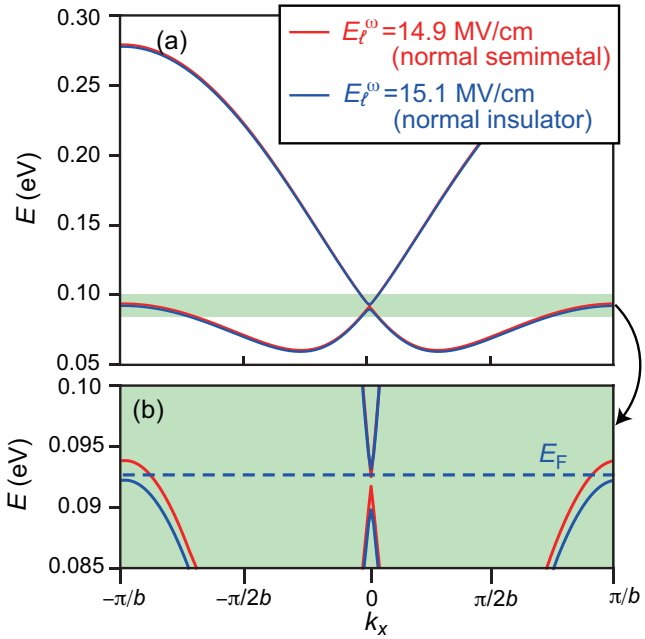

Figure 3.15. (a) Band structures along k_x at $k_y = \pi/a$ of α-(BEDT-TTF)$_2$I$_3$ irradiated with elliptically polarized light for different long-axis amplitudes of light, namely, $E_{\rm L}^{\omega} = 14.9$ MV/cm (normal semimetal phase) and $E_{\rm L}^{\omega} = 15.1$ MV/cm (normal insulator phase). (b) Magnified view of the band structure around the Fermi level. The light parameters are set to be $\hbar\omega = 0.6$ eV, $\alpha = 45°$, and $E_{\rm S}^{\omega} = 2$ MV/cm. Adapted from our previous study in Ref. [82].

MV/cm, can be discussed by focusing on the fine band structures. Figure 3.15(a) presents the quasienergy band structures along $(k_x, \pi/a)$ for $E_{\rm L}^{\omega} = 14.9$ MV/cm (normal semimetal phase) and $E_{\rm L}^{\omega} = 15.1$ MV/cm (normal insulator phase), while Fig. 3.15(b) magnifies those near the Fermi level. Both phases have finite band gaps $\tilde{E}_{\rm gap} > 0$ [Fig. 3.14(a)], manifested by a gap at $k_x = 0$. On the other hand, the sign of the energy gap $E_{\rm gap}$ is opposite between these two phases. The normal semimetal phase has a negative energy gap $E_{\rm gap} < 0$. This means that the Fermi level runs over the third and fourth bands, and thus the system becomes a semimetal with metallic conductivity. Meanwhile, the normal insulator phase has a positive energy gap $E_{\rm gap} > 0$. This means that the Fermi level runs within a gap between the third and fourth bands and does not cross these bands. As a result, the system attains insulating nature. As seen in Fig. 3.15(b), the third band crosses the Fermi level at $k_x = \pm\pi/b$ for the normal semimetal phase at $E_{\rm L}^{\omega} = 14.9$ MV/cm, whereas it does not for the normal insulator phase at $E_{\rm L}^{\omega} = 15.1$ MV/cm. In Fig. 3.12, we have summarized four possible band structures in the present system.

3.4.4 Phase diagram

In this section, we construct a nonequilibrium phase diagram of α-(BEDT-TTF)$_2$I$_3$ under the irradiation with elliptically polarized light by the physical quantities $\tilde{E}_{\rm gap}$, $E_{\rm gap}$, and $N_{\rm ch}^4$. Figure 3.16(a) depicts the phase diagram in plane of the short-axis amplitude $E_{\rm S}^{\omega}$ and the polarization angle α. Here the long-axis amplitude and the frequency of light are chosen as $E_{\rm L}^{\omega} = 18$ MV/cm and $\hbar\omega = 0.67$ eV, respectively. Notice that the type-I Dirac semimetal phase does not appear in this phase diagram because even a small $E_{\rm S}^{\omega}$ open a gap at the two Dirac points. In the limit of $E_{\rm S}^{\omega} = 0$, the light is linearly polarized. In this case, our previous work in Sec. 3.3 predicted that a pair annihilation of Dirac points occurs owing to the deformation of band structure due to the anisotropic renormalization of transfer integrals when $\alpha \sim 45^\circ$. This Dirac-point annihilation result in the emergence of normal insulator phase as shown in the phase diagram at $\alpha \sim 45^\circ$ and $E_{\rm S}^{\omega} = 0$. This normal insulator phase remains even if the light is not perfectly of linear polarization but elliptically polarized with nonzero $E_{\rm S}^{\omega}$ as long as the polarization angle α is nearly 45°. The phase diagram indicates that the normal insulator phase survives up to $E_{\rm S}^{\omega} \sim 7$ MV/cm, which corresponds to the ellipticity of $E_{\rm S}^{\omega}/E_{\rm L}^{\omega} \sim 0.39$. Meanwhile, when $E_{\rm S}^{\omega} \gtrsim 12$ MV/cm, the system is lying in the Chern insulator phase irrespective of the polarization angle α. It should be noted that when $E_{\rm S}^{\omega} = 18$ MV/cm, the light is of perfect circular polarization with $E_{\rm S}^{\omega} = E_{\rm L}^{\omega}$. We also note that when $\alpha = 0$, the phase diagram is consistent with the phase diagrams in Sec. 3.3.

Figure 3.16(a) displays the phase diagram for $E_{\rm L}^{\omega} = 18$ MV/cm, but even when different phases appear at a low amplitude of light, the photoinduced topological phase transition accompanied by the collision and collapse of the Dirac points occurs as long as there are gapped Dirac cones between the third and fourth bands. Hence, the phase diagram becomes more complicated at lower amplitudes, but the conclusions in this section remain unchanged. When the organic salt α-(BEDT-TTF)$_2$I$_3$ is irradiated by elliptically polarized light with nonzero $E_{\rm S}^{\omega}$, the Dirac points, if any, must be gapped because of the photoinduced breaking of time-reversal symmetry. Thereby, as long as the Dirac points exist, either the topological semimetal phase or the Chern insulator phase emerges. The

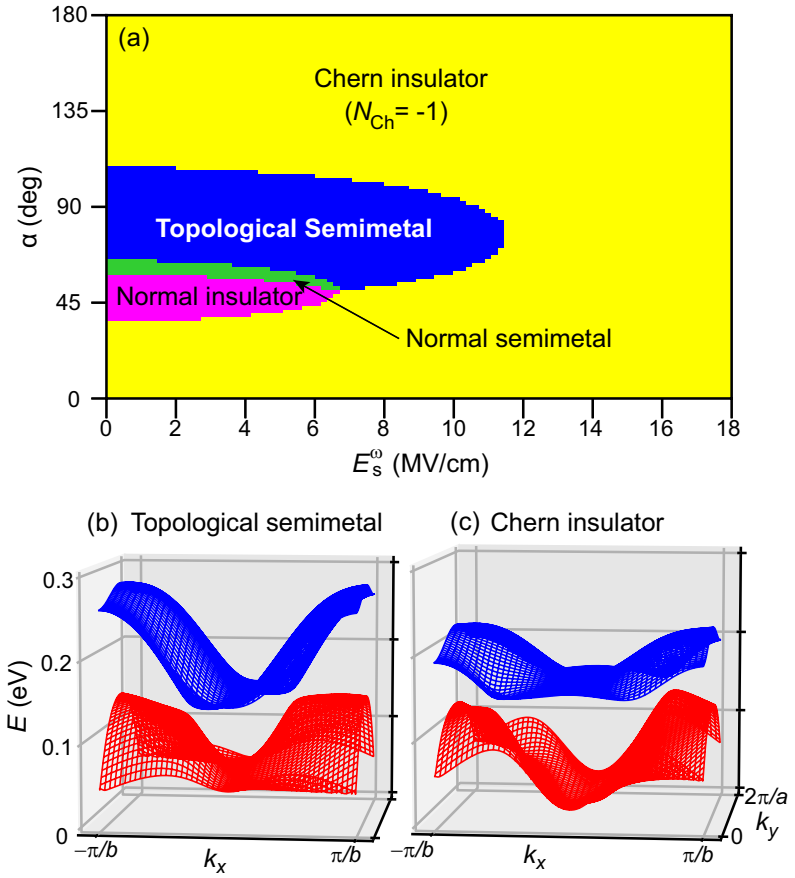

Figure 3.16. (a) Nonequilibrium phase diagram of photodriven α-(BEDT-TTF)$_2$I$_3$ under irradiation with elliptically polarized light in the plane of the short-axis amplitude E_S^ω and the polarization angle α of light when $\hbar\omega = 0.67$ eV and $E_L^\omega = 18$ MV/cm. The topological semimetal phase has gapped Dirac cones in its band structure. (b), (c) Typical quasienergy band structures of (b) the topological semimetal phase and (c) the Chern insulator phase, which are calculated for $\alpha = 90°$ and $\alpha = 135°$, respectively. The light parameters are set to be $\hbar\omega = 0.67$ eV, $E_S^\omega = 7$ MV/cm, and $E_L^\omega = 18$ MV/cm for both cases. Adapted from our previous study in Ref. [82].

topological semimetal phase has the bands crossing the Fermi level although the Dirac points are gapped, which carry the metallic conductivity. On the other hand, the Fermi level is located bewteen the well-separated third and fourth bands without crossing them in the Chern insulator phase, which renders the bulk insulating. Figures 3.16(b) and (c) show typical quaienergy band structures for the topological semimetal phase and the Chern insulator phase under irradiation with elliptically polarized light. It is noted that the quasienergy band structure in the Chern insulator phase in Fig. 3.16(c) is significantly deformed from the original band structue at equilibrium [Fig. 3.2(b)]. This exemplifies the photoinduced band deformation due to the anisotropic renormalization of transfer integrals.

3.5 Discussion

3.5.1 Band structure and off-resonant condition

In Sec. 3.3 and Sec. 3.4, the phase diagram for photoinduced nonequilibrium steady phases were classified according to the features of the Floquet band structures, whereas the band occupations were not considered for the classification. In fact, when the light frequency $\hbar\omega$ is around 0.6–0.8 eV, a series of the bands (ν=1,2,3,4) for the zero-photon states, which are located near the Fermi level, are separated from bands for the one-photon-absorbed ($n = +1$) states and those for the one-photon-emitted ($n = -1$) states (off-resonant situation). As explained earlier, in this situation, the nonequilibrium band-occupation function $f_{n\nu}(\boldsymbol{k})$ for the νth Floquet band approximately coincides with the Fermi–Dirac distribution function in the equilibrium as $f_{n\nu}(\boldsymbol{k}) \sim f_{\mathrm{FD}}(\varepsilon^n_\nu(\boldsymbol{k}))\delta_{n,0}$.

The frequency window of the off-resonant condition (i.e., $0.6 \lesssim \hbar\omega(\mathrm{eV}) \lesssim 0.8$) for α-(BEDT-TTF)$_2I_3$ is determined by the bandwidth W of the band set (ν=1,2,3,4) around the Fermi level relevant to electrons in the BEDT-TTF layer (i.e., the BEDT-TTF bands) and the energy spacing G between the Fermi level and the upper/lower bands. The first-principles calculation of this material in Ref. [107] demonstrated that both W and G are ~ 0.8 eV in the static case. In the photodriven system, the bandwidth W is renormalized as ~ 0.6 eV for the typical light amplitudes and frequencies examined in the present study. It should be noted that the bandwidth W is dependent of the amplitude of light. A set of the BEDT-TTF bands of the zero-photon states around the Fermi level overlaps that of the one-photon-absorbed (-emitted) states when $\hbar\omega \lesssim 0.6$ eV, whereas it overlaps the lower (upper) bands of the one-photon-absorbed (-emitted) states when $\hbar\omega \gtrsim 0.8$ eV, resulting in the on-resonant situation. The BEDT-TTF bands near the Fermi level are well separated from the upper and lower bands in this organic compound, which provides a rare opportunity to have a finite light-frequency window to realize the off-resonant situation. Thereby, α-(BEDT-TTF)$_2$I$_3$ is a precious example material for studying photoinduced nonequilibrium phases and photoinduced phase transitions because of this peculiar band structure as well as the charge ordering as a source of the staggered site potential necessary for the predicted pair annihilation phenomenon. We expect that slight overlaps of the bands with different photon numbers (i.e., the weak on-resonant situation) never alter the band occupation so drastically from the equilibrium

case that the phase classifications based on the Floquet band structure are valid to some extent even above and below this frequency window.

3.5.2 Experimental feasibility

We now discuss the feasibility of experimentally observing the predicted photoinduced pair annihilation triggered by linearly polarized light and the novel type of photoinduced topological phase transition induced by elliptically polarized light. Our quantitative predictions indicate that a rather strong light electric field of $E^{\omega}\sim$15 MV/cm is required to realize the dissaperance of a pair of Dirac-cone bands. We know that samples may be damaged or even broken under continuous irradiation with an intense light field, but it is difficult to discuss to what extent samples of the organic compound can endure an intense light field. However, we consider that the experiment is worth trying or even feasible for the following reasons. First, several experiments of photoinduced phase transitions have been successfully performed for similar organic materials, such as κ-type BEDT-TTF compounds, at least with few-cycle-pulse or one-cycle-pulse laser light as intense as E^{ω} =16 MV/cm [108, 109]. Second, although a continuous-wave photoexcitation was assumed in the present study in applying the Floquet theorem, it has been experimentally demonstrated that continuous-wave photoirradiation is not necessarily required to observe the nonequilibrium steady states or the Floquet states, and a small-number-cycle pulse or even a less-than-10-cycle pulse is sufficient [110, 111]. Third, it has been theoretically shown that because of electron correlation effects, the positions of the Dirac points in real materials are closer than those predicted using the present tight-binding model without electron correlations [88, 112]. Therefore, the collision of the two Dirac points may be realized with a light electric field weaker than the predicted field strength of $\sim$15 MV/cm. Of course, there may be difficulties in conducting real experiments, but it is expected that the predicted pair annihilation of the emergent magnetic charges and the novel type of photoinduced topological phase transition will be observed experimentally in the near future as the difficulties are overcome.

3.6 Conclusion

In conclusion, we have theoretically predicted novel phenomena and rich phases in photodriven α-(BEDT-TTF)$_2$I$_3$. In Sec. 3.2, we demonstrated the emergence of topological nontrivial phases in α-(BEDT-TTF)$_2$I$_3$ irradiated with circularly polarized light. Using the Floquet theory, we observed that irradiation with circularly polarized light opens a gap at the Dirac points, and the system becomes Chern insulator phase characterized by a nonzero Chern number and chiral edge states. In Sec. 3.3, we predicted the photoinduced pair annihilation of the emergent magnetic charges induced by linearly polarized light. This phenomenon is distinct from the photoinduced topological phase transition to the Chern insulater phase because linearly polarized light does not break the time-reversal symmetry. Therefore, this pair annihilation phenomenon is accompanied by a nontopological phase transition to normal insulator phase. We discussed that this phenomenon is attributed to the photoinduced anisotropic renormalizaion of the transfer

integrals by calculating the trajectory of the Dirac points. In addition, we constructed the phase diagram for the nonequilibrium steady state of photodriven α-(BEDT-TTF)$_2$I$_3$ and showed that the pair annihilation phenomenon only occurs when the polarization angle is around 45°. In Sec. 3.4, we predicted a novel type of photoinduced topological phase transition accompanied by the collision and collapse of two Dirac cones in α-(BEDT-TTF)$_2$I$_3$ irradiated with elliptically polarized light. We demonstrate that irradiation with elliptically polarized light, at a specific elliptical-axis angle, causes the collision of the Dirac points, leading to their collapse due to the photoinduced renormalization of the transfer integrals. This results in a topological phase transition from a semimetal with gapped Dirac cones (topological) to a normal insulator (non-topological), distinct from the photoinduced topological phase transition in Sec. 3.2. Using the Floquet-Keldysh formalism, we calculate the photoinduced Hall conductivity and argue that this novel type of photoinduced topological phase transition can be experimentally detected by measuring the Hall current. These three theoretical prediction enrich the fundamental physics of photoinduced topological phase transitions and are anticipated to be observed in experiments.

Chapter 4

Nonlinear optical responses in α-(BEDT-TTF)$_2$I$_3$

In this chapter, we study the dc photocurrent induced by light in the organic salt α-(BEDT-TTF)$_2$I$_3$. We focus on two nonlinear optical responses: shift current [Sec. 4.2] and injection current [Sec. 4.3]. Employing the perturbation theory outlined in Sec. 2.1, we calculate the dependence of the shift current and injection current on the frequency of light in photodriven α-(BEDT-TTF)$_2$I$_3$. Furthermore, we delve into the nonperturbative effects of the nonlinear optical responses using the Floquet theory detailed in Sec. 2.2.

4.1 Introduction

As discussed in Chap. 1, nonlinear optical responses, such as shift current and injection current, have been extensively explored from the perspectives of both fundamental science and electronic applications. Historically, these responses has been theoretically examined as second-order responses to a light electric field using perturbation theory [44, 45]. However, it is evident that higher-order terms contribute to the dc photocurrent, and such nonperturbative effects have not been fully elucidated. Recently, Morimoto and Nagaosa investigated the nonperturbative effects on the dc photocurrent in a restricted two-band system using Floquet theory, leading to a theoretical observation of saturation effect at higher light intensities [53]. This saturation effect has also been experimentally demonstrated [54, 113]. Nevertheless, a comprehensive understanding of nonlinear optical responses in multiband systems remains a subject that requires further investigation.

The organic conductor α-(BEDT-TTF)$_2$I$_3$ offers a unique opportunity for investigating nonlinear optical responses in multiband Dirac-electron systems. As discussed in Sec. 3.5, the four bands illustrated in Fig. 3.2(c) are situated around the Fermi level and are well-separated from the other bands, making it easier to examine the multiband effects among these four bands [80, 81, 82, 107]. In addition, this material is composed of large molecules and, as a result, has relatively large lattice constants ($a = 0.9187$ nm and $b = 1.0793$ nm) in comparison to graphene or transition metal dichalcogenides [114]. This leads to the enhancement of the effects of the light electric field, which is incorporated through Peierls phases on the transfer integrals [79, 80, 82]. Consequently, it becomes

possible to observe nonlinear effects at lower amplitude of light, making this material a promising system for investigating nonperturbative effects.

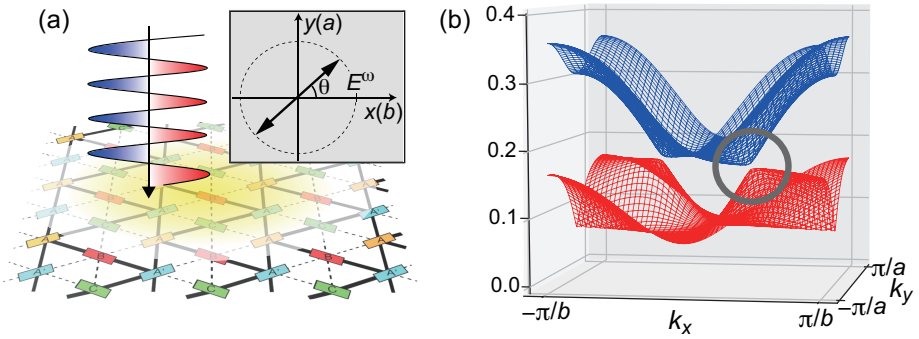

Figure 4.1. (a) Schematic of α-(BEDT-TTF)$_2$I$_3$ under the irradiation with linearly polarized light. (b) Band structure of α-(BEDT-TTF)$_2$I$_3$ obtained from a tight-binding model for two-dimensional BEDT-TTF layer. The staggered site potential in Eq. (3.1) is set as $\Delta = 0.01$ eV. Adapted from our previous study [83].

In the following, our focus is on two nonlinear optical responses, i.e., shift current in α-(BEDT-TTF)$_2$I$_3$ under the irradiation with linearly polarized light [Fig. 4.1] and injection current induced by circularly polarized light. These systems serve as examples of photodriven multiband Dirac-electron systems. Through the application of perturbation theory, we predict the emergence of the shift current and injection current in photodriven α-(BEDT-TTF)$_2$I$_3$, where the direction of the second-order responses being strongly contingent on the frequency of light. We uncover that this distinctive phenomenon arises from the multiband effect. Furthermore, we explore the nonperturbative effects by utilizing Floquet theory, revealing a change in the sign of the optical responses when the amplitude of light increases. We conduct a comparative analysis between the results obtained through Floquet theory and the equation proposed by Morimoto and Nagaosa, shedding light on the inherent nonlinear effects in this system.

4.2 Shift current

In this section, we focus on the dc photocurrent induced by linearly polarized light in α-(BEDT-TTF)$_2$I$_3$. As mentioned earlier, the dc photocurrent, referred to as shift current, is anticipated to be a promising alternative method for generating a large photocurrent, distinct from the method based on pn junctions. This section explores the frequency dependence of the second-order responses obtained through perturbation theory and the amplitude dependence of the nonlinear responses obtained using Floquet theory [44, 45]. We investigate the multiband effects through the analysis of the four band model for α-(BEDT-TTF)$_2$I$_3$, uncovering peculiar phenomena in photodriven α-(BEDT-TTF)$_2$I$_3$. The content of this chapter have been submitted to the academic journal [83].

4.2.1 Second-order responses

As explained in the previous chapter, the electronic structure of α-(BEDT-TTF)$_2$I$_3$ can be described using a tight-binding model as shown in Eq. (3.1). The breaking of inversion symmetry is required to realize a nonzero dc photocurrent, so we study the charge order state ($\Delta > 0$) in this section. We set the order parameter of $\Delta = 0.01$ eV, which can be realized experimentally by applying an appropriate uniaxial pressure [81].

The shift current is described by a rank-three tensor $\sigma^{\mu}_{\alpha\alpha}$, which is given by the formula in Eq. (2.69). As discussed in Sec. 2.1, this rank-three tensor is derived using the perturbation theory as presented in Eq. (2.72). In this section, we exclusively consider irradiation with linearly polarized light. Therefore, we do not take into account the injection current, which would be an additional contribution to the current density resulting from the breaking of time-reversal symmetry [45, 115, 116, 117].

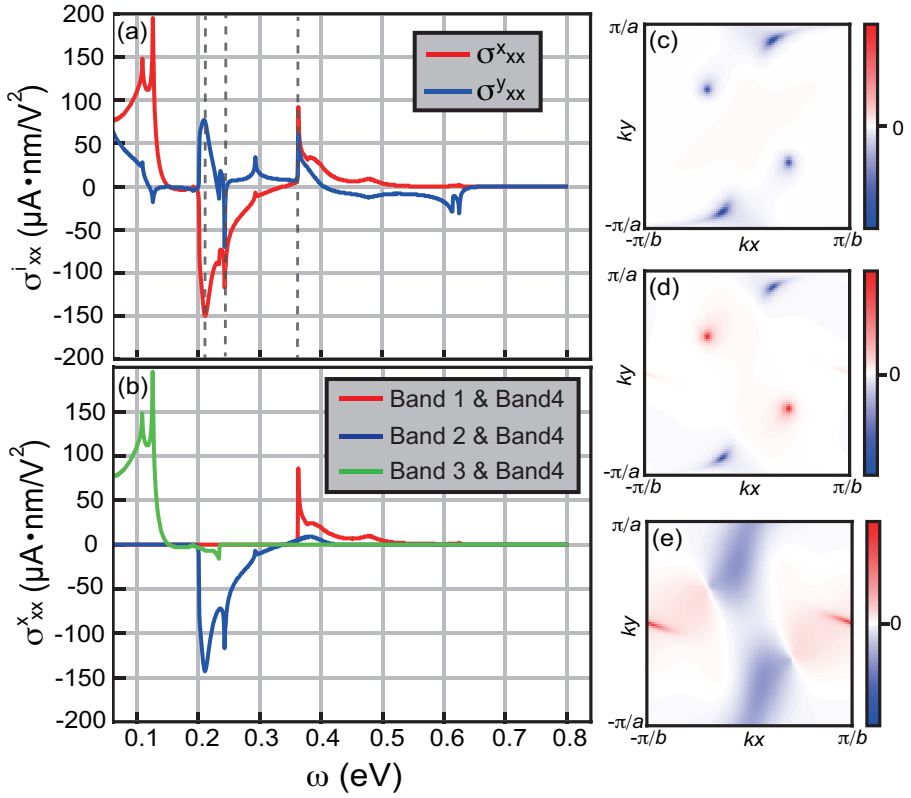

Figure 4.2. (a) Shift current conductivities for α-(BEDT-TTF)$_2$I$_3$ under the irradiation with linearly polarized light with the polarization angle of 0°. Red and green lines indicate the x and y components of the shift current. (b) Contribution to the x component of the shift current in photodriven α-(BEDT-TTF)$_2$I$_3$. Blue, green, and red lines indicate the contribution from the different transitions. (c-e) The multiplication of the shift vector S^x_{mn} and the velocity operator v^x_{mn} in the momentum space, for various band indices, (c) $m = 1$ and $n = 4$, (d) $m = 2$ and $n = 4$, and (e) $m = 3$ and $n = 4$. Adapted from our previous study [83].

Figure 4.2(a) illustrates the calculated results depicting the dependence of conductivity σ^x_{xx} and σ^y_{xx} on the frequency of light. In this figure, we consider linearly polarized light with a polarized angle $\theta = 0°$. Notably, we observe that the behavior of the conductivity σ^x_{xx} differs significantly from that of σ^y_{xx}. As a result, the frequency of light exerts a critical impact on both the magnitude of the current density and its direction. On the other hand, it is worth mentioning that the peaks in σ^x_{xx} and σ^y_{xx} occurs at the same frequency as depicted in Fig. 4.2(a). This suggests that these peaks are attributed to the joint density of states (DOS) term, represented by $\delta(\hbar\omega - \varepsilon_m + \varepsilon_n)$.

Now, let us delve into the reason behind the significant frequency-dependent variation in the direction of the shift current. We discover that, in addition to the complex crystal structure, the multiband effect plays a crucial role in manifesting this phenomenon. To investigate this further, we compute the contribution of the shift current arising from each transition between two bands [Fig. 4.2(b)]. We find that the contribution from the transition between the second and fourth bands is negative, whereas the contributions from other transitions are positive. This sign disparity in contributions is attributed to the sign of the shift vector S^α_{mn} defined in Eq. (2.73). Figures 4.2(c-e) depict the k-space profiles of the multiplication of the shift vector S^x_{mn} and the velocity operator v^x_{mn} [see Eq. (2.73)]. The shift current is obtained by multiplying the joint DOS term with $S^x_{mn}v^x_{mn}$ and integrate it across the Brillouin zone [see Eq. (2.72)]. Hence, the value of $S^x_{mn}v^x_{mn}$ at the k-point that satisfies $\hbar\omega = \varepsilon_m(\boldsymbol{k}) - \varepsilon_n(\boldsymbol{k})$ is the primary contribution to the shift current. As the quantity $S^x_{mn}v^x_{mn}$ is complex in momentum space, as shown in Fig. 4.2(c-e), the calculated contribution to the shift current from each transition, as shown in Fig. 4.2(b), becomes intricate when the frequency of light is altered.

4.2.2 Nonperturbative effects

Next, we explore nonperturbative effects on the dc photocurrent induced by linearly polarized light, employing the Floquet theory. As mentioned earlier, the nonlinear optical response in a restricted two-band system has been analyzed using the Floquet theory, leading to the theoretical observation of a saturation effect at high intensity of light [53]. We initially derived the static Floquet Hamiltonian. The Floquet Hamiltonian for the photodriven α-(BEDT-TTF)$_2$I$_3$ under the irradiation with linearly polarized light is derived in Sec. 3.3. Using the Floquet Hamiltonian, the expression for the dc photocurrent in α-(BEDT-TTF)$_2$I$_3$ is given by,

$$\begin{aligned} J^\mu &= \frac{ie}{2\pi\hbar}\int d^2\boldsymbol{k}\int d\nu\,\mathrm{Tr}\left[v_F G^<\right] \\ &= \frac{ie}{2\pi\hbar^2}\int d^2\boldsymbol{k}\int d\nu\,\mathrm{Tr}\left[\frac{\partial H_F}{\partial k_\mu}\frac{1}{\nu + i\Gamma/2 - H_F}\Sigma^<\frac{1}{\nu - i\Gamma/2 - H_F}\right]. \end{aligned} \tag{4.1}$$

Here, v_F represents the current operator under the irradiation, $G^<$ denotes the lesser Green function in the Keldysh formalism. The quantity Γ refers to the dissipation coefficient and $\Sigma^<$ is the lesser self-energy, which is defined as,

$$[\Sigma^<(\nu)]_{n\nu,m\mu} = i\Gamma\left(1 - \tanh\left[\frac{\nu - \mu + m\omega}{2k_B T_{\mathrm{hr}}}\right]\right)\delta_{n,m}\delta_{\nu,\mu}. \tag{4.2}$$

Here, we assume that the system couples to a heat reservoir at temperature $T_{\rm hr}$ with a dissipation coefficient Γ. In the following, we set $T_{\rm hr} = 0$.

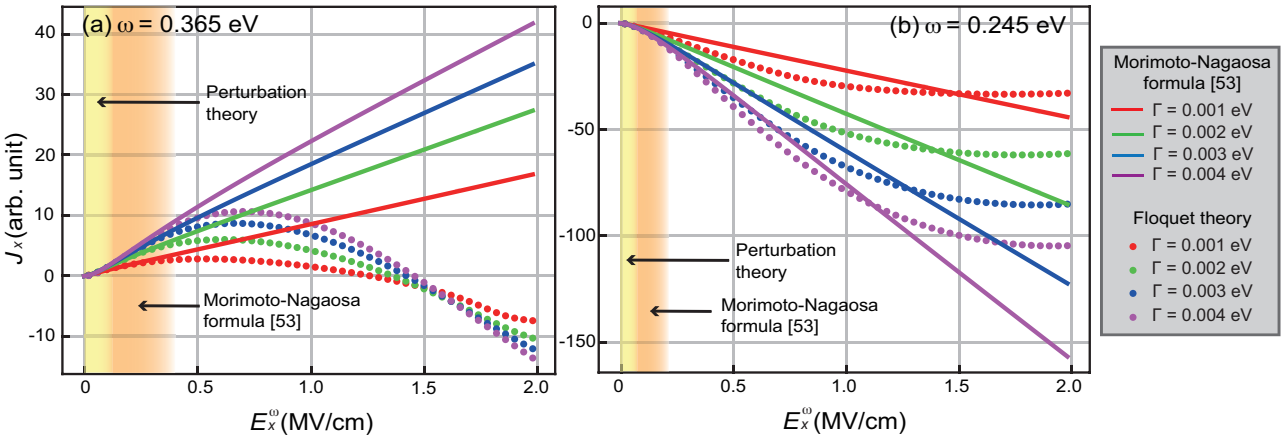

Figure 4.3. Calculated nonlinear optical responses for two light frequencies (a) $\omega = 0.365$ eV and (b) $\omega = 0.245$ eV derived in Floquet theory. These frequencies correspond to the peak frequency of the shift current in Fig. 4.2(a). Color plots illustrate the dc photocurrent obtained using the Eq. (4.1), while color lines represent the dc photocurrent derived by the equation in Ref. [53]. The dc photocurrents obtained using the Eq. (2.72) match those obtained from the Eq. (4.1) in yellow region. On the other hand, the photocurrent with the saturation factor is consistent with those obtained from Eq. (4.1) in orange region. Adapted from our previous study [83].

Figure 4.3(a) displays the calculated dc current in photodriven α-(BEDT-TTF)$_2$I$_3$ for various dissipation coefficients Γ. The color plots depict the results obtained using Eq. (4.1), while the colored lines show the outcomes calculated using the equation derived using a restricted two band model [53]:

$$J^a = -\frac{2\pi e^3 |E^\omega|^2}{\hbar^2} \sum_{n,m} \int \frac{d\boldsymbol{k}}{8\pi^3} f_{nm} \frac{\Gamma}{\sqrt{4e^2 |v^\mu_{mn}|^2 |E^\omega|^2/\omega^2 + \Gamma^2}} S^a_{nm} |r^b_{nm}|^2 \delta(\omega_{mn} - \omega). \quad (4.3)$$

Note that the above equation is the same as the one derived from perturbation theory, except for the saturation factor given by

$$\frac{\Gamma}{\sqrt{4e^2 |v^\mu_{mn}|^2 |E^\omega|^2/\omega^2 + \Gamma^2}}. \quad (4.4)$$

We verify that the photocurrent obtained using the Floquet theory is consistent with the results calculated using Eq. (2.72) when the intensity E^ω satisfies $E^\omega \lesssim 0.1$ MV/cm (yellow region). In fact, Eq. (2.72) is independent on the dissipation coefficient Γ, a feature that is only noticeable in Fig. 4.3(a) at the low intensity of light. On the other hand, the photocurrent calculated by Eq. (2.72) with the saturation factor match the results when $E^\omega \lesssim 0.3$ MV/cm (orange region). Notice that the saturation factor was derived in the restricted two-band system. Hence, the results in Fig. 4.3(a) contain

the multiband effect in nonlinear optical responses. We find that the saturation factor accounts for the saturation effect at intermediate intensity of the light, but it falls short at higher intensities. Indeed, the sign change of the dc photocurrent is observed around $E^{\omega} \sim 1.5$ MV/cm, while the saturation factor remains positive.

Let us discuss the applicable range for the equation derived from the perturbation theory. In the perturbation theory, we develop a perturbation expansion in terms of $eE^{\omega}a/\hbar\omega$ where a denotes the lattice constant of the system. Therefore, Eq. (2.72) is valid when the condition $eE^{\omega}a/\hbar\omega \ll 1$ is satisfied. As explained earlier, since the lattice constant in α-(BEDT-TTF)$_2$I$_3$ is considerably larger than that in materials like graphene or transition metal dichalcogenides, the expansion parameter $eE^{\omega}a/\hbar\omega$ can become large, leading to a pronounced manifestation of the nonlinear effect, as depicted in Fig. 4.3(a). In particular, we observe a sign change of the current density as the light intensity increases. In addition, $eE^{\omega}a/\hbar\omega$ becomes larger when working with lower-frequency light. Indeed, the range within which Eq. (2.72) remains applicable narrows when lower-frequency light is used [Fig. 4.3(b)]. We observe that the applicability of Eq. (2.72) with the saturation factor also diminishes as the frequency of light decreases. In other words, in the case of a multiband system, the saturation factor discussed in Ref. [53] has indeed expanded the applicable range of the equation but remains inadequate when dealing with higher $eE^{\omega}a/\hbar\omega$.

Finally, we investigate the dependence of the shift current on the linear polarization angle of light. In Fig. 4.4, the dc photocurrent density is presented as a function of the polarization angle for various amplitudes of light. Our findings reveal a significant dependence of the shift current on the polarization angle in photodriven α-(BEDT-TTF)$_2$I$_3$. Consequently, altering the polarization angle results in changes in both the magnitude and direction of the shift current. The dependence on the polarization angle exhibits slight variations for different light amplitudes [Figs. 4.4(a-d)]. Moreover, it is important to emphasize that changing the polarization angle leads to a change in the sign of the y-component of the shift current. These results emphasize that not only the frequency but also the polarization angle are crucial parameters affecting the magnitude and direction of nonlinear optical responses.

4.3 Injection current

In the previous section, we explored the dc photocurrent induced by linearly polarized light, where the injection current does not contribute to the resulting dc photocurrent. In this section, our focus shifts to the investigation of the dc photocurrent induced by circularly polarized light. In this scenario, the shift current term becomes negligible, and the injection current mainly contributes to the dc photocurrent. Employing perturbation theory, we analyze the frequency dependence of the dc photocurrent up to the second order. Remarkably, we observe that the injection current becomes a significantly larger at lower light frequencies compared to higher frequencies when the light intensity is small. Additionally, we delve into the nonperturbative effects on the injection current, revealing a strong suppression of the injection current at low light frequencies when the light intensity is high. The detailed findings of this section are currently being prepared

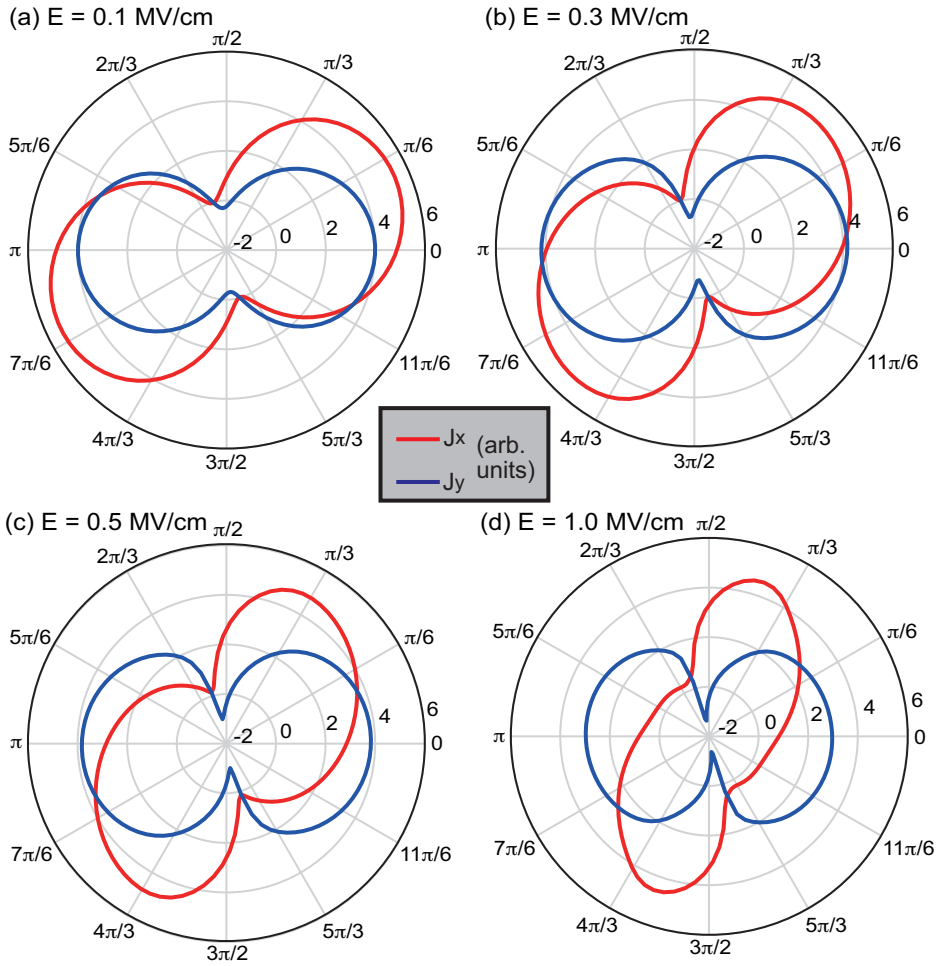

Figure 4.4. The polarization angle dependence on the dc photocurrent in α-(BEDT-TTF)$_2$I$_3$ for various intensities of light, (a) 0.1 MV/cm, (b) 0.3 MV/cm, (c) 0.5 MV/cm, and (d) 1.0 MV/cm. The frequency of light is fixed at $\omega = 0.365$ eV. Red and blue lines indicate the x and y components of the photocurrent. Adapted from our previous study [83].

for submission to an academic journal.

4.3.1 Second-order responses

In this section, we investigate the injection current using Eq. (2.68). Similar to the shift current, nonzero injection current requires the breaking of spatial inversion symmetry. Therefore, we choose the site potential of $\Delta = 0.01$ eV, the same value as in Sec. 4.2.

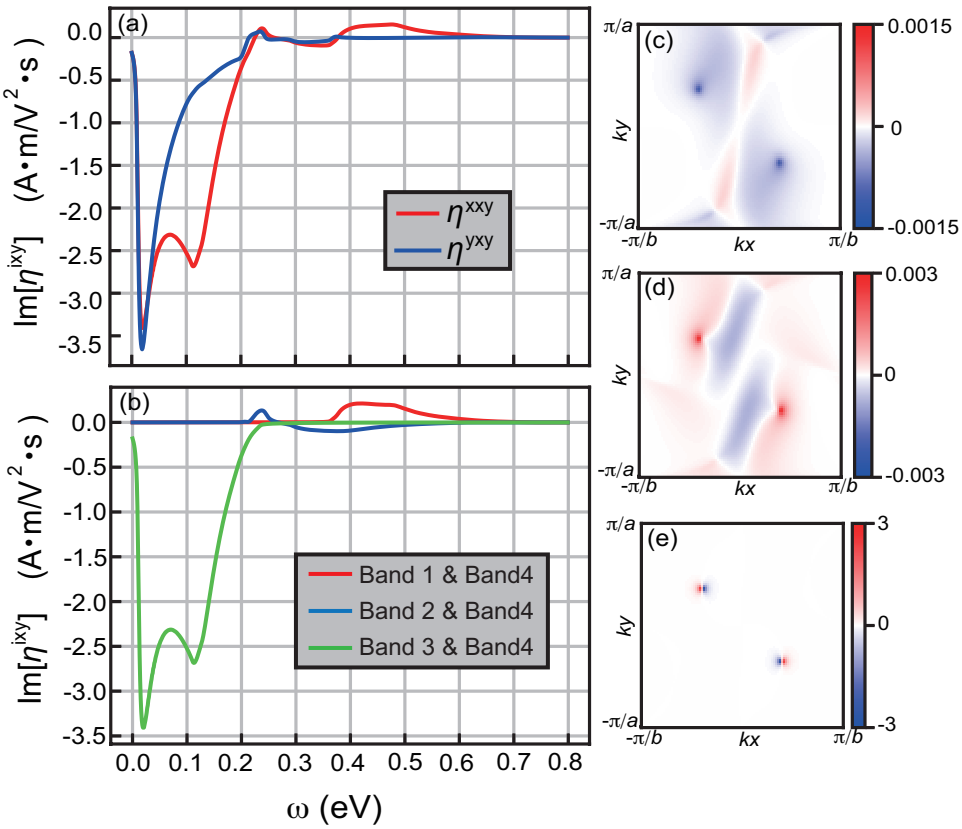

Figure 4.5. (a) Conductivities of the injection currents for α-(BEDT-TTF)$_2$I$_3$ irradiated with circularly polarized light. Red and blue lines correspond to the x and y components of the injection current. (b) Contribution to the x component of the injection current induced by circularly polarized light in α-(BEDT-TTF)$_2$I$_3$. Blue, green, and red lines indicate the contribution from the different transitions. (c-e) The imaginary part of the multiplication of $[r^x_{mn}(\boldsymbol{k}), r^y_{nm}(\boldsymbol{k})]$ and Δ_{mn} depicted in the momentum space, for various band indices, (c) $m = 1$ and $n = 4$, (d) $m = 2$ and $n = 4$, and (e) $m = 3$ and $n = 4$.

Figure 4.5(a) displays the frequency dependence of the injection current in α-(BEDT-TTF)$_2$I$_3$ under irradiation with circularly polarized light. In this figure, η^{xxy} (depicted by the red line) corresponds to the x-component of the injection current, while η^{yxy} (depicted by the blue line) corresponds to the y-component of the injection current when circularly polarized light is applied. Note that η^{xxy} and η^{yxy} are purely imaginary, and

we illustrate their imaginary parts in Fig. 4.5. Similar to the shift current, we observe that the frequency dependence of the conductivity η^{xxy} significantly differs from that of η^{yxy}, leading to a change in direction with varying light frequencies. For instance, there is a peak in η^{xxy} around $\omega = 0.1$ eV, while no peaks are observed in η^{yxy} at the same frequency.

It is worth noting that the units of injection-current conductivity differ from those in shift-current conductivity [see Eqs. (2.67) and (2.69)]. To compare the conductivities between injection and shift currents, it is necessary to multiply the injection-current conductivities by the relaxation time, denoted as $\tau = \hbar/\Gamma$. Assuming a relaxation time of 10^{-12} s, as used in Ref. [116], the largest peak in Fig. 4.5(a) reaches approximately ~ 3500 μA·nm/V^2, which is almost ten times larger than that of the shift current in Fig. 4.2. Moreover, with an assumed sample thickness of ~ 7 nm, the injection-current conductivity at the largest peak in Fig. 4.5(a) becomes nearly the same as the quantized circular photogalvanic effect in Weyl semimetals discussed in Ref. [116].

Moving forward, we delve into the contributions to the injection current from individual transitions. Figure 4.5(b) visually represents these contributions to the conductivity η^{xxy}. Remarkably, the contribution arising from the transition between the third and fourth bands significantly surpasses the contributions from other transitions. To comprehend the reasons for this dominance, we examine the product of Δ_{mn} and $[r^x_{mn}(\boldsymbol{k}), r^y_{nm}(\boldsymbol{k})]$ in Figs.4.5(c-e). It is pertinent to note that the injection-current conductivities are determined by this product and the delta function $\delta(\omega_{mn} - \omega)$ [see Eq.(2.68)]. In Fig.4.5(e), prominent peaks are observed, corresponding to the two Dirac points. These peaks are attributed to the portion of $[r^x_{mn}(\boldsymbol{k}), r^y_{nm}(\boldsymbol{k})]$, given that $r^x_{mn}(\boldsymbol{k})$ is proportional to $1/\omega_{mn}(\boldsymbol{k})$ [see Eq.(2.21)]. Consequently, peaks occur at points in momentum space where the bandgap $E_m(\boldsymbol{k}) - E_n(\boldsymbol{k})$ is minimal.

While contributions from other transitions are comparatively smaller, they are finite, as depicted in Fig. 4.5(b). These multiband effects, despite their smaller magnitudes, induce a change in the sign of the injection-current conductivity η^{xxy}. This nuanced behavior emphasizes the complexity introduced by multiband effects in the injection current response.

4.3.2 Nonperturbative effects

In this section, we explore the nonperturbative effects of the injection currents induced by circularly polarized light, similar to the treatment of the shift current. The formalism for the dc photocurrent in α-(BEDT-TTF)$_2$I$_3$ irradiated with circularly polarized light is expressed by the same equation as in the shift current [Eq. (4.1)]. We specifically consider the scenario where the system couples to a reservoir at a temperature of $T_{\rm hr} = 0$.

A theoretical study has examined nonperturbative effects in injection currents within a restricted two-band system [118]. The research finds that the relaxation time in the injection current undergoes a nonperturbative modification as follows:

$$\frac{\hbar}{\Gamma} \to \frac{\hbar}{\sqrt{4e^2|v^\mu_{mn}|^2|E^\omega|^2/\omega^2 + \Gamma^2}}. \tag{4.5}$$

It is crucial to note that this term depends on $\boldsymbol{k}$ and should be incorporated into the

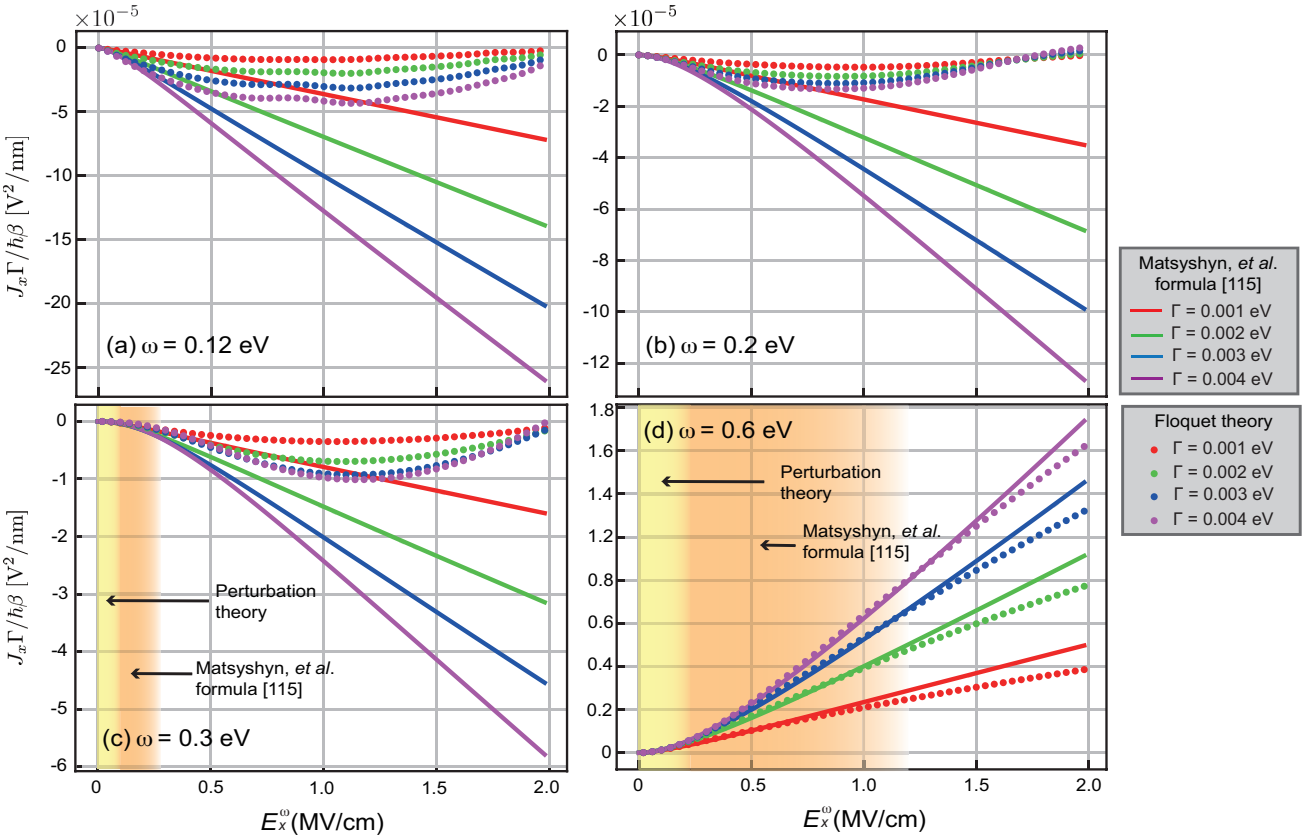

Figure 4.6. Calculated dc photocurrent induced by circularly polarized light for four different light frequencies (a) $\omega = 0.12$ eV, (b) $\omega = 0.2$ eV, (c) $\omega = 0.3$ eV, and (d) $\omega = 0.6$ eV derived in Floquet theory. Color plots illustrate the dc photocurrent obtained using the Eq. (4.1), while color lines represent the dc photocurrent derived by the equation in Ref. [118]. In this figure, β is defined as the quantized circular photogalvanic effect in Ref. [116], namely, $\beta = \pi e^3/h^2$.

integrand in Eq. (2.68). In other words, the injection current with the modification is given by,

$$J^a = -\frac{e^3\pi|E^\omega|^2}{2\hbar}\sum_{n,m,b,c}\int\frac{d\mathbf{k}}{8\pi^3}f_{nm}\frac{1}{\sqrt{4e^2|v^\mu_{mn}|^2|E^\omega|^2/\omega^2+\Gamma^2}}\Delta^a_{mn}\left[r^c_{mn},r^b_{nm}\right]\delta\left(\omega_{mn}-\omega\right). \tag{4.6}$$

We calculate the injection current using the above equation and compare it with the dc photocurrent obtained using Eq. (4.1) [Figs. 4.6(a-d)]. In Figs. 4.6(c,d), the results obtained using Eq. (4.1) match with the injection current obtained from the perturbation theory in the yellow region, while the results obtained from Eq. (4.1) and using the nonperturbative modification given by Eq. (4.5) are consistent in the orange region. We observe that the nonperturbative modification in Eq. (4.5) explains the saturation effect when $\omega = 0.6$ eV [Fig. 4.6(d)]. However, the dc photocurrent is strongly suppressed at smaller light frequencies compared to the results obtained by using the nonperturbative modification in Eq. (4.5) [Figs. 4.6(a-c)]. These results indicate that the multiband effect is important at lower frequencies, similar to the findings in the shift current. Additionally, we note that the sign change is observed in the dc photocurrent with varying light intensity in Fig. 4.6(b).

When the system is clean and the relaxation time τ is large, the injection current is typically larger than the shift current because the injection current is proportional to τ. Therefore, the injection current induced by circularly polarized light is usually larger than the shift current induced by linearly polarized light. In the case of this material, the injection current is approximately ten times larger than the shift current when considering up to the second order, as discussed in Sec. 4.3.1. Additionally, the dc photocurrent induced by circularly polarized light tends to be suppressed when the intensity is large due to the nonperturbative effect, so the shift current may become larger in this material. However, the behavior of saturation at the high light intensity is complex and differs with varying light frequencies. Therefore, a comprehensive analysis using a sufficiently large Floquet Hamiltonian is required to compare these currents.

Chapter 5

Summary

In this dissertation, we have delved into the exploration of physical phenomena within light-irradiated systems, with a specific emphasis on two significant aspects: (1) Topological phase transitions induced by light and (2) nonlinear responses to light electric fields. These phenomena have garnered considerable attention, propelled by the remarkable advancements in laser technology, becoming focal points of extensive research. However, a significant portion of these studies has predominantly focused on two-dimensional systems, including transition metal dichalcogenides, or simplistic toy models. Limited attention has been given to investigations based on realistic models for specific materials. To propel this promising research field forward, it is crucial to extend the scope to a broader range of target materials. Therefore, there is a pressing need for theoretical inquiries that concentrate on real materials characterized by intricate electronic and crystalline structures. Engaging in studies involving tangible materials holds the potential to uncover more diverse and material-specific photoinduced topological phenomena. In line with this objective, we have explored the photoinduced phenomena in the organic conductor α-(BEDT-TTF)$_2$I$_3$, which features two tilted Dirac cones in its band structure.

In Chap. 2, we have reviewed two methods for analyzing photodriven systems. The first method is based on perturbation theory with respect to the light electric field. We concentrate on the second-order response of the current density operator and derive expressions for the shift and injection currents. The second method utilizes Floquet theory, designed for the analysis of time-periodic systems. We derive the static effective Hamiltonian for the photodriven tight-binding model, a key element in Chap. 3 and Chap. 4. One notable advantage of employing Floquet theory over perturbation theory is its capability to explore nonperturbative effects.

In Chap. 3, we delve into the photoinduced topological phase transition in α-(BEDT-TTF)$_2$I$_3$. Using the Floquet static Hamiltonian derived in Chap. 2, we demonstrate three distinctive topological phase transitions in this material: (1) a topological phase transition to the Chern insulator phase induced by irradiation with circularly polarized light, (2) the pair annihilation of emergent magnetic charges induced by irradiation with linearly polarized light, and (3) a novel type of photoinduced topological phase transition accompanied by the collision and collapse of two Dirac cones induced by elliptically polarized light. The topological phase transition induced by circularly polarized light is attributed to the breaking of time-reversal symmetry, and the pair annihilation of

magnetic charges occurs due to the photoinduced anisotropic renormalization of transfer integrals. On the other hand, the novel type of photoinduced topological phase transition is a transition from a topological to a nontopological phase when two Dirac cones collide and collapse due to the renormalization of transfer integrals. To the best of our knowledge, this organic conductor is the only material where the pair annihilation and the collision and collapse of two Dirac cones are realized. These theoretical predictions highlight α-(BEDT-TTF)$_2$I$_3$ as a unique material that provides a rare opportunity to explore a variety of photoinduced phase-transition phenomena.

In Chap. 4, we investigate the dc photocurrent induced by light in α-(BEDT-TTF)$_2$I$_3$, focusing on two distinct nonlinear optical responses: shift and injection current. By applying the perturbation theory discussed in Chap. 2, we determine the dependencies of these currents on the frequency of light. Notably, we discover that the direction of these currents strongly depends on the frequency of light, and this unique dependence is attributed to multiband effects. Furthermore, we explore the nonperturbative effects of the shift and injection current using the Floquet Hamiltonian derived in Chap. 2. Our findings reveal a sign change in these responses, a phenomenon not observable when considering only the second-order response. We discuss the limitations of both the equation derived by the perturbation theory and the one derived by Morimoto and Nagaosa when the light intensity is large.

While we have addressed two significant photoinduced phenomena in α-(BEDT-TTF)$_2$I$_3$, several important questions and related aspects remain. One such aspect is the consideration of the relaxation process after irradiation with light. The nonequilibrium steady state is the focus of this thesis, but understanding the dynamics of the system, especially in the context of experiments using pulsed laser light to prevent sample heating, is crucial. Another important consideration is the more precise incorporation of the effects of interaction terms. In this study, we accounted for the effect of interaction by adding the site potential to the A and A$'$ sites. However, a more in-depth analysis using Floquet dynamical mean field theory may reveal even more peculiar phenomena in these materials. Addressing these challenges will be fascinating directions for future studies.

Appendix A

Injection and shift currents from the Fermi-Golden rule

In this section, we develop the formalism for the injection and shift currents using the Fermi-Golden rule [45, 119, 120]. This derivation is relatively simple compared to the one using perturbation theory in Sec. 2.1. The injection current $\partial \boldsymbol{j}_{\text{injection}}(t)/\partial t$ is determined by the change in velocity $\boldsymbol{\Delta}_{mn}(\boldsymbol{k}) = \boldsymbol{v}_{mm}(\boldsymbol{k}) - \boldsymbol{v}_{nn}(\boldsymbol{k})$ of the electron during an interband transition from an initial state m to a final state n. Therefore, the injection current is given by,

$$\frac{\partial j^c_{\text{injection}}}{\partial t} = \sum_{n,m} \int \frac{d\boldsymbol{k}}{8\pi^3} \left(-e\Delta^c_{mn}(\boldsymbol{k})\right) f_{nm} \mathcal{M}_{m\leftarrow n}, \tag{A.1}$$

where $\mathcal{M}_{m\leftarrow n}$ denotes the transition rate from an initial state n to a final state m. Here, n labels the occupied state and m labels the unoccupied state. Utilizing the Fermi-Golden rule, the transition rate from the perturbation term of $H'e^{-i\omega t}$ is given by,

$$\mathcal{M}_{m\leftarrow n}(\omega) = \frac{2\pi}{\hbar} |\langle m|H'|n\rangle|^2 \delta(E_m - E_n - \hbar\omega). \tag{A.2}$$

In this section, we assume the same light electric field $\boldsymbol{E}(t) = \boldsymbol{E}(\omega)e^{-i\omega t} + \boldsymbol{E}(-\omega)e^{i\omega t}$ as in Sec. 2.1. When this light is irradiated onto the system, the Hamiltonian changes as:

$$\begin{aligned} H_0(\boldsymbol{k}) &\to H_0(\boldsymbol{k} + e\boldsymbol{A}(t)/\hbar) \\ &= H_0(\boldsymbol{k}) + \frac{e\boldsymbol{A}(t)}{\hbar} \cdot \frac{\partial H_0(\boldsymbol{k})}{\partial \boldsymbol{k}} \\ &= H_0(\boldsymbol{k}) - \frac{ie\boldsymbol{E}(\omega)}{\hbar\omega} \cdot \frac{\partial H_0(\boldsymbol{k})}{\partial \boldsymbol{k}} e^{-i\omega t} + \frac{ie\boldsymbol{E}(-\omega)}{\hbar\omega} \cdot \frac{\partial H_0(\boldsymbol{k})}{\partial \boldsymbol{k}} e^{i\omega t}. \end{aligned} \tag{A.3}$$

There are two perturbation terms that contribute to the transition rate, but the contribution from the third term on the right-hand side of Eq. (A.3) does not affect to the transition rate. This is because the third term result in a term with $\delta(E_m - E_n + \hbar\omega)$ [see Eq. (A.2)]. Therefore, we consider the second term on the right-hand side of Eq. (A.3)

in the following. Using Eqs. (A.2) and (A.3), the transition rate can be calculated as,

$$\begin{aligned}
\mathcal{M}_{m\leftarrow n}(\omega) &= \frac{2\pi}{\hbar^2}|\,\langle m|H'|n\rangle\,|^2\delta(\omega_{mn}-\omega) \\
&= \frac{2\pi}{\hbar^2}\left|\sum_a \langle m|\frac{eE^a(\omega)}{\hbar\omega}\frac{\partial H_0(\boldsymbol{k})}{\partial k_a}|n\rangle\right|^2\delta(\omega_{mn}-\omega) \\
&= \frac{2\pi e^2}{\hbar^2}\sum_{a,b}\frac{\langle n|\partial_b H_0(\boldsymbol{k})|m\rangle}{\hbar\omega_{mn}}\frac{\langle m|\partial_a H_0(\boldsymbol{k})|n\rangle}{\hbar\omega_{mn}}\delta(\omega_{mn}-\omega)E^a(\omega)E^b(-\omega) \\
&= \frac{2\pi e^2}{\hbar^2}\sum_{a,b} r^b_{nm}r^a_{mn}\delta(\omega_{mn}-\omega)E^a(\omega)E^b(-\omega). \qquad \text{(A.4)}
\end{aligned}$$

Using Eqs. (A.1) and (A.4), the injection current is given by,

$$\frac{\partial j^c_{\text{injection}}}{\partial t} = -\frac{2\pi e^3}{\hbar^2}\sum_{n,m}\sum_{a,b}\int\frac{d\boldsymbol{k}}{8\pi^3}f_{nm}\Delta^c_{mn}r^b_{nm}r^a_{mn}\delta(\omega_{mn}-\omega)E^a(\omega)E^b(-\omega). \qquad \text{(A.5)}$$

The above equation is consistent with Eqs. (2.67) and (2.68).

The shift current can be derived using the same method as in Eq. (A.5). The shift current is determined by the transition rate and the shift vector $\boldsymbol{S}_{mn}(\boldsymbol{k})$, which corresponds to the change of the position of an electron in real-space. Therefore, the shift current is given by,

$$\begin{aligned}
j^c_{\text{shift}} &= \sum_{n,m}\int\frac{d\boldsymbol{k}}{8\pi^3}\left(-eS^c_{mn}(\boldsymbol{k})\right)f_{nm}\mathcal{M}_{m\leftarrow n} \\
&= -\frac{2\pi e^3}{\hbar^2}\sum_{n,m}\sum_{a,b}\int\frac{d\boldsymbol{k}}{8\pi^3}f_{nm}S^c_{mn}(\boldsymbol{k})r^b_{nm}r^a_{mn}\delta(\omega_{mn}-\omega)E^a(\omega)E^b(-\omega). \qquad \text{(A.6)}
\end{aligned}$$

The above equation is consistent with Eqs. (2.69) and (2.72).

Appendix B

Derivation of TKNN formula in Floquet systems

In this Appendix, we derive the expression for the photoinduced Hall conductivity using linear response theory for Floquet systems [11, 14, 121, 122]. We begin with a time-periodically driven system with a frequency of ω and define the creation and annihilation operators of an electron in Floquet states. Subsequently, we consider a scenario where a small periodic field is applied in addition to the time-periodic force with frequency ω. We discuss the current response to this small periodic field based on perturbation theory and derive the TKNN formula for Floquet systems. We conclude this appendix by discussing the relationship between the photoinduced Hall conductivity and the Berry curvature of the quasienergy band structure.

B.1 Creation and annihilation operators for Floquet state

In this section, we define the creation operator that creates a particle in a Floquet state. As explained in Sec. 2.2, a Floquet system is governed by a time-periodic Hamiltonian $H_0(t) = H_0(t+T)$, where T is the period of the system. In the time-periodic system, the electron is characterized by a quasienergy and Floquet state. The creation(annihilation) operator in Floquet systems is defined as,

$$a_\nu^\dagger(t) = \int d\boldsymbol{r}\phi_\nu(\boldsymbol{r},t)\Psi^\dagger(\boldsymbol{r}), \tag{B.1}$$

where $\phi_\nu(\boldsymbol{r},t)$ denotes the time-periodic wave function defined as $\phi_\nu(\boldsymbol{r},t) = \langle \boldsymbol{r}|\Phi_\nu(t)\rangle$ with the Floquet state $|\Phi_\nu(t)\rangle$ in Eq. (2.75). Here, the Fermionic field creation(annihilation) operator is given by $\Psi^\dagger(\boldsymbol{r})(\Psi(\boldsymbol{r}))$, which satisfies the anticommutation relations,

$$\{\Psi(\boldsymbol{r}), \Psi^\dagger(\boldsymbol{r}')\} = \delta(\boldsymbol{r}-\boldsymbol{r}'). \tag{B.2}$$

The annihilation operator $a_\nu(t)$ is defined in the same way as the creation operator in Eq. (B.1).

In time-dependent systems, the time evolution operator is given by,

$$U_0(t,t_0) = \mathcal{T}\exp\left[-i\int_{t_0}^{t} H_0(t')dt'\right], \tag{B.3}$$

where $\mathcal{T}$ denotes the time-ordered product. Using this operator, the time-dependent operator $A(t)$ in the Schrödinger picture is transformed as $A_H(t) = U_0^\dagger(t,t_0)A(t)U_0(t,t_0)$ in the Heisenberg picture. Using this equation, when we assume that there are no interactions, the creation and annihilation operators in the Heisenberg picture are given by,

$$a_{\nu,H}^\dagger(t) = e^{i\varepsilon_\nu(t-t_0)/\hbar}a_\nu^\dagger(t_0) \tag{B.4}$$

$$a_{\nu,H}(t) = e^{-i\varepsilon_\nu(t-t_0)/\hbar}a_\nu(t_0), \tag{B.5}$$

where ε_ν is the quasienergy that corresponds to the Floquet state $|\Phi_\nu(t)\rangle$. Then, the anticommutation relation in the Heisenberg picture is given by,

$$\{a_{\nu,H}(t), a_{\nu',H}^\dagger(t')\} = e^{-i\varepsilon_\nu(t-t')}\delta_{\nu,\nu'}. \tag{B.6}$$

B.2 Linear response theory in Floquet systems

In the following, we consider the linear response when a small periodic field with frequency Ω is applied to the system in addition to the time-periodic driving force with frequency ω. The Hamiltonian for the system with the small periodic field is given by $H(t) = H_0(t)+F(t)B(t)$, where $B(t)$ is a time-periodic operator with a frequency of ω and $F(t)$ is a time-dependent function. We define the density matrix $\rho_0(t)$ that characterizes the nonequilibrium steady state before the small periodic field is applied. Note that $\rho_0(t)$ is a time-periodic operator that satisfies $\rho_0(t) = \rho_0(t+T)$.

Next, we consider how a time-periodic operator $A(t) = A(t+T)$ changes by applying the small periodic field with a frequency of Ω. We define the change in the expectation value of $A(t)$ as,

$$\delta\langle A(t)\rangle = \mathrm{Tr}\{\rho(t)A(t)\} - \mathrm{Tr}\{\rho_0(t)A(t)\}. \tag{B.7}$$

In analogy to the equilibrium case, $\delta\langle A(t)\rangle$ is expected to be given by,

$$\delta\langle A(t)\rangle = \int_{-\infty}^{\infty} dt'\tilde{\chi}(t,t')F(t'), \tag{B.8}$$

where the response function $\tilde{\chi}(t,t')$ is defined as,

$$\tilde{\chi}(t,t') = -i\theta(t-t')\mathrm{Tr}\left\{\rho_0(t_0)[A_I(t), B_I(t')]\right\}. \tag{B.9}$$

Here the operator $A_I(t)$ in the interaction picture is given by,

$$A_I(t) = U_0^\dagger(t,t_0)A(t)U_0(t,t_0). \tag{B.10}$$

It should be noted that the right-hand side in Eq. (B.9) is not dependent on t_0 even though there are terms with $\rho_0(t_0)$.

The time-periodicity of the response function $\tilde{\chi}(t,t')$ is derived by following calculation:

$$\begin{aligned}\tilde{\chi}(t+T,t'+T) &= -i\theta(t-t')\mathrm{Tr}\left\{\rho_0(t_0)[A_I(t+T),B_I(t'+T)]\right\}\\ &= -i\theta(t-t')\mathrm{Tr}\left\{\rho_0(t_0-T)U_0^\dagger(t_0,t_0-T)[A_I(t),B_I(t')]U_0(t_0,t_0-T)\right\}\\ &= -i\theta(t-t')\mathrm{Tr}\left\{\rho_0(t_0)[A_I(t),B_I(t')]\right\}\\ &= \tilde{\chi}(t,t'). \end{aligned} \tag{B.11}$$

In this calculation, we use the fact that $\rho_0(t)$ and $U_0(t+\tau,t)$ are periodic functions with a period T. We then define a new response function as $\chi(\tau,t') \equiv \tilde{\chi}(t'+\tau,t')$. The new response function $\chi(\tau,t')$ is a periodic function in terms of τ, so we perform Fourier transformation and Fourier series expansion with respect to τ and t', respectively, and obtain the following equation:

$$\chi(\tau,t') = \sum_m \int_{-\infty}^{\infty} d\Omega e^{-i\Omega\tau} e^{-im\omega t'} \chi^{(m)}(\Omega). \tag{B.12}$$

By substituting this equation into Eq. (B.8), $\delta\langle A(t)\rangle$ is given by,

$$\delta\langle A(\Omega)\rangle = \sum_m \chi^{(m)}(\Omega) F(\Omega - m\omega). \tag{B.13}$$

In this appendix, we assume that Ω is sufficiently smaller than ω, and $F(\Omega')$ is nonzero only when $\Omega' \gg \Omega$. Then, only $m=0$ should be considered, and $\delta\langle A(t)\rangle$ is rewritten as,

$$\delta\langle A(\Omega)\rangle = \bar{\chi}(\tau) F(\Omega), \tag{B.14}$$

where we define the time-average of the response function as $\bar{\chi}(\tau) = 1/T \int_0^T dt' \chi(\tau,t')$.

So far, we have developed a general linear response theory, and now we discuss a system in which an AC electric field with a small oscillation frequency of Ω is added to a periodically driven system of frequency ω induced by light. Let $\boldsymbol{A}_0(t)$ and $\delta\boldsymbol{A}(t)$ be the vector potentials generated by the external field with frequency ω and that with frequency Ω, respectively. Then, the total vector potential is given by $\boldsymbol{A}(t) = \boldsymbol{A}_0(t) + \delta\boldsymbol{A}(t)$. Note that $\boldsymbol{A}_0(t)$ is a periodic function that holds $\boldsymbol{A}_0(t) = \boldsymbol{A}_0(t+T)$. By taking the perturbation of $H(t)$ with respect to $\delta\boldsymbol{A}(t)$, the Hamiltonian is rewritten as,

$$H(t) = H(t)|_{\delta\boldsymbol{A}(t)=0} + \left.\frac{\partial H(t)}{\partial \boldsymbol{A}(t)}\right|_{\delta\boldsymbol{A}(t)=0} \cdot \delta\boldsymbol{A}(t) + \frac{1}{2}\left.\frac{\partial^2 H(t)}{\partial A_\alpha(t)\partial A_\beta(t)}\right|_{\delta\boldsymbol{A}(t)=0} \delta A_\alpha(t)\delta A_\beta(t) \tag{B.15}$$

In this equation, the indices α and β denote the coordinates x, y, and z, and are summed over. In analogy to the equilibrium case, we define the paramagnetic current operator $\boldsymbol{J}^{(p)}(t)$ and kinetic operator $K_{\alpha\beta}(t)$ as,

$$\boldsymbol{J}^{(p)}(t) = -\left.\frac{\partial H(t)}{\partial \boldsymbol{A}(t)}\right|_{\delta\boldsymbol{A}(t)=0}, K_{\alpha\beta}(t) = -\frac{1}{2}\left.\frac{\partial^2 H(t)}{\partial A_\alpha \partial A_\beta}\right|_{\delta\boldsymbol{A}(t)=0}. \tag{B.16}$$

Using these operators, the expectation value of the current operator is given by,

$$\begin{aligned}\langle J_\alpha(t)\rangle &= \mathrm{Tr}[\rho(t)J_\alpha(t)] \\ &= \langle J_\alpha^{(p)}(t)\rangle + \sum_\beta \mathrm{Tr}\left[\rho_0(t)K_{\alpha\beta}(t)\right]\delta A_\beta(t) + O\left([\delta\boldsymbol{A}(t)]^2\right)\end{aligned} \tag{B.17}$$

It should be noted that we need to consider the first order of $\delta\boldsymbol{A}(t)$ in the first term of right-hand side in Eq. (B.17). We call the first term of right-hand side in Eq. (B.17) as the paramagnetic current term, and the second term the diamagnetic current term.

Then, we consider the linear response of the paramagnetic current term with respect to $\delta\boldsymbol{A}(t)$. Here, we consider the change in the expectation value of $J_\alpha^{(p)}(t)$ due to the term $\delta\boldsymbol{A}(t)$. Using Eqs. (B.8) and (B.9), $\delta\langle J_\alpha^{(p)}(t)\rangle$ is given by,

$$\delta\langle J_\alpha^{(p)}(t)\rangle = \int_{-\infty}^{\infty} dt' \chi_{\alpha\beta}(t-t',t')\delta A_\beta(t'), \tag{B.18}$$

where the response function is given by,

$$\chi_{\alpha\beta}(\tau,t') = -i\theta(\tau)\mathrm{Tr}\left\{\rho_0(t_0)[J_{\alpha,I}^{(p)}(t'+\tau), J_{\beta,I}^{(p)}(t')]\right\}. \tag{B.19}$$

Using Eq. (B.12), $\delta\langle J_\alpha^{(p)}(t)\rangle$ is transformed as,

$$\delta\langle J_\alpha^{(p)}\rangle(\Omega) = \int_{-\infty}^{\infty} dt' \sum_m e^{i(\Omega-m\omega)t'}\chi_{\alpha\beta}^{(m)}(\Omega)\delta A_\beta(t'). \tag{B.20}$$

When we choose the gauge which satisfies $\boldsymbol{E}(t) = -\partial\boldsymbol{A}(t)/\partial t$, the above equation is rewritten as,

$$\delta\langle J_\alpha^{(p)}\rangle(\Omega) = \sum_m \frac{\chi_{\alpha\beta}^{(m)}(\Omega)}{i(\Omega-m\omega)}\delta E_\beta(\Omega-m\omega). \tag{B.21}$$

In the following, we assume that $\delta\boldsymbol{A}(t)$ appears only in the second-order term $H^{(2)}(t) = \sum_{\boldsymbol{k}} h_{ij}(t)c_i^\dagger c_j$ with respect to creation and annihilation operator. For instance, the tight-binding model in which the transfer integrals are multiplied by the Peierls phases is one example. In terms of the basis of Floquet states, using the creation and annihilation operators $a_{\boldsymbol{k}\nu}^\dagger(t)(a_{\boldsymbol{k}\nu}(t))$ for an electron in a Floquet state, the second-order term in which $\delta\boldsymbol{A}(t)$ appears is written as $H^{(2)}(t) = \sum_{\boldsymbol{k}} h_{\nu_1\nu_2}(t)a_{\boldsymbol{k}\nu_1}^\dagger a_{\boldsymbol{k}\nu_2}$, where ν labels the Floquet state. Then, the current operator is given by,

$$J_\alpha^{(p)}(t) = \sum_{\boldsymbol{k}} j_{\alpha,\nu_1\nu_2}(\boldsymbol{k},t)a_{\boldsymbol{k}\nu_1}^\dagger(t)a_{\boldsymbol{k}\nu_2}(t). \tag{B.22}$$

Here, $j_{\alpha,\nu_1\nu_2}(\boldsymbol{k},t)$ is given by,

$$j_{\alpha,\nu_1\nu_2}(\boldsymbol{k},t) = -\left.\frac{\partial h_{\nu_1\nu_2}(\boldsymbol{k},t)}{\partial A_\alpha(t)}\right|_{\delta\boldsymbol{A}(t)=0} = -\left.\langle\phi_{\boldsymbol{k},\nu_1}(t)|\frac{\partial\check{h}(t)}{\partial A_\alpha(t)}|\phi_{\boldsymbol{k},\nu_2}(t)\rangle\right|_{\delta\boldsymbol{A}(t)=0}, \tag{B.23}$$

where $\check{h}(t)$ is a matrix of single-particle operators whose matrix elements are given by $h_{ij}(t)$.

In addition, we assume that the density operator of the nonequilibrium steady state in the absence of the small periodic field is given by,

$$\rho_0(t) = \prod_{\boldsymbol{k}\nu} [f_{\boldsymbol{k}\nu} a^\dagger_{\boldsymbol{k}\nu}(t) a_{\boldsymbol{k}\nu}(t) + (1 - f_{\boldsymbol{k}\nu}) a_{\boldsymbol{k}\nu}(t) a^\dagger_{\boldsymbol{k}\nu}(t)], \tag{B.24}$$

where $f_{\boldsymbol{k}\nu}$ is the nonequilibrium distribution function for a Floquet state characterized by the wave number $\boldsymbol{k}$ and the Floquet band ν. Using Eqs. (B.4) and (B.5), the following relation holds:

$$\mathrm{Tr}\left[\rho_0(t_0) a^\dagger_{I,\boldsymbol{k}\nu}(t_1) a_{I,\boldsymbol{k}'\nu'}(t_2)\right] = f_{\boldsymbol{k}\nu} e^{i\varepsilon_{\boldsymbol{k}}(t_1 - t_2)} \delta_{\boldsymbol{k},\boldsymbol{k}'} \delta_{\nu,\nu'}. \tag{B.25}$$

Using this equation, the response function in Eq. (B.19) is given by,

$$\chi_{\alpha\beta}(\tau, t') = -i\theta(\tau) \sum_{\boldsymbol{k}} \sum_{\nu_1\nu_2} e^{i(\varepsilon_{\boldsymbol{k}\nu_1} - \varepsilon_{\boldsymbol{k}\nu_2})} (f_{\boldsymbol{k}\nu_1} - f_{\boldsymbol{k}\nu_2}) j_{\alpha,\nu_1\nu_2}(\boldsymbol{k}, t' + \tau) j_{\beta,\nu_2\nu_1}(\boldsymbol{k}, t') \tag{B.26}$$

The matrix elements $j_{\alpha,\nu_1\nu_2}(\boldsymbol{k}, t)$ are time-periodic function in terms of t, so we perform the Fourier series expansion as,

$$j_{\alpha,\nu_1\nu_2}(\boldsymbol{k}, t) = \sum_m e^{-im\omega t} j^{(m)}_{\alpha,\nu_1\nu_2}(\boldsymbol{k}). \tag{B.27}$$

Then, by performing the Fourier series expansion and Fourier transformation as shown in Eq. (B.12), the response function in Eq. (B.26) is given by,

$$\chi^{(m)}_{\alpha\beta}(\Omega) = \sum_{\boldsymbol{k}} \sum_{\nu_1\nu_2} \sum_m \frac{(f_{\boldsymbol{k}\nu_1} - f_{\boldsymbol{k}\nu_2}) j^{(m)}_{\alpha,\nu_1\nu_2}(\boldsymbol{k}) j^{(-m)}_{\beta,\nu_2\nu_1}(\boldsymbol{k})}{\Omega - m\omega + (\varepsilon_{\boldsymbol{k}\nu_1} - \varepsilon_{\boldsymbol{k}\nu_2}) + i\eta}. \tag{B.28}$$

By substituting this equation into Eq. (B.21), we can obtain the change in the paramagnetic current term due to a small periodic field with frequency Ω.

On the other hand, the contribution of the diamagnetic current term to the change in the current operator $\delta\langle J_\alpha(\Omega)\rangle$ is obtained by performing the Fourier transformation of the second term on the right-hand side in Eq. (B.17). This contribution is calculated as,

$$\int_{-\infty}^{\infty} dt e^{i\Omega t} \mathrm{Tr}\left[\rho_0(t) K_{\alpha\beta}(t)\right] \delta A_\beta(t). \tag{B.29}$$

The kinetic operator $K_{\alpha,\beta}(t)$ is time-periodic, so we perform the Fourier transformation of $\mathrm{Tr}\left[\rho_0(t) K_{\alpha\beta}(t)\right]$ as,

$$\mathrm{Tr}\left[\rho_0(t) K_{\alpha\beta}(t)\right] = \sum_m \mathcal{K}^{(m)}_{\alpha,\beta} e^{-im\omega t}. \tag{B.30}$$

Using this equation, the change in the expectation value of current operator due to the diamagnetic term is given by,

$$\sum_m \frac{\mathcal{K}^{(m)}_{\alpha,\beta}}{i(\Omega - m\omega)} \delta E_\alpha(\Omega + m\omega). \tag{B.31}$$

The paramagnetic and diamagnetic current terms together contribute to the conductivity as follows:

$$\sigma_{\alpha\beta}(\Omega) = \frac{\chi^{(0)}_{\alpha\beta}(\Omega) + \mathcal{K}^{(0)}_{\alpha\beta}}{i\Omega}. \tag{B.32}$$

Eqs. (B.28) and (B.32) maintain the same form as in the equilibrium system. The key distinction lies in replacing the Fermi distribution function and energy eigenvalues from the equilibrium system with the nonequilibrium distribution function $f_{\boldsymbol{k}\nu}$ and quasienergy $\varepsilon_{\boldsymbol{k}\nu}$, respectively. Additionally, the inner product of the current operators in Floquet systems is replaced by,

$$j^{(0)}_{\alpha,\nu_1\nu_2} = -\frac{1}{T}\int_0^T dt\, \langle\phi_{\boldsymbol{k},\nu_1}(t)|\, \frac{\partial\check{h}(t)}{\partial A_\alpha(t)}\, |\phi_{\boldsymbol{k},\nu_2}(t)\rangle \Big|_{\delta\boldsymbol{A}(t)=0}. \tag{B.33}$$

Therefore, the equation for the photoinduced Hall conductivity can be derived in a manner similar to the equilibrium system. The photoinduced Hall conductivity in Floquet system is expressed as,

$$\sigma_{xy} = \frac{e^2}{h}\int \frac{d\boldsymbol{k}}{(2\pi)^3}\sum_\nu f_{\boldsymbol{k}\nu}[\nabla_{\boldsymbol{k}} \times A_\alpha(\boldsymbol{k})]_z, \tag{B.34}$$

where the Berry connection in Floquet systems is defined as,

$$A_\alpha(\boldsymbol{k}) = -\frac{i}{T}\int_0^T dt\, \langle\phi_{\boldsymbol{k},\nu_1}(t)|\, \nabla_{\boldsymbol{k}}\, |\phi_{\boldsymbol{k},\nu_2}(t)\rangle\,. \tag{B.35}$$

This equation is utilized in Section 3.4.3 to obtain the Hall conductivity in the photodriven α-(BEDT-TTF)$_2$I$_3$.

Acknowledgements

First of all, I would like to express my sincere appreciation to my supervisor, Prof. Masao Ogata, for his unwavering support and invaluable scientific discussions. Without his guidance, this thesis would not have taken shape in its organized structure. I am also deeply grateful to my previous supervisor, Prof. Masahito Mochizuki, for the fruitful discussions and support that initiated the studies presented in this thesis. His insights and advice were quite instrumental in shaping the stages of my research.

I extend my heartfelt thanks to Dr. Yasuhiro Tanaka, a research collaborator, for engaging discussions on organic conductors. I am also indebted to Prof. Philipp Werner and Prof. Michael Schüler for their enlightening discussions and insightful advice. Their generosity provided me with the opportunity to study in Switzerland for two months, and I appreciate the valuable scientific exchanges and guidance during that time. Special thanks to Prof. Mikito Koshino and Mr. Takaaki Joya for their contributions to the discussions on shift currents. I would like to acknowledge all my colleagues in the Ogata group for their scientific discussions and support.

I also express my appreciation to the referees of this thesis, Prof. Takashi Oka, Prof. Naoya Tajima, Prof. Shinji Tsuneyuki, Prof. Tohru Okamoto, and Prof. Toshihito Osada. We conducted useful discussions, and they provided valuable advice to improve this thesis.

I would also like to express my gratitude for the support received through the Program for Leading Graduate Schools (MERIT). My thanks to the assistant supervisor, Prof. Shuji Hasegawa, for fruitful discussions and guidance within the MERIT program.

Last but not least, I extend my thanks to my parents and friends for their unwavering support and encouragement throughout this journey.

Bibliography

[1] K. v. Klitzing, G. Dorda, and M. Pepper: Physical Review Letters **45**, 494 (1980).

[2] R. B. Laughlin: Physical Review B **23**, 5632 (1981).

[3] D. J. Thouless, M. Kohmoto, M. P. Nightingale, and M. den Nijs: Physical Review Letters **49**, 405 (1982).

[4] M. Kohmoto: Annals of Physics **160**, 343 (1985).

[5] Y. Hatsugai: Physical Review Letters **71**, 3697 (1993).

[6] C. L. Kane and E. J. Mele: Physical Review Letters **95**, 226801 (2005).

[7] M. Z. Hasan and C. L. Kane: Reviews of Modern Physics **82**, 3045 (2010).

[8] L. Fu, C. L. Kane, and E. J. Mele: Physical Review Letters **98**, 106803 (2007).

[9] X.-L. Qi and S.-C. Zhang: Reviews of Modern Physics **83**, 1057 (2011).

[10] F. D. M. Haldane: Physical Review Letters **61**, 2015 (1988).

[11] T. Oka and H. Aoki: Physical Review B **79**, 081406 (2009).

[12] T. Kitagawa, T. Oka, A. Brataas, L. Fu, and E. Demler: Physical Review B **84**, 235108 (2011).

[13] J.-i. Inoue and A. Tanaka: Physical Review Letters **105**, 017401 (2010).

[14] M. S. Rudner and N. H. Lindner: Nature Reviews Physics **2**, 229 (2020).

[15] T. Kitagawa, E. Berg, M. Rudner, and E. Demler: Physical Review B **82**, 235114 (2010).

[16] R. Roy and F. Harper: Physical Review B **96**, 155118 (2017).

[17] M. Nakagawa, R.-J. Slager, S. Higashikawa, and T. Oka: Physical Review B **101**, 075108 (2020).

[18] M. Sato, S. Takayoshi, and T. Oka: Physical Review Letters **117**, 147202 (2016).

[19] T. Mori: Physical Review B **98**, 104303 (2018).

[20] D. V. Else, B. Bauer, and C. Nayak: Physical Review Letters **117**, 090402 (2016).

[21] T. N. Ikeda and M. Sato: Science Advances **6**, eabb4019 (2020).

[22] C. Dai, Z. Shi, and X. Yi: Physical Review A **93**, 032121 (2016).

[23] L. D'Alessio and M. Rigol: Nature Communications **6**, 8336 (2015).

[24] M. Messer, K. Sandholzer, F. Görg, J. Minguzzi, R. Desbuquois, and T. Esslinger: Physical Review Letters **121**, 233603 (2018).

[25] Y. Tanaka and M. Mochizuki: Physical Review B **104**, 085123 (2021).

[26] Y. Tanaka and M. Mochizuki: Physical Review Letters **129**, 047402 (2022).

[27] N. H. Lindner, G. Refael, and V. Galitski: Nature Physics **7**, 490 (2011).

[28] M. Ezawa: Physical Review Letters **110**, 026603 (2013).

[29] M. Claassen, C. Jia, B. Moritz, and T. P. Devereaux: Nature Communications **7**, 13074 (2016).

[30] A. Huamán and G. Usaj: Physical Review B **99**, 075423 (2019).

[31] P. X. Nguyen and W.-K. Tse: Physical Review B **103**, 125420 (2021).

[32] X. Kong, W. Luo, L. Li, M. Yoon, T. Berlijn, and L. Liang: 2D Materials **9**, 025005 (2022).

[33] Z. Yan and Z. Wang: Physical Review Letters **117**, 087402 (2016).

[34] M. Ezawa: Physical Review B **96**, 041205 (2017).

[35] R. Chen, B. Zhou, and D.-H. Xu: Physical Review B **97**, 155152 (2018).

[36] M. S. Rudner, N. H. Lindner, E. Berg, and M. Levin: Physical Review X **3**, 031005 (2013).

[37] P. M. Perez-Piskunow, G. Usaj, C. A. Balseiro, and L. F. Torres: Physical Review B **89**, 121401 (2014).

[38] G. Usaj, P. M. Perez-Piskunow, L. F. Torres, and C. A. Balseiro: Physical Review B **90**, 115423 (2014).

[39] H. Dehghani, T. Oka, and A. Mitra: Physical Review B **90**, 195429 (2014).

[40] H. Dehghani, T. Oka, and A. Mitra: Physical Review B **91**, 155422 (2015).

[41] H. Aoki, N. Tsuji, M. Eckstein, M. Kollar, T. Oka, and P. Werner: Reviews of Modern Physics **86**, 779 (2014).

[42] Z. Gu, H. Fertig, D. P. Arovas, and A. Auerbach: Physical Review Letters **107**, 216601 (2011).

[43] T. Oka and S. Kitamura: Annual Review of Condensed Matter Physics **10**, 387 (2019).

[44] R. von Baltz and W. Kraut: Physical Review B **23**, 5590 (1981).

[45] J. E. Sipe and A. I. Shkrebtii: Physical Review B **61**, 5337 (2000).

[46] D. E. Parker, T. Morimoto, J. Orenstein, and J. E. Moore: Physical Review B **99**, 045121 (2019).

[47] D. A. Kleinman: Physical Review **128**, 1761 (1962).

[48] Y. Shen: Annual Review of Physical Chemistry **40**, 327 (1989).

[49] G. Hodes: Science **342**, 317 (2013).

[50] L. Z. Tan, F. Zheng, S. M. Young, F. Wang, S. Liu, and A. M. Rappe: npj Computational Materials **2**, 1 (2016).

[51] C. Aversa and J. E. Sipe: Physical Review B **52**, 14636 (1995).

[52] D. Passos, G. Ventura, J. V. P. Lopes, J. L. dos Santos, and N. Peres: Physical Review B **97**, 235446 (2018).

[53] T. Morimoto and N. Nagaosa: Science Advances **2**, e1501524 (2016).

[54] T. Akamatsu, T. Ideue, L. Zhou, Y. Dong, S. Kitamura, M. Yoshii, D. Yang, M. Onga, Y. Nakagawa, K. Watanabe, et al.: Science **372**, 68 (2021).

[55] Q. Ma, R. Krishna Kumar, S.-Y. Xu, F. H. Koppens, and J. C. Song: Nature Reviews Physics **5**, 170 (2023).

[56] J. Ahn, G.-Y. Guo, N. Nagaosa, and A. Vishwanath: Nature Physics **18**, 290 (2022).

[57] H. Watanabe and Y. Yanase: Physical Review X **11**, 011001 (2021).

[58] H. Wang and X. Qian: npj Computational Materials **6**, 199 (2020).

[59] Y. Zhang, T. Holder, H. Ishizuka, F. de Juan, N. Nagaosa, C. Felser, and B. Yan: Nature Communications **10**, 3783 (2019).

[60] L. D'Alessio and M. Rigol: Physical Review X **4**, 041048 (2014).

[61] A. Lazarides, A. Das, and R. Moessner: Physical Review E **90**, 012110 (2014).

[62] T. Kuwahara, T. Mori, and K. Saito: Annals of Physics **367**, 96 (2016).

[63] T. Mori, T. Kuwahara, and K. Saito: Physical Review Letters **116**, 120401 (2016).

[64] D. Abanin, W. De Roeck, W. W. Ho, and F. Huveneers: Communications in Mathematical Physics **354**, 809 (2017).

[65] D. A. Abanin, W. De Roeck, W. W. Ho, and F. Huveneers: Physical Review B **95**, 014112 (2017).

[66] M. C. Rechtsman, J. M. Zeuner, Y. Plotnik, Y. Lumer, D. Podolsky, F. Dreisow, S. Nolte, M. Segev, and A. Szameit: Nature **496**, 196 (2013).

[67] M. C. Rechtsman, Y. Plotnik, J. M. Zeuner, D. Song, Z. Chen, A. Szameit, and M. Segev: Physical Review Letters **111**, 103901 (2013).

[68] G. Jotzu, M. Messer, R. Desbuquois, M. Lebrat, T. Uehlinger, D. Greif, and T. Esslinger: Nature **515**, 237 (2014).

[69] H. Lignier, C. Sias, D. Ciampini, Y. Singh, A. Zenesini, O. Morsch, and E. Arimondo: Physical Review Letters **99**, 220403 (2007).

[70] J. W. McIver, B. Schulte, F.-U. Stein, T. Matsuyama, G. Jotzu, G. Meier, and A. Cavalleri: Nature Physics **16**, 38 (2020).

[71] D. H. Auston: Applied Physics Letters **26**, 101 (1975).

[72] S. Sato, J. McIver, M. Nuske, P. Tang, G. Jotzu, B. Schulte, H. Hübener, U. De Giovannini, L. Mathey, M. Sentef, et al.: Physical Review B **99**, 214302 (2019).

[73] M. Nuske, L. Broers, B. Schulte, G. Jotzu, S. Sato, A. Cavalleri, A. Rubio, J. McIver, and L. Mathey: Physical Review Research **2**, 043408 (2020).

[74] S. Sato, P. Tang, M. Sentef, U. De Giovannini, H. Hübener, and A. Rubio: New Journal of Physics **21**, 093005 (2019).

[75] Y. Hirai, N. Yoshikawa, M. Kawaguchi, M. Hayashi, S. Okumura, T. Oka, and R. Shimano: arXiv preprint arXiv:2301.06072 (2023).

[76] Y. Murotani, N. Kanda, T. Fujimoto, T. Matsuda, M. Goyal, J. Yoshinobu, Y. Kobayashi, T. Oka, S. Stemmer, and R. Matsunaga: arXiv preprint arXiv:2310.01093 (2023).

[77] H. Hübener, M. A. Sentef, U. De Giovannini, A. F. Kemper, and A. Rubio: Nature Communications **8**, 13940 (2017).

[78] K. Kajita, Y. Nishio, N. Tajima, Y. Suzumura, and A. Kobayashi: Journal of the Physical Society of Japan **83**, 072002 (2014).

[79] K. Kitayama and M. Mochizuki: Physical Review Research **2**, 023229 (2020).

[80] K. Kitayama, Y. Tanaka, M. Ogata, and M. Mochizuki: Journal of the Physical Society of Japan **90**, 104705 (2021).

[81] K. Kitayama, M. Mochizuki, Y. Tanaka, and M. Ogata: Physical Review B **104**, 075127 (2021).

[82] K. Kitayama, M. Ogata, M. Mochizuki, and Y. Tanaka: Journal of the Physical Society of Japan **91**, 104704 (2022).

[83] K. Kitayama and M. Ogata: arXiv preprint arXiv:2311.07176 (2023).

[84] K. Kitayama and M. Ogata: in preparation .

[85] T. Mikami, S. Kitamura, K. Yasuda, N. Tsuji, T. Oka, and H. Aoki: Physical Review B **93**, 144307 (2016).

[86] N. Tajima, S. Sugawara, M. Tamura, Y. Nishio, and K. Kajita: Journal of the Physical Society of Japan **75**, 051010 (2006).

[87] S. Katayama, A. Kobayashi, and Y. Suzumura: Journal of the Physical Society of Japan **75**, 054705 (2006).

[88] A. Kobayashi, S. Katayama, Y. Suzumura, and H. Fukuyama: Journal of the Physical Society of Japan **76**, 034711 (2007).

[89] H. Kino and H. Fukuyama: Journal of the Physical Society of Japan **64**, 1877 (1995).

[90] H. Seo: Journal of the Physical Society of Japan **69**, 805 (2000).

[91] Y. Tanaka and K. Yonemitsu: Journal of the Physical Society of Japan **77**, 034708 (2008).

[92] Y. Tanaka and M. Ogata: Journal of the Physical Society of Japan **85**, 104706 (2016).

[93] R. Wojciechowski, K. Yamamoto, K. Yakushi, M. Inokuchi, and A. Kawamoto: Physical Review B **67**, 224105 (2003).

[94] A. Kiswandhi and T. Osada: Journal of Physics: Condensed Matter **34**, 105602 (2021).

[95] A. Kobayashi, S. Katayama, K. Noguchi, and Y. Suzumura: Journal of the Physical Society of Japan **73**, 3135 (2004).

[96] T. Osada: Journal of the Physical Society of Japan **86**, 123702 (2017).

[97] T. Osada and A. Kiswandhi: Journal of the Physical Society of Japan **90**, 053704 (2021).

[98] T. Ishikawa, Y. Sagae, Y. Naitoh, Y. Kawakami, H. Itoh, K. Yamamoto, K. Yakushi, H. Kishida, T. Sasaki, S. Ishihara, et al.: Nature Communications **5**, 5528 (2014).

[99] T. Fukui, Y. Hatsugai, and H. Suzuki: Journal of the Physical Society of Japan **74**, 1674 (2005).

[100] N. Tsuji, T. Oka, and H. Aoki: Physical Review Letters **103**, 047403 (2009).

[101] A.-P. Jauho, N. S. Wingreen, and Y. Meir: Physical Review B **50**, 5528 (1994).

[102] G. D. Mahan: *Many-particle physics* (Springer Science & Business Media, 2000).

[103] Y. Suzumura and A. Kobayashi: Journal of the Physical Society of Japan **80**, 104701 (2011).

[104] K. Asano and C. Hotta: Physical Review B **83**, 245125 (2011).

[105] L. Tarruell, D. Greif, T. Uehlinger, G. Jotzu, and T. Esslinger: Nature **483**, 302 (2012).

[106] N. Tsuji, T. Oka, and H. Aoki: Physical Review B **78**, 235124 (2008).

[107] H. Kino and T. Miyazaki: Journal of the Physical Society of Japan **75**, 034704 (2006).

[108] Y. Kawakami, T. Amano, Y. Yoneyama, Y. Akamine, H. Itoh, G. Kawaguchi, H. Yamamoto, H. Kishida, K. Itoh, T. Sasaki, et al.: Nature Photonics **12**, 474 (2018).

[109] Y. Kawakami, T. Amano, H. Ohashi, H. Itoh, Y. Nakamura, H. Kishida, T. Sasaki, G. Kawaguchi, H. Yamamoto, K. Yamamoto, et al.: Nature Communications **11**, 4138 (2020).

[110] K. Uchida, H. Hirori, T. Aoki, C. Wolpert, T. Tamaya, K. Tanaka, T. Mochizuki, C. Kim, M. Yoshita, H. Akiyama, et al.: Applied Physics Letters **107** (2015).

[111] K. Uchida, T. Otobe, T. Mochizuki, C. Kim, M. Yoshita, H. Akiyama, L. Pfeiffer, K. West, K. Tanaka, and H. Hirori: Physical Review Letters **117**, 277402 (2016).

[112] D. Ohki, Y. Omori, and A. Kobayashi: Physical Review B **101**, 245201 (2020).

[113] Y. Dong, M.-M. Yang, M. Yoshii, S. Matsuoka, S. Kitamura, T. Hasegawa, N. Ogawa, T. Morimoto, T. Ideue, and Y. Iwasa: Nature Nanotechnology **18**, 36 (2023).

[114] E. Mori, H. Usui, H. Sakamoto, K. Mizoguchi, and T. Naito: Journal of the Physical Society of Japan **81**, 014707 (2011).

[115] P. Hosur: Physical Review B **83**, 035309 (2011).

[116] F. De Juan, A. G. Grushin, T. Morimoto, and J. E. Moore: Nature Communications **8**, 15995 (2017).

[117] C.-K. Chan, N. H. Lindner, G. Refael, and P. A. Lee: Physical Review B **95**, 041104(R) (2017).

[118] O. Matsyshyn, F. Piazza, R. Moessner, and I. Sodemann: Physical Review Letters **127**, 126604 (2021).

[119] J. Ahn, G.-Y. Guo, and N. Nagaosa: Physical Review X **10**, 041041 (2020).

[120] A. Arora, J. F. Kong, and J. C. Song: Physical Review B **104**, L241404 (2021).

[121] M. S. Rudner and N. H. Lindner: arXiv preprint arXiv:2003.08252 (2020).

[122] A. Kumar, M. Rodriguez-Vega, T. Pereg-Barnea, and B. Seradjeh: Physical Review B **101**, 174314 (2020).